RHODES UNIVERSITY
Where leaders learn

Photodynamic Anticancer and Antimicrobial Activities of π-Extended BODIPY Dyes and Cationic Mitochondria-Targeted Porphyrins

A thesis submitted to Rhodes University in partial fulfilment of the requirements for the degree of

Master of Science (Chemistry)

By

Choonzo Nachoobe Chiyumba

BSCH (Rhodes University)

Supervised by Professor *John Mack*

Co-supervised by Dist. Prof Tebello Nyokong

Dedication

To my mother, Phaides Shansali and father, Dauge Chilekwa Chiyumba, I am proud to have/had you as my parents. Thank you for nurturing and investing in me and being excellent role models.

To DAD, may your soul rest in eternal peace! And, I know you would have been proud of what I have become and achieved, and to MUM, you will always be at heart, and I love you.

Acknowledgements

I want to acknowledge the support from all the beautiful people who made the completion of this work a success.

In particular, I would like to express my sincere gratitude to the following:

Professor John Mack, my supervisor and the nanotechnology specialist in the Institute of Nanotechnology Innovation, without his thorough and supportive guidance, this work would not have been possible;

The National Research Fund (NRF) of South Africa for the financial support throughout my studies;

Dr Balaji Babu for mentoring me and his thoughtful advice throughout my studies;

Professor Kevin Lobb for coaching me throughout molecular docking;

The Chemistry Department at Rhodes University;

The Institute of Nanotechnology (INI) Rhodes University and the S22 lab members for being good collaborators;

Big mama Evenie Chiyumba Malambo and her husband Vincent Malambo for always being my cheerleaders and always believing in me;

My siblings; Lisa and Kelly Pembele, Mebelo and Chiyumba Chiyumba, Mwiinga Chiyumba and Nyanga Chiyumba;

My unconditional friends, Namalala Kashinka, Memory Nsowa Pongolani Phiri, Eng. Situmbeko Liyanda, Dr Mando Mwenya Seluka, Bienfait K. Isamura, Jones Chilufya, Nsanga Njelama, Mojahi Moatung, Simunikiwe Nogqala , Urbain Ndogano, Justin Bazibuhe, Graddy Mukubwa, James Oyim, and Bridged Magaela.

Abstract

Cancer is among the most devastating diseases and is mainly caused by gene mutation. This could be hereditary, or the mutation could be stimulated due to a lifestyle one lives, such as smoking, which induces lung cancer. The high morbidity rates of cancer are attributed to it being metastatic. The relatively poor physicochemical properties of existing drugs have caused treatment to be ineffective. Photofrin®, Foscan®, and Photogem® are some of the porphyrin-based derivatives approved by the Food and Drug Administration (FDA) for use in photodynamic therapy (PDT). Despite having such drugs, the quest to find better cancer drugs is still ongoing and 4,4-difluoro-4-bora-3a,4a-diaza-*s*-indacene (BODIPY) dyes are among the molecules that are being studied as potential photosensitisers (PS) in PDT. However, these molecules suffer from poor solubility and ineffective generation of singlet oxygen, the main ingredient in PDT treatment.

Furthermore, photosensitisers used in PDT face a problem with hypoxic conditions associated with cancer cells, which causes the generation of singlet oxygen to be relatively low. The PS also suffer from the untargeted treatment, increasing their toxicity.

Therefore, the main aim of this study was to improve the bioavailability of BODIPY dyes. Thus, a series of BODPIY dyes were synthesised with hydrogen bond accepting atoms and heavy atoms that enhance singlet oxygen generation.

Additionally, to override hypoxia conditions, porphyrins with mitochondria targeting properties were synthesised since it has been well established that the mitochondria will always have a decent amount of oxygen in cancerous cells. When employed as PS in PDT studies, these molecules have better cytotoxic abilities than BODIPY dyes,

and this potency was credited to their mitochondria targeting ability and efficient singlet oxygen generation.

Finally, this study reports the synthesis of di- and mono-substituted BODIPY dyes with improved solubility and porphyrins substituted with triphenyl phosphine, a mitochondria targeting moiety. On the other hand, the work further illustrates the synthesis of β-substituted cationic porphyrin with mitochondria targeting properties.

Table of contents

Table of Contents

List of figures

List of schemes

List of Tables

List of symbols

β	Beta
ε	Molar extinction coefficient
f	Oscillator strength
η_{cpd}	Refractive indices of solvent
λ	Wavelength
O_2	Ground state oxygen
$^1O_2$	Singlet oxygen
Φ_F	Fluorescence quantum yields
Φ_Δ	Singlet oxygen quantum yield
P	Lipophilicity
^1PS	Ground state photosensitizer
$^1PS^*$	Singlet excited state photosensitizer
$^3PS^*$	Triplet state photosensitizer
S_0	Ground state
S_1	Singlet excited state
T_T	Triplet lifetime

List of abbreviation

BC	Before Christ
$BF_3{\cdot}OEt_2$	Boron trifluoride diethyl etherate
BODIPY	Boron dipyrromethene
CFU	Colony forming units
DCM	Dichloromethane
DBB	1,2-dibenzoylbenzene
DMEM	Dulbecco’s modified Eagle’s medium
DMSO	Dimethylsulfoxide
DPBS	Dulbecco’s phosphate-buffered saline
DPBF	1,3-diphenylisobenzofuran
DPM	Dipyrromethene
FCS	Fetal calf serum
FDA	Food and Drug Administration
f−TPP	Formyl−tetraphenylporphyrin
HOMO	Highest occupied molecular orbital
HSA	Human serum albumin
ISC	Intersystem crossing
LED	Light emitting diode

LUMO	Lowest unoccupied molecular orbital
MALDI-TOF-MS	Matrix-assisted laser desorption/ionisation-time of flight-mass spectrometry
MCD	Magnetic circular dichroism
MCF-7	Breast cancer cell line
MO	Molecular orbital
MS	Mass spectrometry
MTT	Trypan blue and tetrazolium dye
NBS	N-bromosuccinimide
NIS	N-iodosuccinimide
NMR	Nuclear magnetic resonance
PDT	Photodynamic therapy
PET	Photoelectron transfer
ROS	Reactive oxygen species
TD-DFT	Time−dependent density functional theory
TEA	Triethylamine
TFA	Trifluoroacetic acid
TLC	Thin−layer chromatography
TPP′	Tetraphenylporphyrin
UV-vis	Ultraviolet-visible

ZnPc	Zinc phthalocyanine
ZnTPP	Zinc tetraphenylporphyrin

Chapter one

General Introduction

1. INTRODUCTION

1.1 Cancer

1.1.1 Epidemiology

Cancer has become a barrier to an increase in life expectancy and has also been ranked among the leading causes of death worldwide.[1,2] The first documented cancer cases were reported in an ancient Egyptian book describing trauma surgery, which dates from around 3000 BCE.[3,4] The book describes the removal of 8 ulcers of the breast by cauterisation with a fire drill tool, and the book further records a statement about the disease that "there is no treatment." In this era, the disease was not called cancer. The root of the word cancer is credited to the "father of medicine," Hippocrates, who used the words *carcinos* and *carcinomas* to define non-ulcer and ulcer-forming tumours (460−370 BC).[3]

This disease has continued to greatly impact human health even in the 21st century. In the absence of sufficiently effective treatments, there are ever-increasing morbidity and mortality rates. Incidence rates of cancer gradually increase as age climbs. Thus, advanced age is the major risk factor for cancer.[5] **Figure 1.1** shows less than 25 cases per 100,000 people for ages below 20. This increases to around 350 cases per 100,000 people from 45 to 49 years, and cases further increase for an age group of 60 and older to about 1,000 cases per 100,000 people. This figure further presents the number of incidents and mortality cases in 2020 for all countries. GLOBOCAN in 2020 recorded a total of over 19 million new cases in both sexes, with breast cancer having the highest incident cases, 2.3 million (11.7%). Lung cancer was the second highest with 2.2 million cases (11.4%), and colorectum was third with 1.9 million cases (10%). The second last in the top five common cancer was prostate with 1.4 million new cases

(7.3%), and in fifth place was stomach cancer with 1.1 million cases (5.6%). Liver and cervical cancer were placed in sixth and seventh place, respectively, with liver cancer having 905,000 (4.7%) while cervical had 604,127 cases (3.1%). The remaining percentage came from other cancers, which were grouped, and 8.9 million cases were recorded (46%).[5,6]

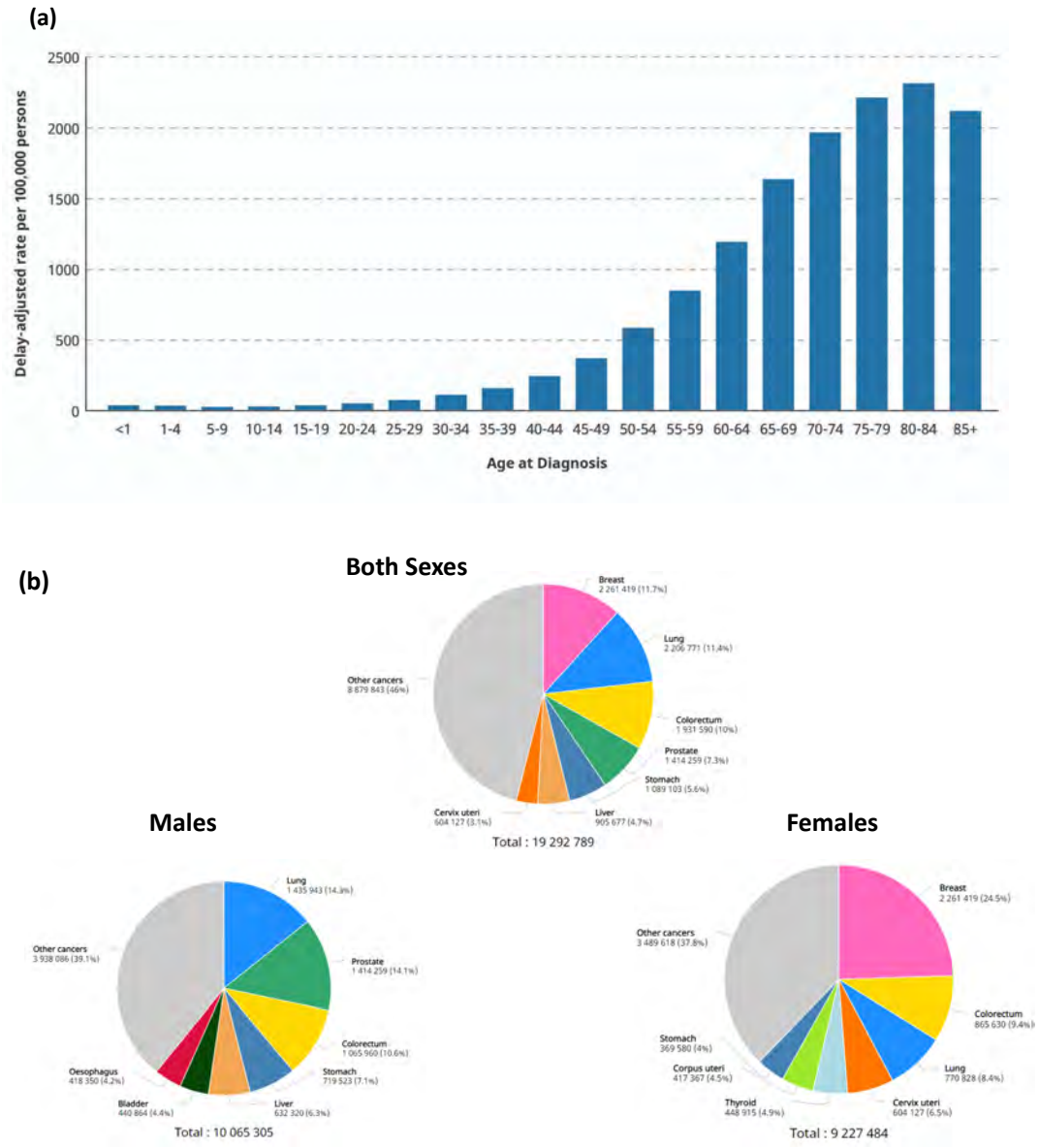

Figure 1.1 (a) Incidence rates by age of diagnosis for both sexes from 2013-17. [7] Credit: National Cancer Institute (b) the number of new incident cases in 2020 for both sexes, males only and female only.[5] This figure was reproduced with the permission of John Wiley & Sons, Hoboken, New Jersey, U.S., 2020 (Accessed 13.06.2022).

Figure 1.2 shows an estimate of the mortality rates that occurred in 2020. A total of 10 million deaths emerged and lung cancer had the highest death rate of 1.8 million (18%), colorectum cancer 935,173 (9.4%), liver 830,180 (8.3%), stomach 768,793 (7.7%), and breast cancer 684,996 (6.9%). Furthermore, Oesophagus cancer had a mortality rate of 544,076 (5.5%) and pancreas cancer of 466,003 (4.7%). Additionally, 3.9 million deaths (39.5%) were recorded for all remaining cancers. Breast cancer had the highest mortality rate in females (684,996;15.5%).[5,6] For this reason, this study selected this type of cancer as the primary cancer of interest.

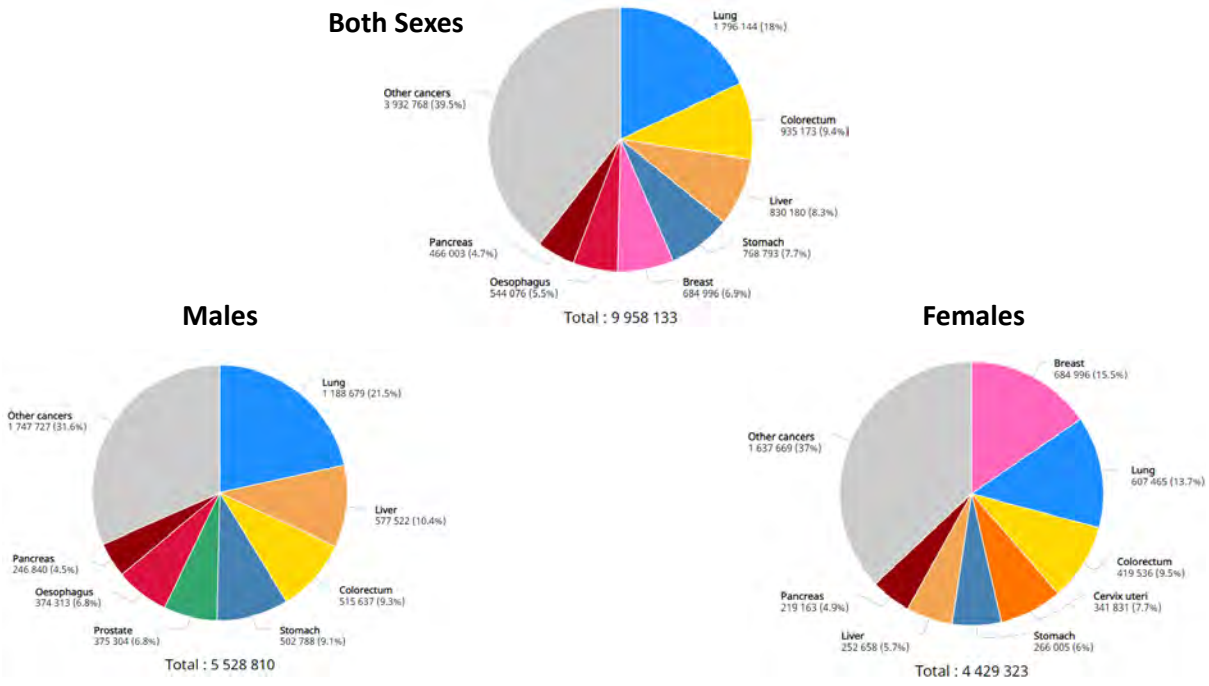

Figure 1.2 Mortality rates in 2020 for both sexes, males only and females only.[5] This figure was reproduced with the permission of John Wiley and Sons, Hoboken, New Jersey, U.S., 2020 (Accessed 13.06.2022).

1.1.2 Etiology and pathogenesis

The etiological causes of cancer are divided into three groups: physical carcinogenesis (e.g., ionizing radiation, ultraviolet radiation), chemical carcinogenesis (asbestos,

benzpyrene, etc.), and biological carcinogenesis (viruses, bacteria, and fungi).[8] These etiological causes damage the cell's genetic apparatus, leading to the inactivation of tumour suppression genes and activation of tumour protomer genes and mutation.[8–10] This, in turn, induces abnormal division of cells that form malignant tumours, which acquire properties such as the ability to spread to nearby tissues with the help of circulatory and lymphatic systems. This causes metastasis, which is the major cause of death in cancer patients.[8,10]

1.2 Therapeutic methods

Conventionally cancer is treated using surgery, chemotherapy, radiotherapy, or a combination of these. These modes of treatment are invasive and cause severe side effects. Additionally, the efficacy of the traditional methods heavily depends on the cancer's stage, type, and location. Therefore, there is a need to conduct in-depth research on other treatments that will override the drawbacks of traditional cancer treatment, such as photodynamic therapy (PDT).[11–19]

1.2.1. Photodynamic therapy

PDT is a non-conventional cancer treatment mode that has been investigated for over 30 years.[20–23] This treatment involves three factors: light (600−900 nm), a photosensitiser (light-sensitive drug), and oxygen. To initiate this therapy, a PS that selectively accumulates in the lesion is administered intravenously, locally, or topically. After an incubation time (allowing the PS to localise in the target site), the lesion is illuminated with light, and this excites the PS and enables it to react with oxygen when available. This leads to the formation of oxidant species (radicals, singlet oxygen, and triplet species (**Figure 1.3**), leading to cell death in the target tissues.[20,24–30]

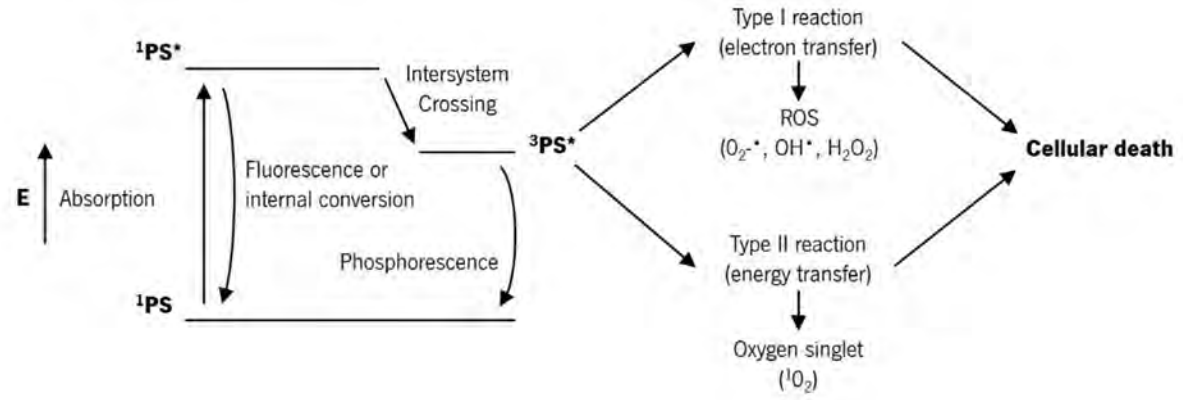

Figure 1.3 PDT mechanism of action using a modified Jablonski diagram.[29] This figure was reproduced with the permission of MDPI, Basel, Switzerland, 2021 (Accessed 16.05.2022).

1.2.1.1. PDT components and photochemical mechanism of action

Generally, PDT comprises oxidizing biomolecules that are produced photochemically through two reaction mechanisms, Type I and Type II.[23,27,31] When the PS absorbs light, it is excited from the ground state (**^{1}PS**) to a short-lived singlet excited state (**^{1}PS***).[32–36] This state is exceptionally unstable and can either undergo internal conversion by losing obtained energy as heat or decay back to the ground state *via* fluorescence (loss of energy by photon emission). Nonetheless, **^{1}PS*** can undergo intersystem crossing due to spin-orbital coupling, which can be promoted by the heavy atom effect. This enables **^{1}PS*** to progress to a more stable triplet state (**^{3}PS***), which has a spin inversion of an electron in orbitals in higher energies.[36–42] A PS in the T_1 state can either relax back to the ground state through phosphorescence (light emission) or undergo the Type I and Type II mechanisms (**Figure 1.3**).[32,34,35,43]

The **^{3}PS*** state has a longer lifetime than the singlet excited state providing sufficient time to transfer energy directly to molecular ground state oxygen (O_2). This is referred to as the Type II mechanism.[33,44–46] This energy transforms O_2 into singlet oxygen

($^1O_2$). $^1O_2$ is extremely reactive. Thus, it induces oxidative stress to biomolecules, damaging them and leading to cell death.[31,33–36,40] Additionally, Type I reactions involve the direct transfer of electrons or abstraction of hydrogen atoms from the substrate, such as the cell membrane, due to the interaction with the excited PS (**Figure 1.3)**. This phenomenon leads to the production of reactive oxygen species (ROS), such as $HO^{\bullet}$, $O_2^{-\bullet}$, and H_2O_2, and these cause biological lesions due to their oxidative damage property.[37,42,46,47]

1.2.1.2. Mediated–PDT cell death action mechanism

The mechanism of action of PDT involves the generation of ROS, which triggers either necrotic, apoptotic and/or autophagy type of cell death.[48] The mode and the extent of death depend on cellular morphology, immunological responses, PS subcellular localisation, oxygen concentration, excitation wavelength, and intensity, among other factors. The stated factors influence whether cell death is either nonprogrammed or programmed.[48–53]

Autophagy occurs when the cell tries to repair its damage from photoinjury. When this reaction fails, this cell is signalled for apoptosis. Apoptosis is another programmed mode of cell death that is distinguished by the degradation of the nucleus and membrane and occurs when the PS primarily localise in the mitochondria.[51,54–57] The last mode of cell death mediated by PDT is necrosis, which occurs due to inflammation that is indued from external stimuli such as trauma. The PS involved in such deaths localises in the plasma membrane (**Figure 1.4**).[58–62]

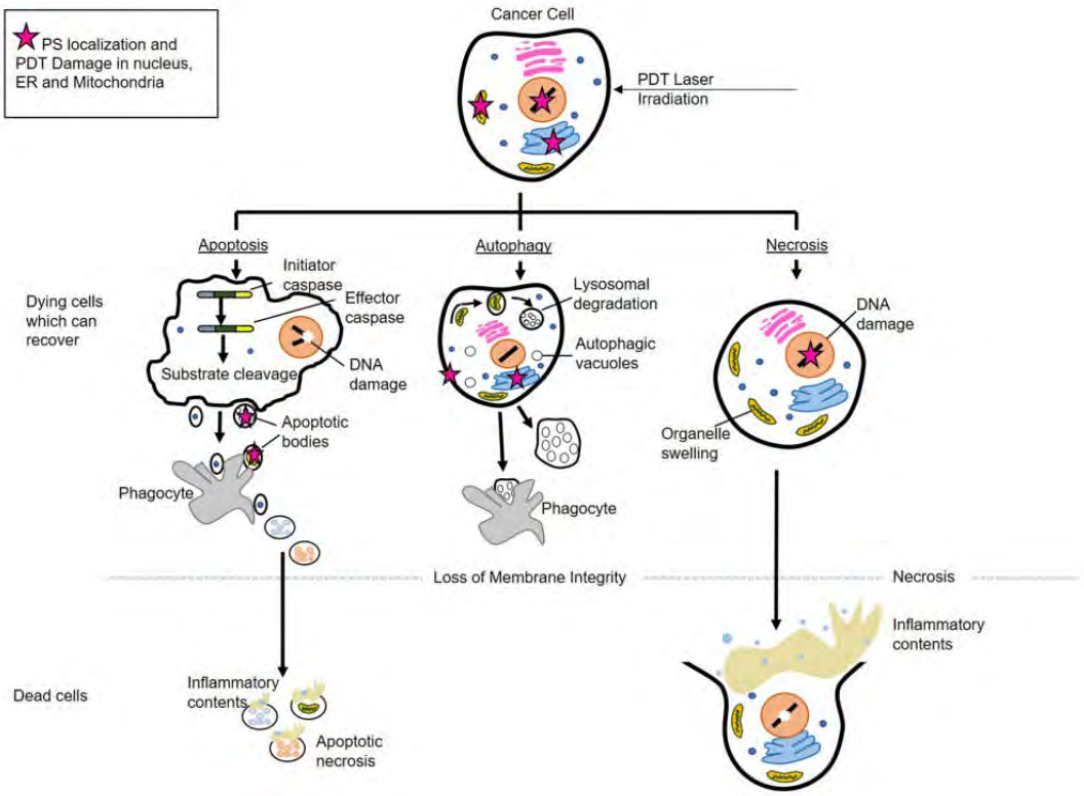

Figure 1.4 Modes of cell death induced by PDT.[30,48] This figure was reproduced with the permission of Elsevier, Amsterdam, Netherlands, 2004. (Accessed 16.05.2022).

1.3 Types of photosensitisers

1.3.1. BODIPY DYES

4,4′-Difluoro-4-bora-3a,4a-diaza-*s*-indacenes, popularly known as BODIPY dyes, are highly fluorescent dyes with a versatile structure, which allows for the modification of the core dye. These modifications enable the dyes to be used in a wide range of applications, such as PDT/PACT, optical limiting, solar cells, and fluorescent labelling. Treibs and Kreuzer first reported these dyes after a serendipitous synthesis in 1968.[63–68] Initially, BODIPY dyes were not studied further. In the 1990s, the dyes attracted attention when Boyer and Pavlopoulos reported their possible use in fluorescence markers and tunable lasers as organic fluorophores.[69–71] The interest in these dyes arises from their facile synthesis, excellent spectroscopic properties (narrow

Gaussian-shaped emission and absorption bands), structural versatility, high molar extinction coefficients (ε > 80000 M^{-1} cm^{-1}), and high fluorescence quantum yields (Φ_F). Furthermore, BODIPY dyes (core dye) (**Figure 1.5**) exhibit moderate redox potentials, high sensitivity to polar solvents, negligible triplet-state formation, and high photothermal stability.[72–76]

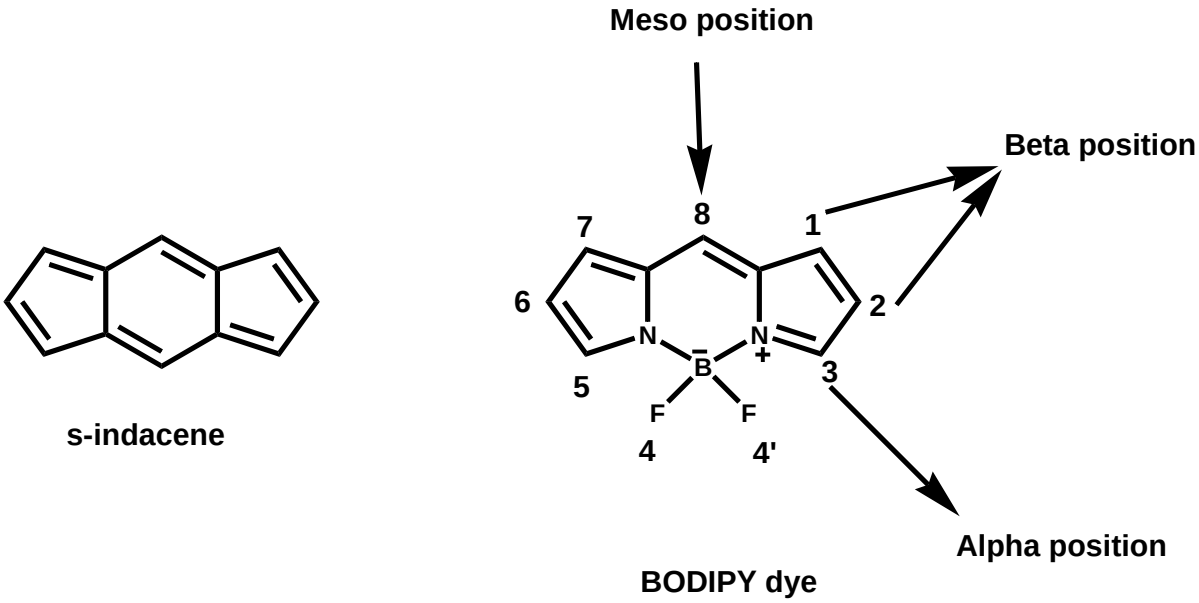

Figure 1.5 BODIPY dye and the IUPAC numbering on its *s*-indacene core.[68]

BODIPY dyes are zwitterionic and consist of two pyrrolic rings complexed with a disubstituted boron atom (BF_2). This complexation creates a rigid system that prevents *cis*/*trans* isomerisation of the dipyrromethene and enables them to have a π-conjugated system.[77–81] Despite having such a system, BODIPY dyes do not obey Hückel's 4n + 2 rule of aromaticity due to the presence of the boron atom. Their structures are normally compared to indacene dyes due to their rigid planar conformation arising from the coordination at the boron centre.[82–84] Indacene dyes are considered aromatic, and their π-MOs can be compared to that of aromatic cyclic perimeter $C_{12}H_{12}^{2-}$ that has M_L = 0, ±1, ±2, ±3, ±4, ±5 MOs arranged in ascending energy terms.[84] The nodal patterns of the π-MOs of BODIPY dyes follow the same

sequence as that of the $C_{12}H_{12}^{2-}$. However, the introduction of the cross-links, BF_2, and the pyrrolic nitrogens give rise to a lower symmetry (C_{2V}) that causes a lifting in the degeneracies of the MOs energies (**Figure 1.6**). This phenomenon creates a distinct separation in the energies of the HOMO and LUMO from the rest of the π-system. The $S_0 \rightarrow S_1$ transitions are predicted to be almost 100% comprised of HOMO→LUMO transitions according to theoretical calculations.[84]

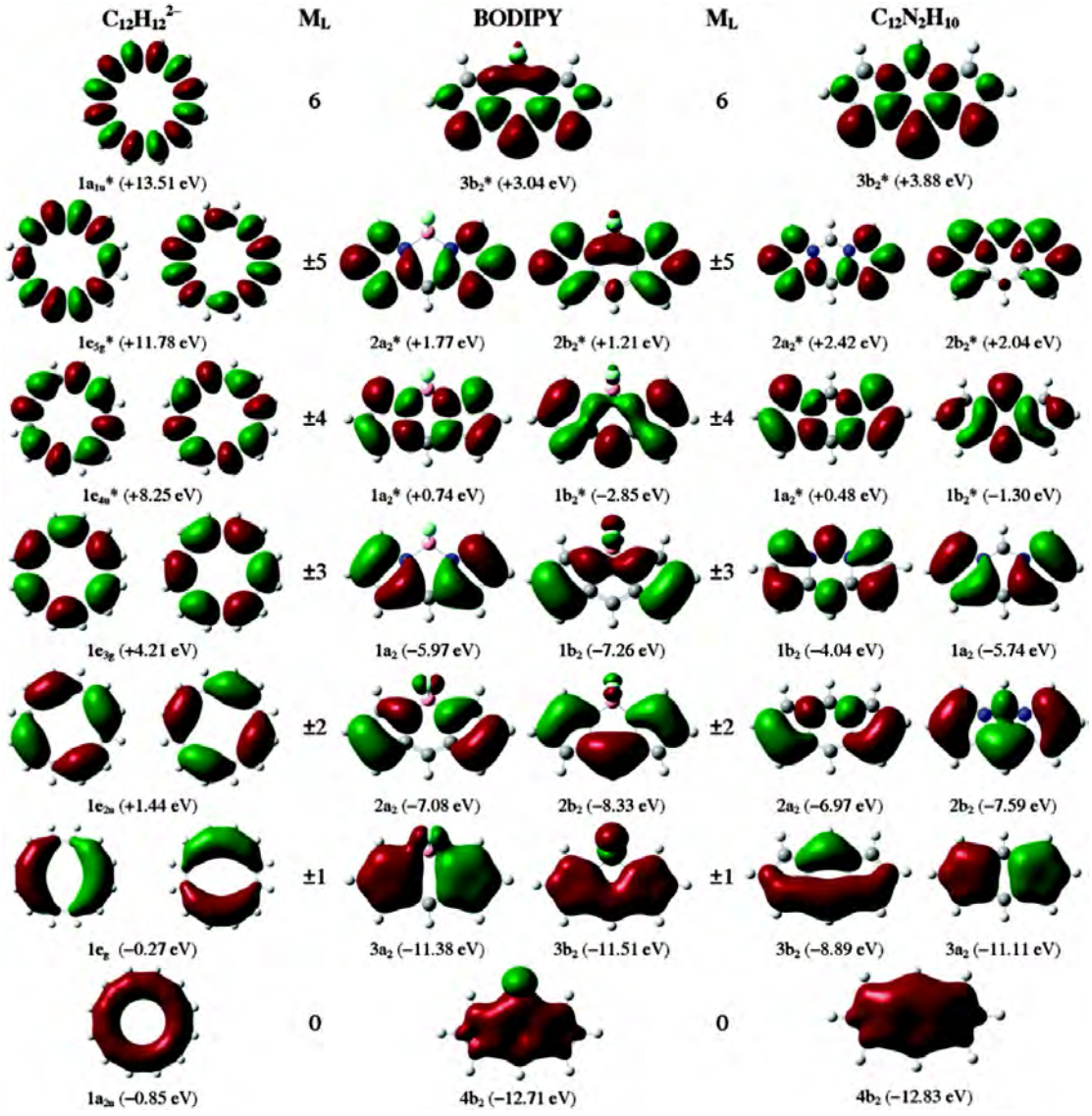

Figure 1.6 Cyclic perimeter $C_{12}H_{12}^{2-}$, BODIPY dye and a $C_{12}H_{10}H_2$ model compound MO energies.[84] This figure was reproduced with the permission of the Royal Society of Chemistry, London, UK, 2014. (Accessed 16.05.2022).

1.3.1.1. Synthesis of BODIPY dyes

BODIPY dyes are synthesised by reacting highly electrophilic carbonyl compounds (acid anhydrides, acid chlorides, or aldehydes) with a pyrrole to yield a dipyrromethene (DPM). The DPM is further reacted with BF_3 to form a complex with a boron centre (**Scheme 1.1**).[85–87]

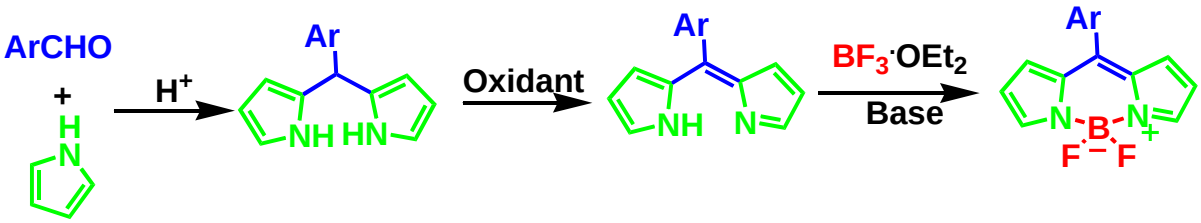

Scheme 1.1 General synthesis of a BODIPY core.[86]

1.3.1.2. BODIPY dye synthetic modification strategies

Structural modification of the BODIPY dyes is carried out to alter their photophysical properties, and these are achieved by the addition of functional groups at the α and β positions, the *meso*-positions, and substitution of the fluorine atoms at the 4,4′-position.[85–87]

1.3.1.2.1. Wavelength tuning strategies

A BODIPY dye must absorb in the therapeutic window (620−850 nm) to be an effective PS for PDT, since haemoglobin and other pigments absorb at shorter wavelength, while water absorbs at longer wavelength limiting the transparency of laser light in human tissue. This is attained through the extension of the π-conjugation system. Synthetic strategies followed to achieve this include styryl, aryl and alkenyl substitution.[84,88–90] BODIPY core dyes with methyl groups at the 3,5- and/or 1,7-positions are prone to chemical modification due to their strong nucleophilic character. The mesomeric effect attributed to this chemical modification destabilises the HOMO

relative to the LUMO at the 3,5-positions since larger MO coefficients are located at these positions in the HOMO (**Figure 1.6**). This leads to a narrowing of the HOMO−LUMO gap, so the main absorption band is shifted further into the therapeutic window.[84,91–94]

1.3.1.2.2. Singlet oxygen enhancement strategies

The generation of singlet oxygen ($^1O_2$) is fundamental for effective PDT and photodynamic antimicrobial chemotherapy (PACT). BODIPY dyes have low singlet oxygen quantum yields and high fluorescence quantum yields. This makes the dyes to be less effective in PDT and PACT. Populating the triplet manifold enables BODIPY dyes to produce $^1O_2$. Thus, these dyes are modified by adding heavy atoms, normally bromine or iodine, to enhance the ISC through spin coupling.[95–102]

5.1.1.1 Optical properties of BODIPY dyes

BODIPYs generally contain narrow absorption spectra with two maxima in the same region: (i) S_0−S_1 transition band (intense 0-0 band) and (ii) a small shoulder band attributed to 0-1 vibrational transitions (**Figure 1.7**). When the BF_2 centre is removed, the dye is transformed into a cyanine-type chromophore with an all-*trans* conformation. Cyanines can undergo *cis*-*trans* isomerisation resulting in fluorescence quenching upon electronic excitation.[103–108] The rigidity of BODIPY dyes arising from the BF_2 results in favourable properties for applications as fluorescent dyes since they typically have high fluorescence quantum yield values. Any structural modifications that induce flexibility in the molecule will lower the fluorescence quantum yields (Φ_F). For the lowest energy transitions, narrow Gaussian-shaped adsorption and emission bands are observed due to the similarity in the potential energy surfaces.[74,87,93,109–115]

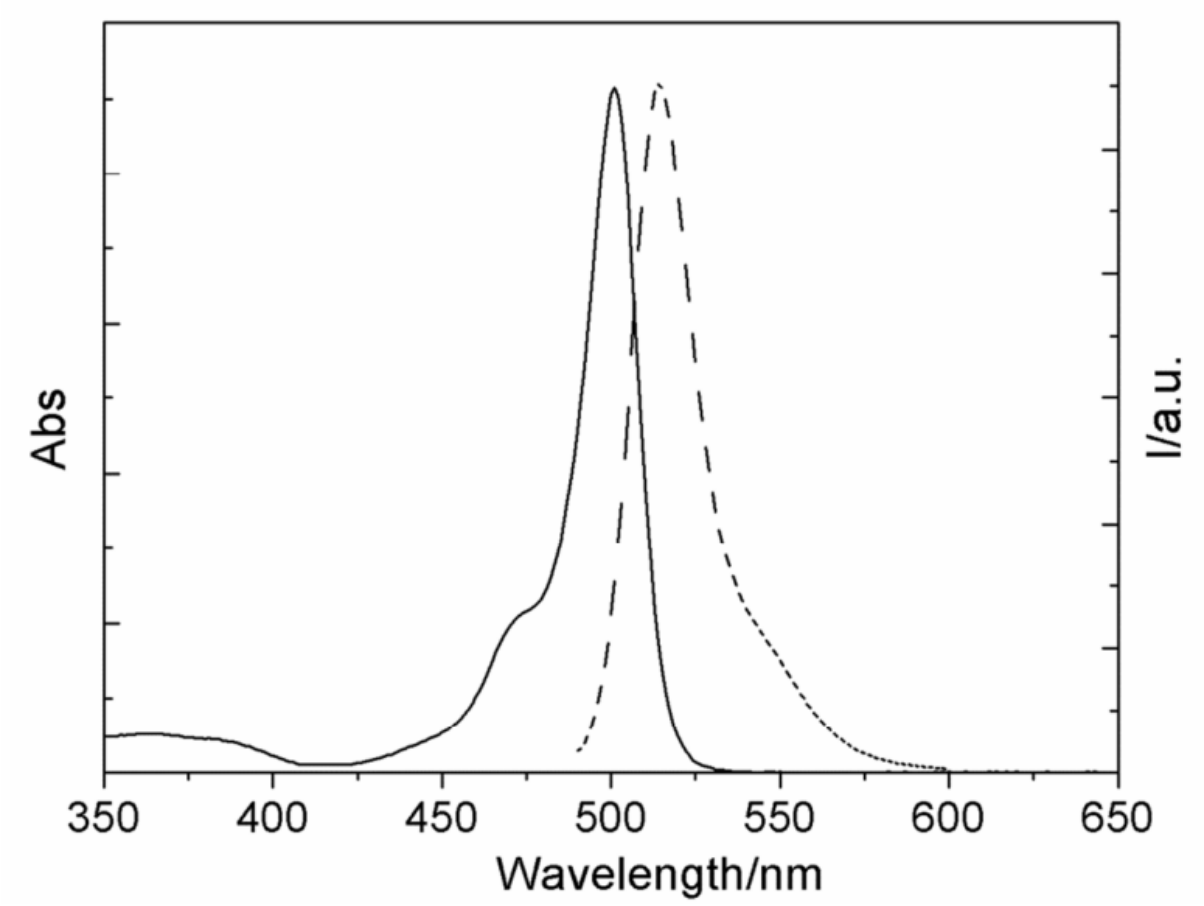

Figure 1.7 Absorption and emission spectra of a typical BODIPY dye core.[84] [84] The figure was reproduced with the permission of the Royal Society of Chemistry, London, UK, 2014. (Accessed 16.05.2022).

1.3.2. Porphyrins and their analogues

Porphyrins are macrocyclic 18π tetrapyrrole compounds linked with a methine (=CH–) in a planar conformation. The structure of porphyrin can be found in nature, in hemes and chlorophyll. An unsubstituted porphyrin ligand is called a porphin and is shown in **Figure 1.8** with its' pyrrolic rings labelled A to D.[116] Usually, the most common type of side chains attached to these rings are vinyl, ethyl, methyl, and acetic acid groups. Porphyrins and their analogues readily complex with metal cations such as Zn(II), Cu(II), Sn(IV), and Fe(II/III). Other derivatives of porphyrins exist, such as chlorins,

which are porphyrins with one reduced bond on one of the pyrrole rings, and bacteriochlorins, which have two oppositely arranged reduced bonds on two pyrrole rings of the porphyrin.[116]

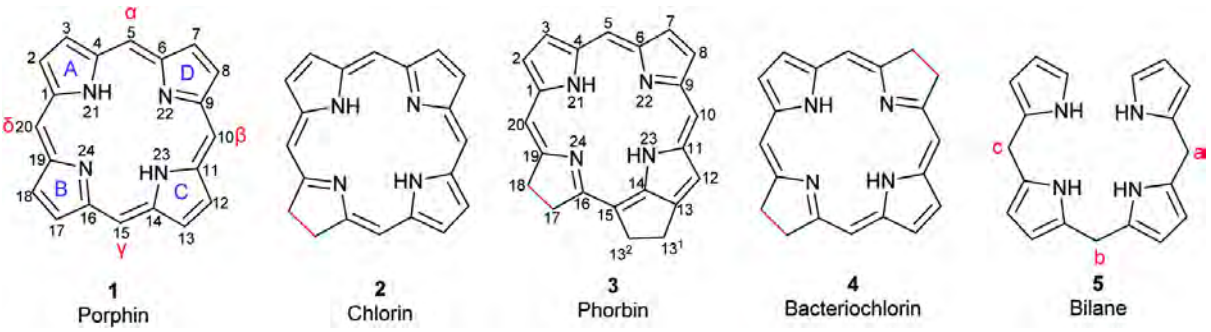

Figure 1.8 Current numbering of tetrapyrrole macrocyclic structures and the difference in bond saturation are highlighted in red.[116]

1.3.2.1 Physicochemical, spectroscopy, and symmetry properties of porphyrins and their analogues.

Porphyrin ligands contain 26 π-electrons. 18 of these take part in delocalisation on the inner cyclic perimeter according to Hückel's rule, **Figure 1.9**.[117–120] Two electron pairs associated with nitrogen atoms are sterically hindered when bound to protons. The absorption spectra of porphyrins are distinguished by two bands prominently in the visible region. The major band, called the B or Soret band, lies at *ca.* 400 nm, while the Q bands lie at the red end of the visible region. The B and Q bands arise from the π−π* transitions.[117,121–124] The B band becomes less intense if the ring is cleaved, or the π-conjugation is lost. Porphyrin derivatives (chlorins and bacteriochlorins) that have partial ring saturation still retain 18 π delocalised electrons with a B band in the 380−420 nm region and Q-bands that lie between 500−800 nm.[121,125]

The B and Q bands result from transitions between the four frontier molecular orbitals derived from a $C_{16}H_{16}^{2-}$ parent hydrocarbon perimeter. Gouterman's four-orbital model involves accidentally near-degenerate a_{1u} and a_{2u} MOs with M_L = ±4 angular nodal

patterns derived from the HOMO of the parent perimeter, and an e_g MO derived from the LUMO with M_L = ±5 angular nodal patterns.[121,126,127] Gouterman mixed the four possible excitations between the HOMO and LUMO by using the configuration theory to account for the forbidden and allowed Q and B bands based on ΔM_L = ±9 and ±1 properties, respectively.[126,127]

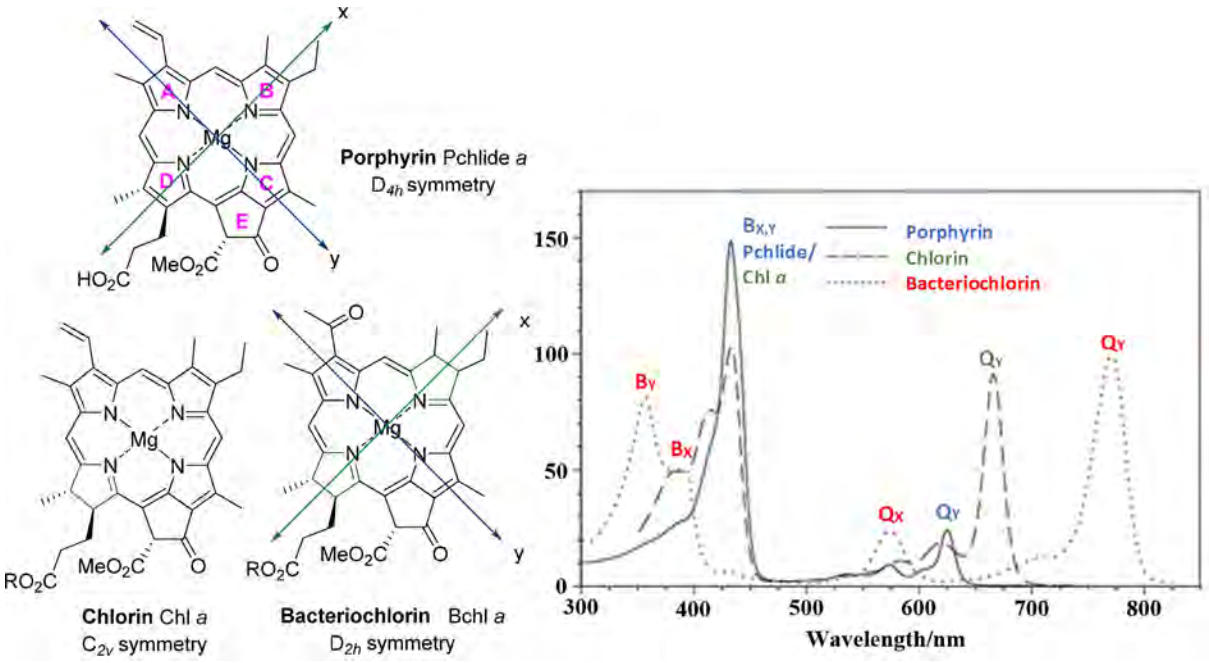

Figure 1.9 Molecular symmetries (LEFT) and electronic absorption spectra (RIGHT) of Mg(II) porphyrin, chlorin, and bacteriochlorin complexes.[117] This figure is reproduced with the permission of MDPI, Basel, Switzerland, 2014. (Accessed 16.05.2022).

The electronic properties of these macrocyclic tetrapyrroles largely depend on the ring's symmetry and the ligation effects on the central metal and the substituents around the molecule. One-electron transitions between the molecular orbitals aligned along the *x*- and *y*-axes through opposing pyrrole nitrogen atoms generate four excited states. This causes them to interact and overlap destructively and constructively with one another resulting in the allowed and forbidden B and Q bands, **Figure 1.10**. Due

to the D_{4h} symmetry of metal porphyrins, the nodal patterns of the a_{1u} and a_{2u} MOs of Gouterman's 4-orbital model are accidentally degenerate, while the e_g LUMO remains degenerate for symmetry reasons.[117,121,126,128–130] The application of charge transfer and modification between the excitations results in two sets of *x*- and *y*-polarised degenerate excitations. One set lies at higher energy and is strongly allowed, resulting in a ^1E_u state that gives rise to the B band at a shorter wavelength. The other set lies at lower energy and has low oscillator strengths, since this ^1E_u excited state arises from forbidden transitions. The observed intensity of the Q band arises primarily from vibrations occurring within the molecule.[121,128,131]

There is a pronounced difference in the number of Q-bands observed in the spectra of metalloporphyrins and free-base porphyrins. This is due to the decrease in symmetry of the free-base to D_{2h}, and this lower symmetry is caused by the presence of hydrogens bonded to two opposing central nitrogens. In this kind of molecule (with D_{2h}), the *x*-axis of the molecule (that is, through the central nitrogen atom with a pair of lone electrons) and the *y*-axis (through central nitrogen bonded with hydrogen) are not equivalent.[117,121,126] Therefore, the spectroscopic transitions will be split into *x*- and *y*-polarised bands. The excited states from these transitions will be non-degenerate, and the Q-bands become partially allowed (**Figure 1.10**). Additionally, the reduction of β,β'-double bonds, and addition of groups at the β position further reduces the symmetry of the porphyrin while metallation increases it, and a point group of D_{4h} is assigned to a generalised metalloporphyrin complex.[121,132]

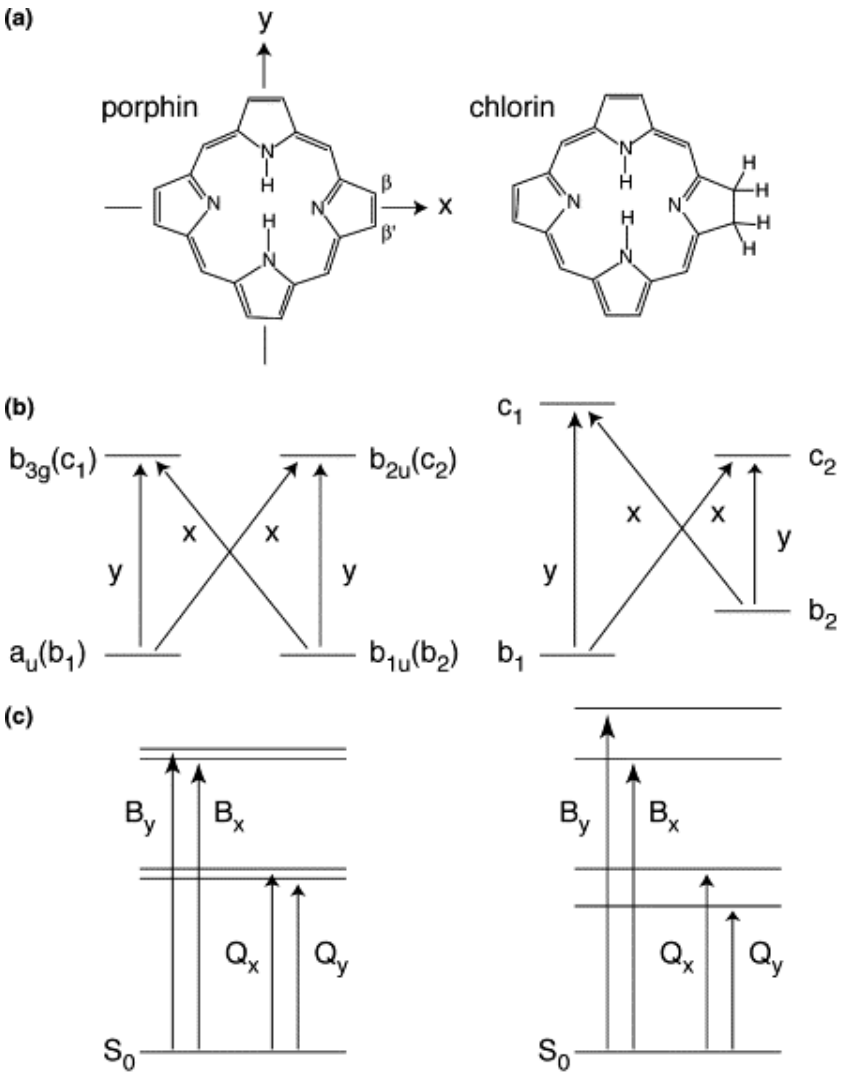

Figure 1.10 (a) Schematic representation of porphyrin and chlorin axes, (b) two HOMO and two LUMO MOs, and (c) electronic states of porphyrin and chlorin.[126] This figure is reproduced with the permission of Elsevier, Amsterdam, Netherlands, 2003. (Accessed 16.05.2022).

1.3.2.2 Synthetic strategies of porphyrins

The synthesis of porphyrins occurs readily when aryl rings are introduced at the *meso*-positions. This type of tetraarylporphyrin PS has attracted considerable attention due to its simplicity of preparation and potential to be chemically modified by introducing different aryl groups. The synthetic approaches usually involve the condensation of pyrrole with aryl or heteroaryl substituted aldehydes. The following are the commonly used methods to synthesise tetraarylporphyrins.[133–138]

Rothemund's method

Menotti and Rothemund are the pioneers of synthesizing *meso*-tetraphenylporphyrin and achieved a *ca.* 10% yield (**Scheme 1.2**). They reacted pyrrole with benzaldehyde in pyridine in a closed tube at 200 °C for 24 h. Due to harsh reaction conditions and lower yields, other ways were sought after that would enable the preparation of a wide range of *meso*-substituted porphyrins with much better yields.[139–143]

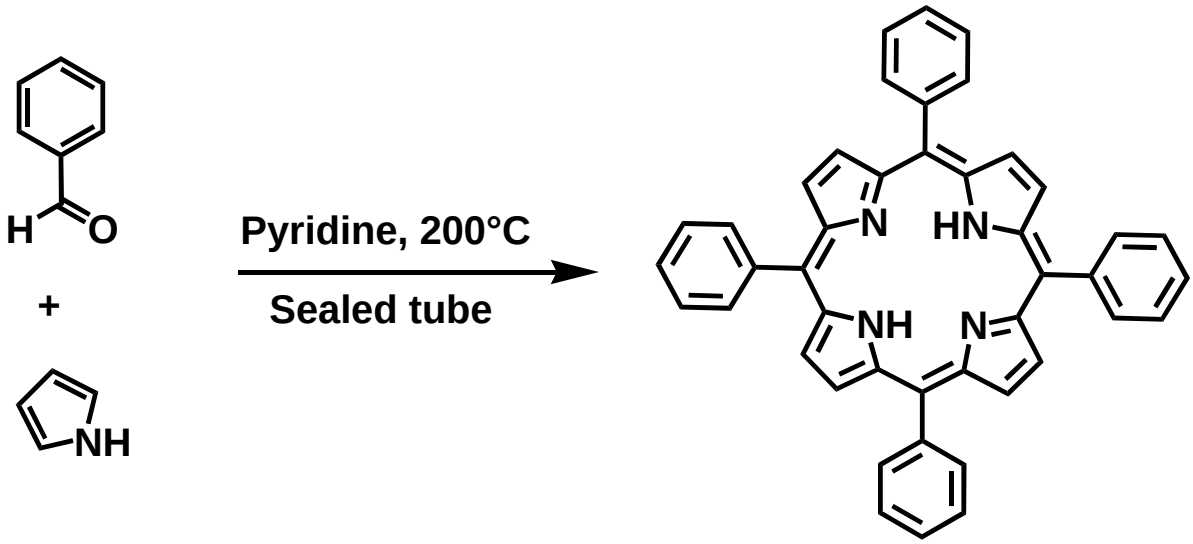

Scheme 1.2 Porphyrin synthesis using Rothemund's method.[139]

Adler-Longo's Method

Adler and Longo found ways of improving the above method. Their reaction procedure involved refluxing benzaldehyde with pyrrole for 30 min at 140°C in propionic acid. This enabled the development of porphyrins with a wide range of *meso*-aryl rings at *ca.* 20% yield (**Scheme 1.3**). The drawback of this protocol is that the purification method is laborious because of the high yields of tar that are formed. Due to the acidic conditions, the attempts to synthesise porphyrins using aldehydes substituted with

atoms that have hydrogen bonding abilities typically fail. This method is still regarded as the ideal way of synthesizing porphyrins despite its disadvantages.[144–150]

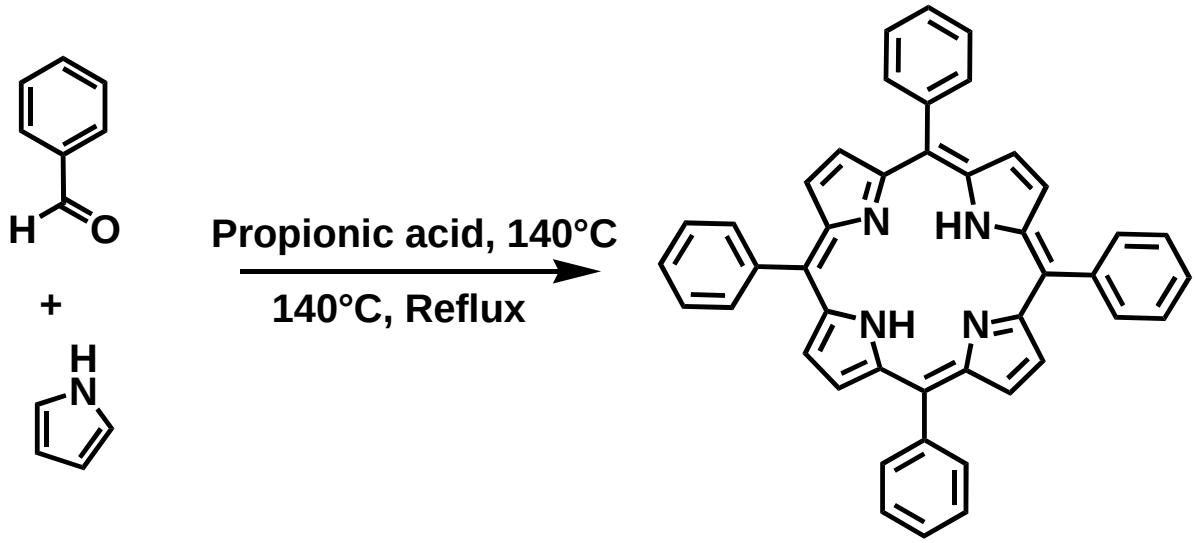

Scheme 1.3 Adler and Longo's porphyrin synthesis method.[144]

Lindsey's method

Lindsey reported a procedure that uses aldehydes that are unstable in acidic environments to synthesise porphyrins. In this method, equal amounts of pyrrole and benzaldehyde were reacted in DCM either in the presence of trifluoroacetic acid or boron trifluoride etherate (as catalysts) for 1 h at room temperature under inert gas (**Scheme 1.4**). Later, 2,3-dichloro-5,6-dicyanoquinone (DDQ) is added to form a porphyrin from porphyrinogen, with purification achieved at higher yields than the above two methods.[142,145,146,148]

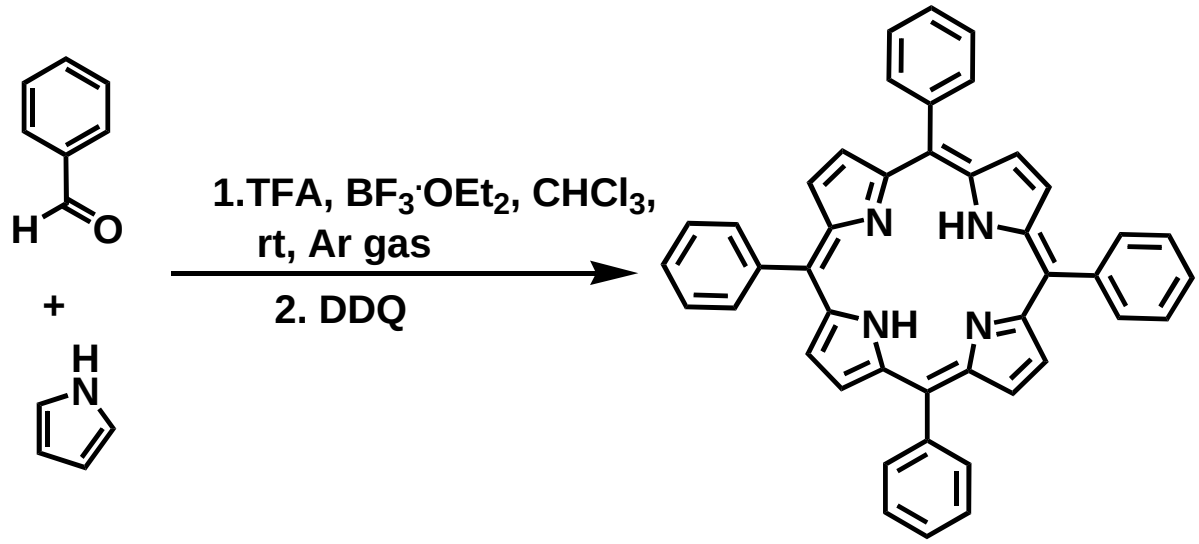

Scheme 1.4 Porphyrin synthesis using Lindsey's method.[143]

1.4 Photophysicochemical properties of photosensitisers

1.4.1 Singlet oxygen quantum yield

Oxygen can act as a universal quencher by accepting the excess energy from molecules that are excited electronically. This results in the formation of singlet molecular oxygen $O_2(^1\Delta_g)$, a highly reactive species.[99,151–154] Singlet oxygen can chemically and physically react with molecules of several classes. Anthracene derivatives have been widely used as substrates for $O_2(^1\Delta_g)$ and can hence be used to quantify singlet oxygen formation. The reactions involved mainly occur through chemical means to produce the corresponding endoperoxides (**Scheme 1.5**).[95,98,100,116,155,156]

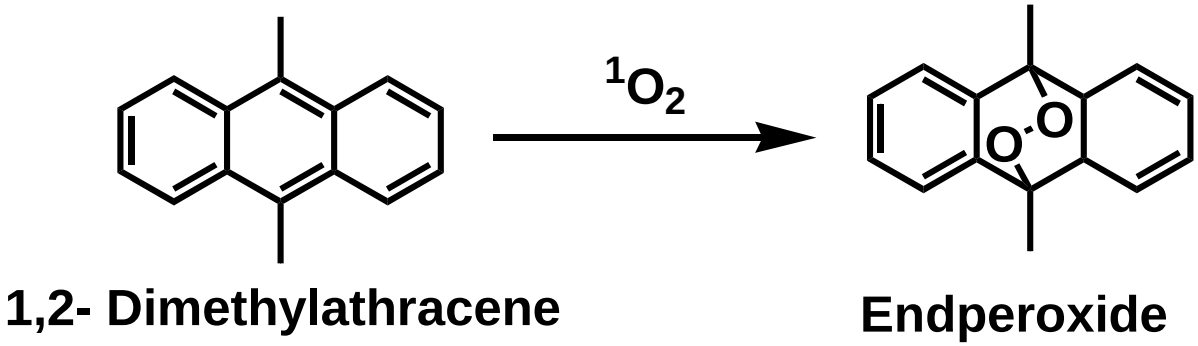

Scheme 1.5 Generation of endoperoxide from 9,10-dimethylanthracene and $^1O_2$.[155]

Another $^1O_2$ scavenger that has been widely studied is 1,3-diphenylisobenzofuran (DPBF). This scavenger readily undergoes 1,4-cycloaddition upon reacting with $^1O_2$, resulting in the formation of an endoperoxide (**Scheme 1.6**). This subsequently irreversibly forms 1,2-dibenzoylbenzene (DBB) and breaks the π-system making the molecule unable to absorb light at 412 nm (DPBF absorption wavelength) in a manner that can be used to quantify singlet oxygen generation by monitoring changes in the UV-visible absorption spectrum.[96,97,102,157–161]

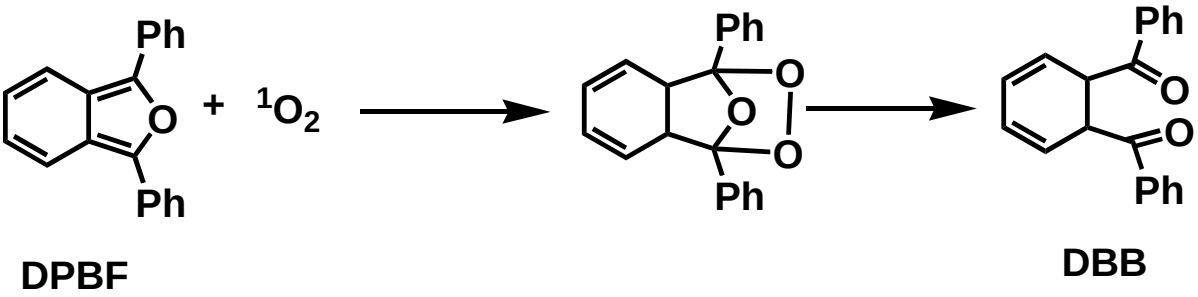

Scheme 1.6 Reaction mechanism of DPBF with $^1O_2$.[161]

In this work, two singlet oxygen scavengers with these structures were used to quantify how much $^1O_2$ is generated by the PS synthesised. A PS with a high singlet oxygen quantum yield, a parameter defined by the ratio of singlet oxygen species generated per photon, is preferred to attain greater PDT effectiveness. The magnitude of singlet oxygen generation is determined by the ability of the PS to undergo intersystem

crossing (ISC) to the triplet manifold (**Figure 1.4**).[162–165] In general, ISC is facilitated by incorporating heavy atoms, as described above. **Equation 1.1** was used to determine singlet oxygen quantum yields of the synthesised PS:

$$\Phi_{\Delta} = \Phi_{\Delta std} \frac{slope_{cpd}}{slope_{std}} \quad (\mathbf{1.1})$$

Where $slope_{cpd}$ and $slope_{cpd}$ are slopes obtained from the degradation of the singlet oxygen scavenger linear graphs. Zinc tetraphenylporphyrin (ZnTPP: $\Phi_{\Delta} = 0.55$) and methylene blue ($\Phi_{\Delta} = 0.52$) were used as standards in dimethyl sulfoxide (DMSO), and 9,10-dimethylanthracene or 1,3-diphenylisobenzofuran were used as singlet oxygen scavengers.[166–169]

1.4.2 Fluorescence quantum yields

Fluorescence is a form of luminescence in which molecules emit light from electronically excited states. Atoms or molecules absorb light at specific wavelengths and later emit it at a longer wavelength after a defined time interval (fluorescence lifetime).[170] This process is controlled by three factors; firstly, excitation of the molecule to a higher energy excited state by an incident photon on the femtosecond timescale; secondly, vibrational relaxation of excited electrons from higher vibrational levels to the lowest on the picosecond timescale; and thirdly, the return of the molecule to the ground state through emission of a photon typically on a nanosecond timescale (**Figure 1.11**).[171,172]

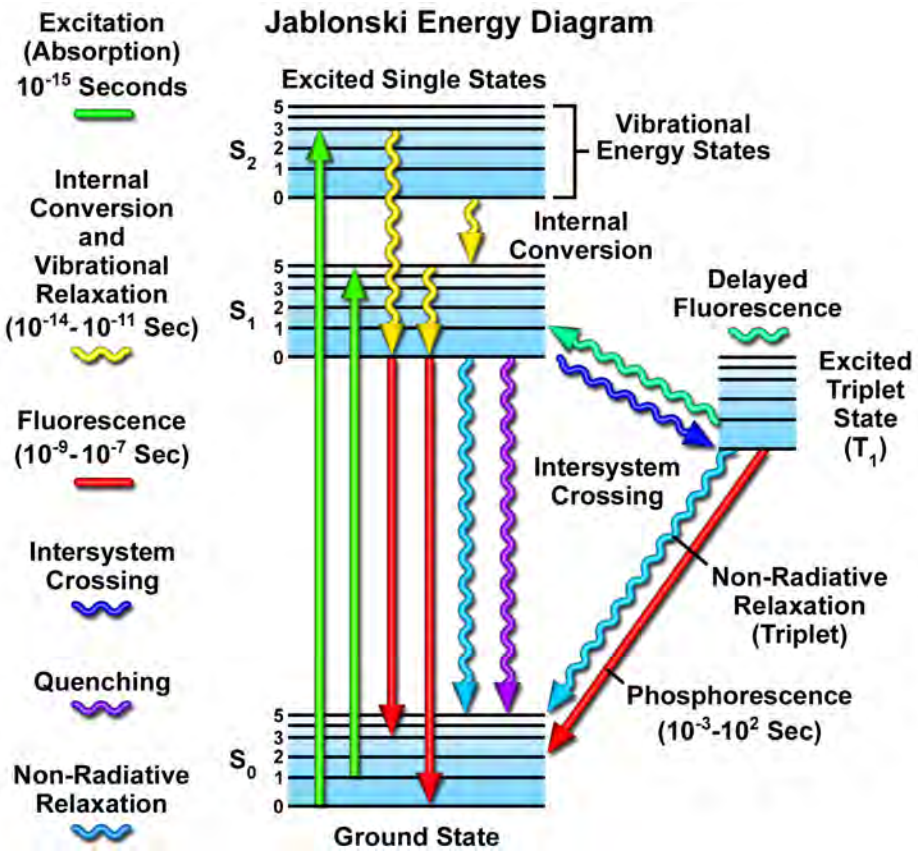

Figure 1.11 Schematic representation of Jablonski energy diagram.[173] This figure was reproduced with permission of Molecular Expressions™ Optical Microscopy Primer, By Ian D. Johnson and Michael W. Davidson, Florida, USA, (Accessed 16.05.2022).

Fluorescence quantum yield (Φ_F) values typically have an inverse relationship with the singlet oxygen quantum yield. Since this process is dependent on ISC, a higher rate of ISC results in lower fluorescence and *vice versa*.[170,171] In this study, we used a comparative method to determine the Φ_F values of the synthesised molecules. **Equation 1.2** was used to calculate the values of Φ_F:[175]

$$\Phi_F = \Phi_{F(std)} \frac{F_{cpd} A_{std} \eta_{cpd}^2}{F_{std} A_{cpd} \eta_{std}^2} \quad (\mathbf{1.2})$$

Where $\Phi_{F(std)}$ is the fluorescence quantum yield of the standard, F_{cpd} and F_{std} are the summations of intensities (fluorescence), and η_{cpd}^2 and η_{std}^2 are refractive indices of solvent used for compound and standard, respectively. In this study, a comparative method was used on this basis to determine the Φ_F values of the synthesized molecules. Rhodamine G6 (0.94)[174] in ethanol and ZnTPP (0.03)[175] in DMSO were used as the standards.

1.5 Other applications

1.5.1 Photodynamic antimicrobial chemotherapy

Photodynamic antimicrobial chemotherapy (PACT) is a non-invasive treatment that relies on the generation of reactive oxygen species to induce death to oral bacteria, plaque, scrapings, and biofilms. The principle behind PACT is similar to PDT. The only difference is the target to be treated. Briefly, this therapy relies on the combined use of a PS, light, and oxygen (**Figure 1.4**).[134,176,177] PACT has been accepted as an alternative treatment for bacteria since it overrides the disadvantage of resistance that is associated with antibiotics. As earlier alluded to, the efficiency of a PS dye is primarily dependent on the amount of singlet oxygen it can produce.[178,179]

1.6 Study background and rationale

Cancer has continued to be a global burden. It is currently rated as the second leading cause of death worldwide. Cancer is a disease in which a group of abnormal cells divide uncontrollably by overriding the rules of cell division. In the body, cells have signals that direct whether cell division, cell differentiation, or cell death should occur. Nonetheless, cancerous cells develop self-government from these cell signals, and this causes uncontrollable cell proliferation and growth. When this progression is allowed to carry on, the abnormal cells spread and invade adjoining parts of the

body/organs, and this is referred to as metastasis which is the major cause of cancer-related deaths. To this day, the conventional methods (chemotherapy, radiotherapy, and surgery) of treating cancer have not been sufficiently effective to stop metastasis and completely eradicate cancer, with successful treatments often achieved at the cost of severe side effects.

In recent decades, a new mode of cancer treatment (PDT) has been studied extensively and proposed as a possible alternative to the conventional treatment methods. This technique involves using non-toxic compounds known as photosensitisers (e.g., BODIPY or porphyrin dyes), visible light of a specific wavelength, and molecular oxygen, which is transformed to singlet molecular oxygen initiating the deactivation of cancer cells. Most of the photosensitisers approved by the Food and Drug Administration (FDA) to be used in PDT, such as Photofrin®, suffer from aggregation in aqueous media and relatively weak absorption in the therapeutic window (620−850 nm), poor photostability and chemical heterogeneity. In this thesis, extensive research has been carried out to synthesise novel photosensitisers (BODIPY dyes, porphyrins and their derivatives) with improved properties that enhance their photosensitisation ability for PDT.

1.7 Study objectives

This study aimed to synthesise BODIPY dyes with improved water solubility properties and cationic porphyrins with mitochondria-targeting properties as photosensitising agents for use in both photodynamic therapy and photodynamic antimicrobial chemotherapy.

The specific objectives of this study were:

1) To synthesise and characterise BODIPY dyes with high singlet oxygen quantum yields and improved water solubility.
2) To synthesise and characterise cationic porphyrins and their derivatives that localise in the mitochondria matrix.
3) To conduct *in vitro* photodynamic activities on the MCF-7 breast cancer cell line and HeLa cells (uterine cervical cancer cells) using BODIPY dyes and porphyrins as photosensitisers.
4) To carry out photodynamic antimicrobial activities with *Staphylococcus aureus* as a bacteria strain of choice and BODIPY and porphyrins as photosensitisers.
5) To analyse the electronic structures and optical properties of the BODIPY dyes and porphyrins using molecular modelling.
6) To execute *in silico* docking using human serum albumin human mitochondria ABC transporter.

Chapter 2

Methodology and Experimental

This section contains two parts

1) **Reagents, instrumentation, and successful syntheses**
2) **Failed attempted experiments**

2. MATERIALS AND METHODS

2.1 Materials

2.1.1 Chemicals

2.1.1.1 Reagents for the synthesis of 1-6

2,4-Dimethylpyrrole, 4-(methylthiol)benzaldehyde, ferrocenecarboxaldehyde, 4-pyridinecarboxaldehyde, 4-acetoxybenzaldehyde, 4-morpholinecarboxaldehyde, 3,4-dihydroxybenzaldehyde, trifluoroacetic acid, tetrachloro-1,4-benzoquinone (*p*-chloranil), triethylamine (TEA), boron trifluoride diethyl etherate ($BF_3 \cdot OEt_2$), piperidine, diphenylisobenzofuran (DPBF), N-bromosuccinimide (NBS), N-iodosuccinimide (NIS), bromine, anhydrous sodium sulfate, Methylene Blue, zinc phthalocyanine (ZnPc), Rhodamine 6G and all spectroscopic grade solvents were purchased from Sigma-Aldrich.

2.1.1.2 Reagents for the synthesis of 7 and 8

Distilled pyrrole, propionic acid, benzaldehyde, 4-pyridine carboxaldehyde, triphenylphosphine, 1,4-dibromobutane, (4-bromobutyl)triphenylphosphonium, copper acetate, tin(II) chloride, phosphoryl chloride sodium sulfate (Na_2SO_4) and all spectroscopic grade solvents were purchased from Sigma-Aldrich.

2.1.1.3 Reagents for MTT-assay

MCF-7 breast cancer cell line and HeLa cells were purchased from Cellonex®, fetal calf serum (FCS) and 100 unit/mL penicillin-100 µg/mL streptomycin-amphotericin B were obtained from Biowest®, Dulbecco's phosphate-buffered saline (DPBS) and Dulbecco's modified Eagle's medium (DMEM) were purchased from Lonza®, cell proliferation neutral red reagent (WST-1 assay), trypan blue and tetrazolium MTT (3-

(4,5-dimethylthiazol-2-yl)-2,5-diphenyltetrazolium bromide) dye were obtained from Sigma-Aldrich.

2.1.1.4 Reagents for bacteria studies

Staphylococcus aureus and *Escherichia coli* were purchased from Davies Diagnostic. Nutrient agar was obtained from Merck, and phosphate buffer saline was prepared in the laboratory using appropriate quantities of sodium chloride, potassium chloride, sodium phosphate dibasic, potassium phosphate monobasic, and the water used was ultra-pure Type II obtained from an Elga Purelab Chorus 2 (RO/DI) system (Marlow, UK).

2.1.2 Equipment

- A Shimadzu UV-2550 spectrometer was used to measure ground state electronic absorption spectra at room temperature with a wavelength range of 300−800 nm in a 1 cm path length cuvette.
- Mass spectra were obtained using a Bruker Auto-FLEX III Smartbeam MALDI-TOF mass spectrometer using α-cyano-4-hydroxycinnamic acid as a matrix in either negative or positive ion mode with an m/z range of 400−1500 amu.
- Bruker AMX 600 and 400 MHz and 85 MHz benchtop NMR spectrometers were used to obtain ^{1}H-NMR and ^{13}C-NMR data. The spectra were obtained at ambient temperature using deuterated solvents ($CDCl_3$ and DMSO-d_6).
- Varian Eclipse spectrofluorimeter was used for fluorescence quantum yield studies. Excitation was carried out in the B band region for porphyrins and the main visible region band for BODIPYs at the crossover wavelength of the standard and the PS.
- Singlet oxygen quantum yield studies were carried out using an Ekspla NT 342B-20-AW laser with an Nd:YAG that pumps a 420−2300 nm optical

parametric oscillator (OPO) (355 nm, 2.0 mJ/7 ns, 20 Hz) to provide monochromatic light at a crossover wavelength for the standard and sample. A Thermo Scientific Evolution 350 spectrometer was used to record the degradation of the singlet oxygen quencher (DPBF or DMA) at specific time intervals.

- An Eskpla NT342B-20-AW laser provided the pump beam for an Edinburgh Instruments LP980 transient absorption spectrometer fitted with a PMT-LP (Hamamatsu R928P) and ICCD camera (Andor DH320T-25F03).
- A Ledetect 96 microplate reader was used to obtain the optical density of bacteria in the context of a 96 well plate.
- A Modulight® Medical Laser (ML) 7710-680 system, fitted with a Thorlabs LED that emits light in the wavelength range of a major spectral band of the molecule under study, was used in PDT studies.
- Colony-forming units per millilitre ($CFU.mL^{-1}$) values for bacteria were determined using Scan® 500 automatic colour colony counter.
- The bacteria suspensions were mixed using a vortex mixer from Lasiec.
- Synergy 2 multi-mode microplate reader (BioTek®) was used to measure cell viability.
- The Centre for High Performance Computing in Cape Town was accessed for all theoretical studies.
- Porvair 25 cm^2 vented flasks were used to culture MCF-7 cells; later, 75 cm^2 flasks were used for subculturing. A Zeiss Axio Vert.A1 FL-LED Inverted Microscope with Fluorescence was used to view cells under phase contrast. A binocular tube and phototube (0%/100%) were used for brightfield measurements.

- Magnetic circular dichroism (MCD) was used as an additional optical technique for analyzing ground and excited state degeneracies and identifying the main electronic Q and B bands.

2.2 Synthesis of BODIPY dyes

2.2.1 Synthesis of 1 and 2

BODIPY dyes **1** and **2** were synthesised using previously reported methods.[180–183] 2.1 eq of 2,4-dimethylpyrrole and 1 eq of benzaldehyde of choice were dissolved in a stirring solution of 30 ml of DCM, and 2-3 drops of TFA were added. This reaction mixture was stirred at room temperature under an inert atmosphere. After the depletion of the aldehyde (confirmed using thin-layer chromatography (TLC)), 1.2 eq of *p*-chloranil dissolved in DCM was added at 0°C. The reaction was further stirred for 30 min at room temperature while maintaining an inert atmosphere. A change in colour to purple provided conformation of dipyrromethene formation (**Scheme 2.1**). After 30 min, 10 eq of TEA and $BF_3 \cdot OEt_2$ were added to the reaction at 0°C over a 10 min period, and the mixture was further stirred at room temperature for 18 h. The reaction was then washed with water and dried over anhydrous sodium sulfate, and the solvent was evaporated under reduced pressure. Column chromatography was used to purify the compounds using 1:2 PET: ethyl acetate for **1** and DCM for **2** as eluent. **1** and **2** were obtained (**Scheme 2.1**) as orange and purple crystals, respectively.

BODIPY **1** (1.0 g, yield; 50%), ^{1}H NMR (600 MHz, $CDCl_3$): δ 7.28 (d, J = 8.3 Hz, 2H), 7.12 (d, *J* = 8.4 Hz, 2H), 5.92 (s,2H), 2.49 (s, 6H), 2.48 (s, 3H), 1.37 (s, 6H) ppm ; UV-vis (DMSO) λ, nm (log ε) 500 (5.21).

BODIPY **2** (500 mg, yield; 40%): UV-vis (DMSO) λ, nm (log ε) 535 (5.21); MS (MALDI-TOF): m/z $[M + H]^+$ = 433.50 (calc. 432.10).

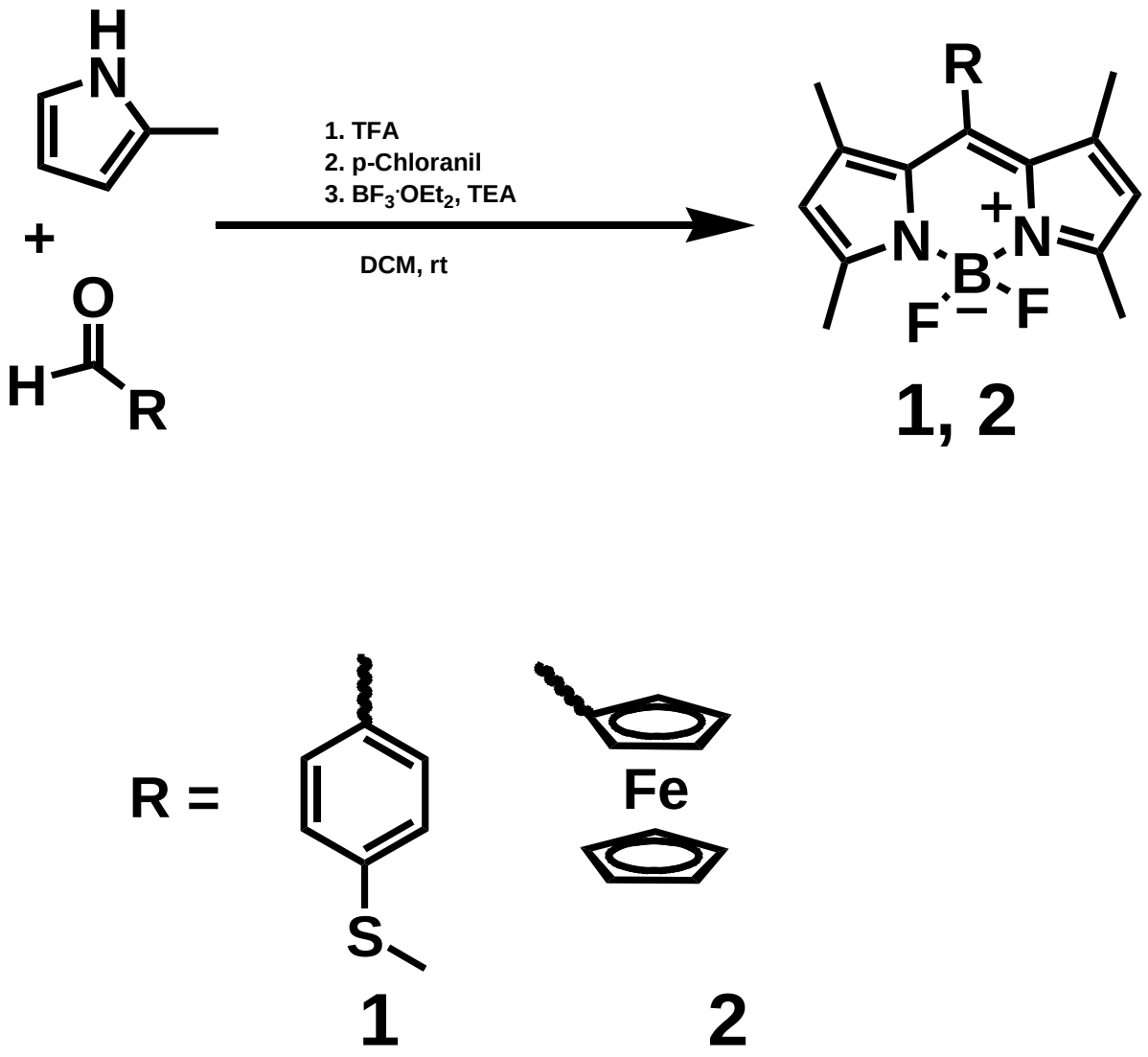

Scheme 2.1 Synthesis of **1** and **2**.[72]

2.2.2 Synthesis of 3, 4 and 5

1 eq of **1** was dissolved in 15 ml of DCM, and to this, 3 eq of bromine/ NIS was added. The reaction was stirred at room temperature under an inert atmosphere, and UV-visible absorption spectroscopy was used to monitor the consumption of **1** to form **3** and **4**. **5** was synthesised by reacting **2** with NIS (**Scheme 2.2**). Silica gel column chromatography was used to isolate the desired product. 1:2 PET/DCM (v/v) was used for **3** and **4**, while DCM was used for **5**.

3 (800 mg, yield;70%): ^{1}H NMR (400 MHz, $CDCl_3$) δ 7.35 (d, *J* = 8.4 Hz, 2H), 7.13 (d, *J* = 8.4 Hz, 2H), 2.58 (s, 3H), 2.54 (s, 3H), 1.54 (s, 3H), 1.41 (s, 3H), 1.23 (s, 3H) ppm; UV-vis (DMSO) λ, nm (log ε), 530 (5.57); MS (MALDI-TOF): m/z $[M]^+$ = 528.45 (calc. 528.06 [$C_{20}H_{19}BBr_2F_2N_2S^+$]).

4 (1 g, yield; 70%): ^{1}H NMR (400 MHz, $CDCl_3$) δ 7.35 (d, *J* = 8.3 Hz, 1H), 7.13 (d, *J* = 8.4 Hz, 1H), 2.61 (s, 3H), 2.53 (s, 2H), 1.43 (s, 3H), 1.23 (s, 10H); UV-vis (DMSO) λ, nm (log ε), 539 (5.61); MS (MALDI-TOF): m/z $[M-H]^+$ = 603.74 (calc. 604.07 [$C_{20}H_{19}BI_2F_2N_2S^+$]).

5 (0.72 g, yield; 60%) : UV-vis (DMSO) λ, nm (log ε) 548 (5.61); MS (MALDI-TOF): m/z for $[M+H-CH_3]^+$ = 576.92 (calc. 575.56), $[M+H-2CH_3]^+$ = 548.84 (calc. 547.81), $[M+H-Br-CH_3)]^+$ = 498.92 (calc. 497.97).

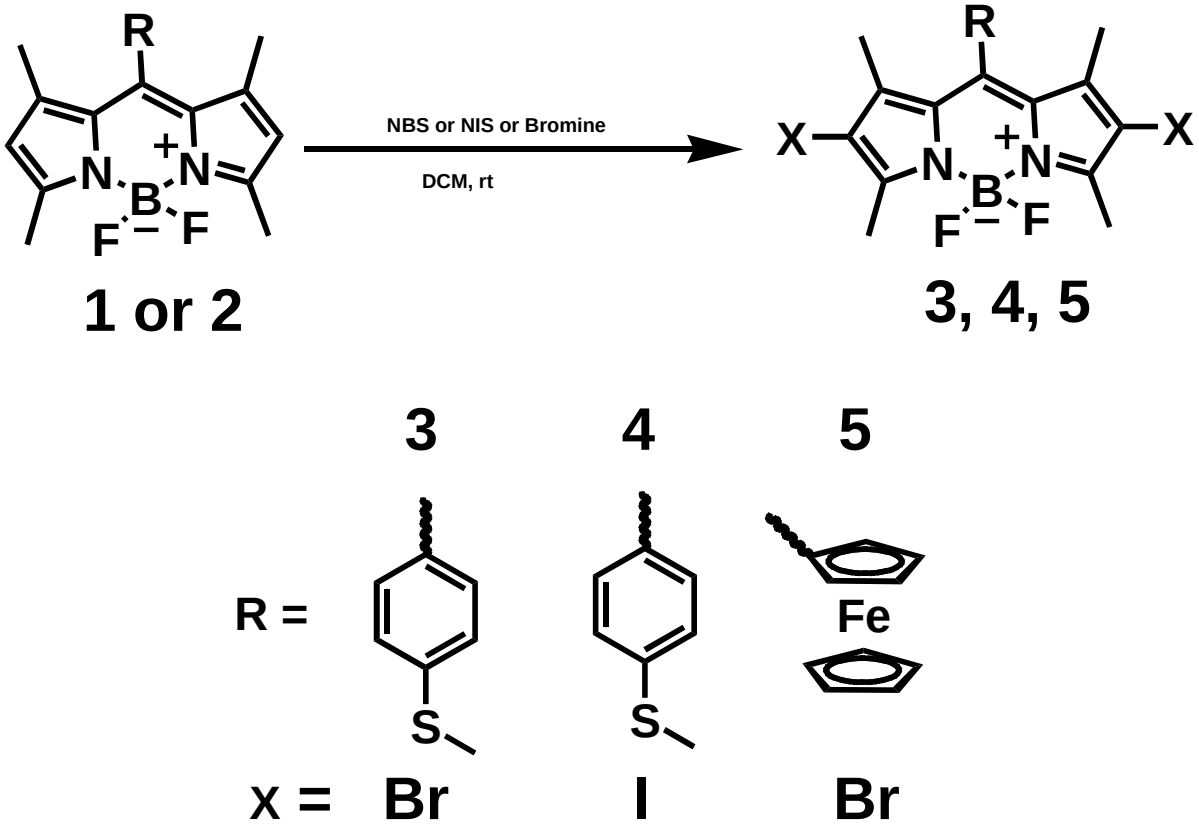

Scheme 2.2 Synthesis of BODIPY dyes **3**, **4** and **5**.[72]

2.2.3 Synthesis of π-extended BODIPY dyes

BODIPY dyes **6**-**9** were synthesised using a well-known Knoevenagel condensation procedure.[180,181] To a round-bottomed flask equipped with Dean-Stark apparatus, 3 eq of pyridine carboxaldehyde was mixed with 1 eq of **3** in benzene, and 1.2 ml of glacial acetic acid and piperidine were added to work up the reaction. This reaction mixture was refluxed until there was no detection of BODIPY dye **2** by UV-visible absorption spectroscopy. The rest of the π-extended BODIPY dyes were synthesised in a similar manner. Column chromatography was used to purify the desired molecules using $CHCl_3$:MeOH 2:1 ratio (**Scheme 2.3**). The use of methanol to isolate **6a** and **6b** led to the hydrolysis of the ester moiety to an alcohol.

6b was synthesised as follows; 1 eq of **6a** was dissolved in DMF, and 2 eq of iodomethane was added, and this reaction was stirred for 24 h at 5°C. After the stated reaction time, **6b** was obtained by centrifuging the reaction mixture in diethyl ether (**Scheme 2.4**).

6a (60 mg, yield; 60%): %): ^{1}H NMR (400 MHz, $CDCl_3$) δ 8.67 (d, *J* = 5.9 Hz, 2H), 8.04 (d, *J* = 16.7 Hz, 2H), 7.86 (d, *J* = 16.7 Hz, 2H), 7.54 (d, *J* = 6.0 Hz, 2H), 7.41 (d, *J* = 8.3 Hz, 2H), 7.20 (d, *J* = 8.3 Hz, 2H), 3.48 (d, *J* = 6.4 Hz, 4H), 2.57 (s, 3H), 1.52 (s,6H); UV−vis (DMSO) λ, nm (log ε) 630 (5.42); MS (MALDI-TOF): m/z $[M + H]^+$ = 708.44 (calc. 706.25 $[C_{32}H_{25}BBr_2F_2N_4S^+]$).

6b (10 mg, yield; 98%): ^{1}H NMR (400 MHz, $CDCl_3$) δ 8.60 (d, *J* = 6.0 Hz, 2H), 7.96 (d, *J* = 16.7 Hz, 2H), 7.78 (d, *J* = 16.7 Hz, 1H), 7.43 (d, *J* = 6.0 Hz, 2H), 7.34 (d, *J* = 8.3 Hz, 2H), 7.20 (d, *J* = 7.4 Hz, 1H), 7.13 (d, *J* = 6.6 Hz, 2H), 2.51 (s, 2H), 2.20 (s, 2H), 1.45 (s, 3H), 1.36 (s, 6H), 1.16 (s, 6H).; UV-vis (DMSO) λ, nm (log ε) 658 (5.28); MS

(MALDI-TOF): m/z [M+H] = 737.07 (calc. 736.36 [$C_{34}H_{31}BBr_2F_2N_4S^+$]), [M – F,$CH_3$]$^+$ = 703.99 (Cald. 704.30), [M + H – S-CH_3]$^+$ = 689.98 (Cald. 690.23).

7a (60 mg. yield; 25%) ^{1}H NMR (400 MHz, DMSO-d_6) δ 10.58 (s, 1H), 9.80 – 9.76 (s, 1H), 7.76 (d, *J* = 8.4 Hz, 8H), 6.93 (d, *J* = 8.4 Hz, 4H), 4.09 (d, *J* = 4.9 Hz, 4H), 3.17 (s, 9H). MS (MALDI-TOF): m/z for [M + H]$^+$ = 831.37 (calc. 830.28 [$C_{34}H_{27}BBr_2F_2N_2O_2S^+$]), [M - OH]$^+$ = 812.29 (calc. 812.33), [M - 2OH,CH_3]$^+$ = 784.27 (calc. 784.25) . UV-vis (DMSO) λ, nm (log ε) 677 (5.73).

7b (70 mg, yield; 30%) ^{1}H NMR (400 MHz, DMSO-d_6) δ 9.77 (s, 1H), 7.75 (d, *J* = 8.4 Hz, 2H), 6.92 (d, *J* = 8.4 Hz, 4H), 4.07 (d, J= 4 Hz, 4H), 3.17 (s, 12H). MS (MALDI-TOF): m/z for [M + H]$^+$ = 727.13 (calc. 726.17 [$C_{27}H_{23}BBr_2F_2N_2OS$]), for [M - F]$^+$ = 708.07 (calc. 708.18); UV-vis (DMSO) λ, nm (log ε) 605 (5.59).

8a (100 mg, yield; 50%) ^{1}H NMR (80 MHz, DMSO-d_6) δ 9.36 (s, 4H), 6.95 (d, *J* = 7.4 Hz, 6H), 6.58 (d, *J* = 7.3 Hz, 4H), 3.30 (d, *J* = 6.8 Hz, 4H), 2.22 (s, 9H). MS (MALDI-TOF): m/z for [M + H]$^+$ = 863.28 (calc. 862.28 [$C_{34}H_{27}BBr_2F_2N_2O_4S^+$]), for [M - F]$^+$ = 844.25 (calc. 844.99); UV-vis (DMSO) λ, nm (log ε) 693 (5.41).

8b (50 mg, yield; 30%); ^{1}H NMR (80 MHz, DMSO-d_6) δ 8.46 (s, 2H), 6.04 (d, *J* = 7.1 Hz, 3H), 5.67 (d, *J* = 8.5 Hz, 4H), 2.04 (d, *J* = 17.2 Hz, 2H), 1.27 (s, 12H). MS (MALDI-TOF): m/z for [M]$^+$ = 742.97 (calc. 742.17), for [M − F]$^+$ = 723.94 (calc. 724.19 [$C_{27}H_{23}BBr_2F_2N_2O_2S^+$]); UV-vis (DMSO) λ, nm (log ε) 619 (5.13).

9a (35 mg, yield; 40%) ^{1}H NMR (80 MHz, DMSO-d_6) δ 6.50 (d, *J* = 8.8 Hz, 2H), 6.20 (d, *J* = 8.5 Hz, 2H), 5.82 (d, *J* = 9.0 Hz, 8H), 2.50 (d, 4H), 1.35 – 1.26 (m, 16H), 0.28 (s, 9H). MS (MALDI-TOF m/z for [M − 2H]$^+$ = 966.61 (calc. 968.49 [$C_{42}H_{41}BBr_2F_2N_4O_2S^+$]), for [M – 3$CH_3$]$^+$ = 926.59 (calc. 926.41), [M + H – (CH_3, BF_2)]$^+$

= 908.54 (calc. 907.66), for $[M - 3CH_3, BF_2]^+$ = 879.49 (calc. 879.61); UV-vis (DMSO) λ, nm (log ε) 714 (5.02).

9b (20 mg, yield; 25%) ^{1}H NMR (80 MHz, DMSO-d_6) δ 6.50 (d, *J* = 8.8 Hz, 2H), 6.20 (d, *J* = 8.5 Hz, 2H), 5.82 (d, *J* = 9.0 Hz, 4H), 2.50 (d, *J* = 5.3 Hz, 2H), 1.35 – 1.26 (m, 8H), 0.28 (s, 9H), 0.13 (s, 3H). MS (MALDI-TOF): m/z for $[M + H]^+$ = 796.12 (calc. 795.28 [$C_{31}H_{30}BBr_2F_2N_3OS^+$]), for $[M - 3CH_3]^+$ = 777.09 (calc. 777.04); UV-vis (DMSO) λ, nm (log ε) 616 (5.78).

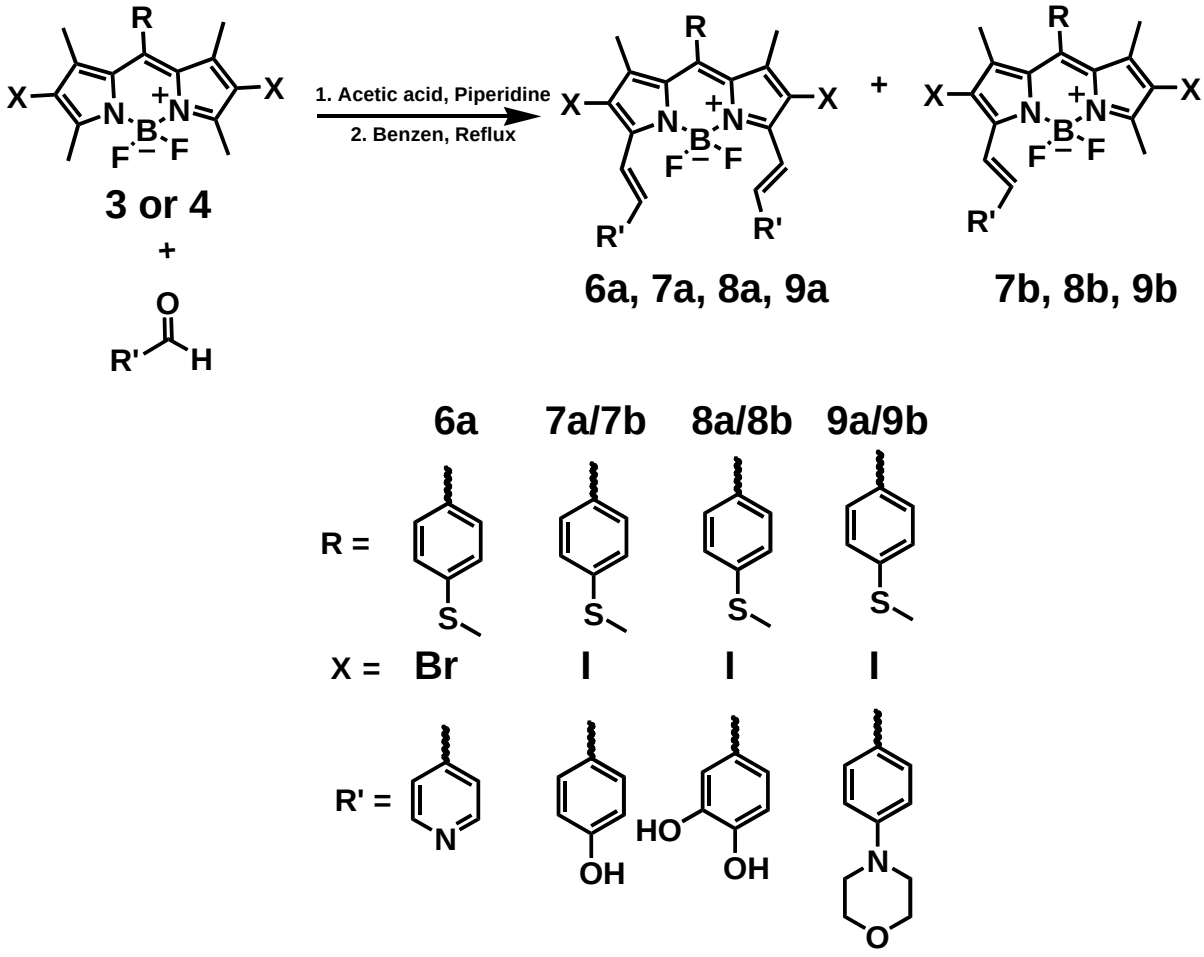

Scheme 2.3 Synthesis of π-extended BODIPY dyes.[189]

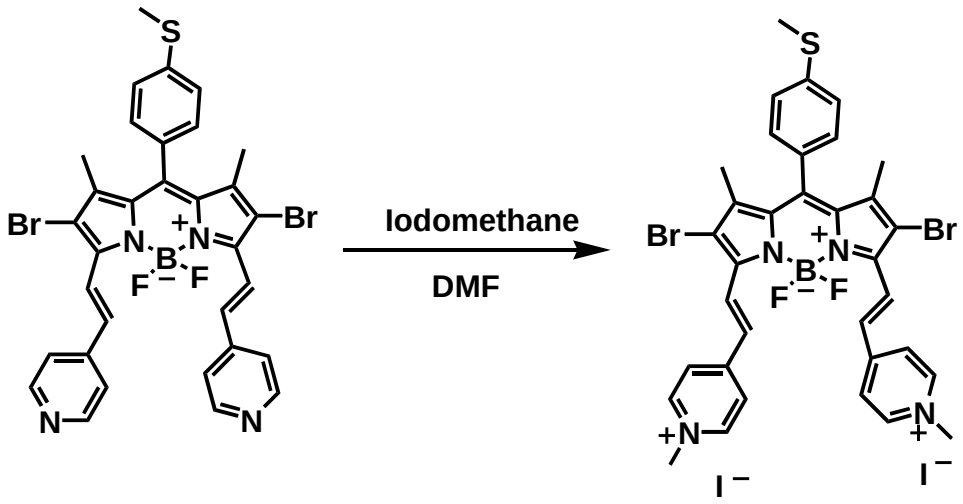

Scheme 2.4 Synthesis of BODIPY dye **6b**.

2.3 Synthesis of porphyrins

2.3.1 Synthesis of the Sn(IV)-porphyrin 10 series

To synthesise **10a**, 1 eq of 4-pyridinecarboxaldehyde was added to propionic acid and refluxed (**Scheme 2.5**). To the refluxing solution, 2 eq of pyrrole was added, and the reflux was continued for 3.5 h. The reaction was cooled, and aqueous sodium hydroxide was then added to neutralise the acid. The desired compound was then extracted using diethyl ether, and the solvent was evaporated using a rotary evaporator. The resulting residue was purified using alumina gel column chromatography and chloroform as the solvent system.

Next**, 10a** (1 eq) was reacted with 2 eq of tin chloride in pyridine under reflux for 3 h and was allowed to cool. The addition of 10 ml of aqueous ammonia followed, and the reaction temperature was raised to 65°C for 1 h. The reaction was allowed to cool again to room temperature, and subsequently, excess water was added to dissolve the metal salt. The Sn(IV)-porphyrin was extracted using chloroform, and the solvent was evaporated using the rotary evaporator. The resulting product was purified using

alumina gel column chromatography and 1:2 solvent ratios of chloroform and methanol, respectively, as a solvent system to obtain **10b** (**Scheme 2.5**).

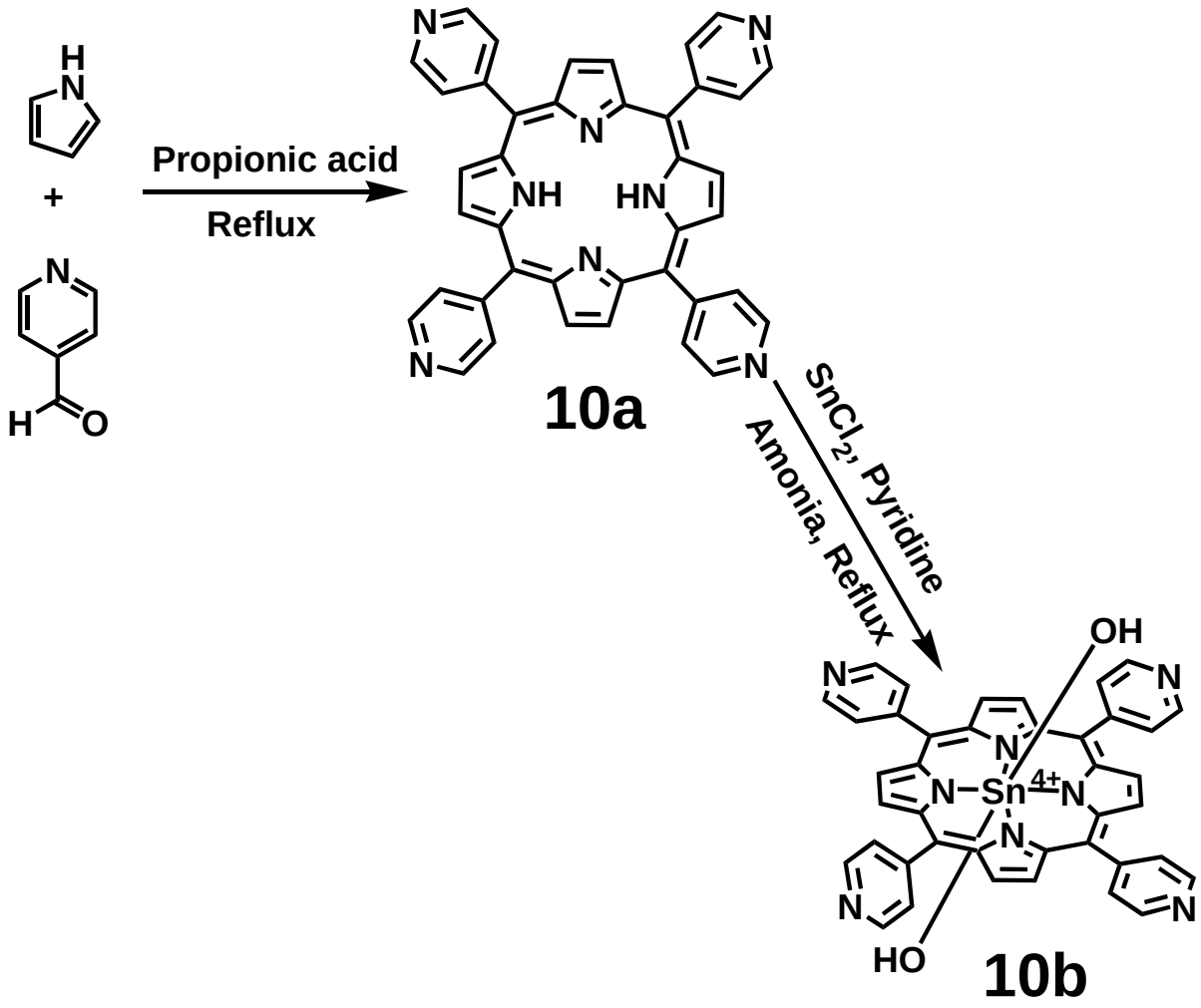

Scheme 2.5 Synthesis of porphyrin **10a** and **10b**.[177]

10c was obtained as follows: to a stirring solution of DMF, 2.1 eq of **10a** and 2 eq of 4-bromobutyltriphenylphosphonium (**TPP**) were added. This mixture was stirred at room temperature for 24 h. Porphyrin **10c** was obtained by centrifuging the reaction mixture in diethyl ether as a brown solid (**Scheme 2.7**).

TPP was synthesised by adding 1 eq triphenylphosphine and 1 eq 1,4-dibromobutane in xylene, and the reaction was refluxed for 24 h. The desired product was obtained by washing with diethyl ether[178] (**Scheme 2.6**).

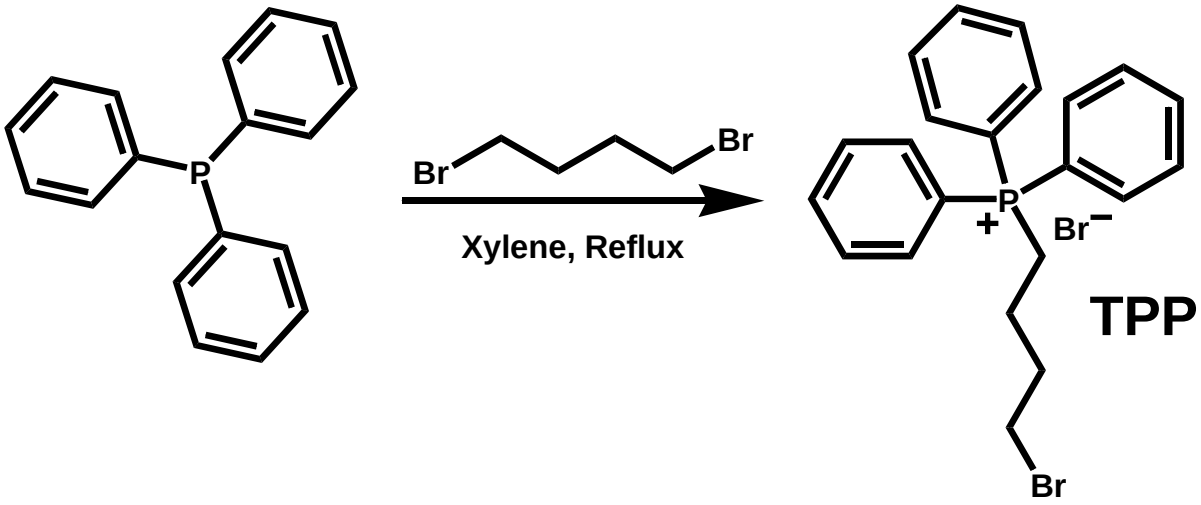

Scheme 2.6 Synthesis of **TPP**.[178]

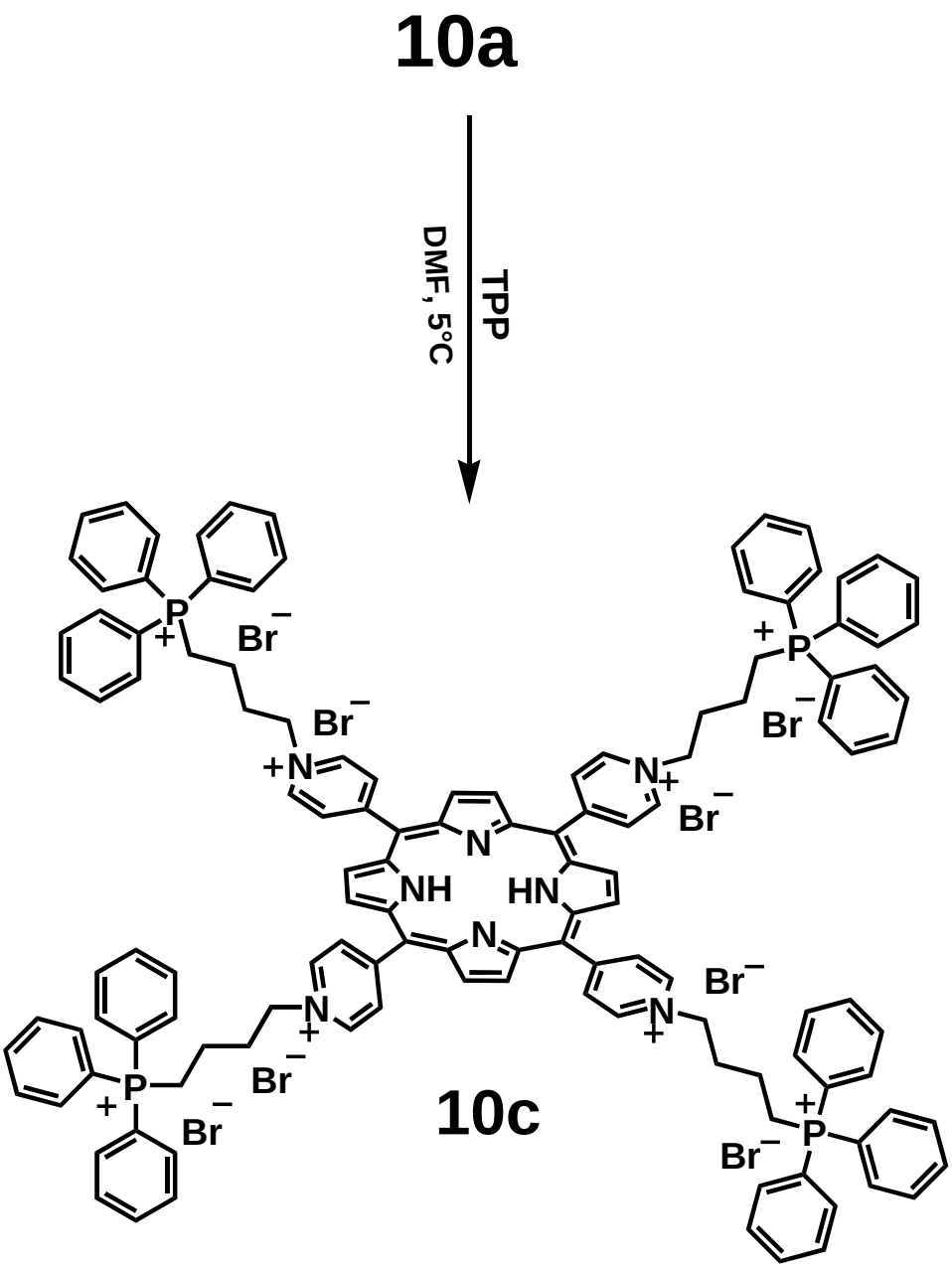

Scheme 2.7 Synthesis of **10c**.[177]

10d was synthesised from the **10b**. To a stirring solution of DMF, 2.1 eq of **10b** and 2 eq of **TPP** were added and stirred for 24 h. To obtain **10d**, the reaction mixture was washed with diethyl ether and then centrifuged. **10d** was obtained as a purple solid (**Scheme 2.8**).

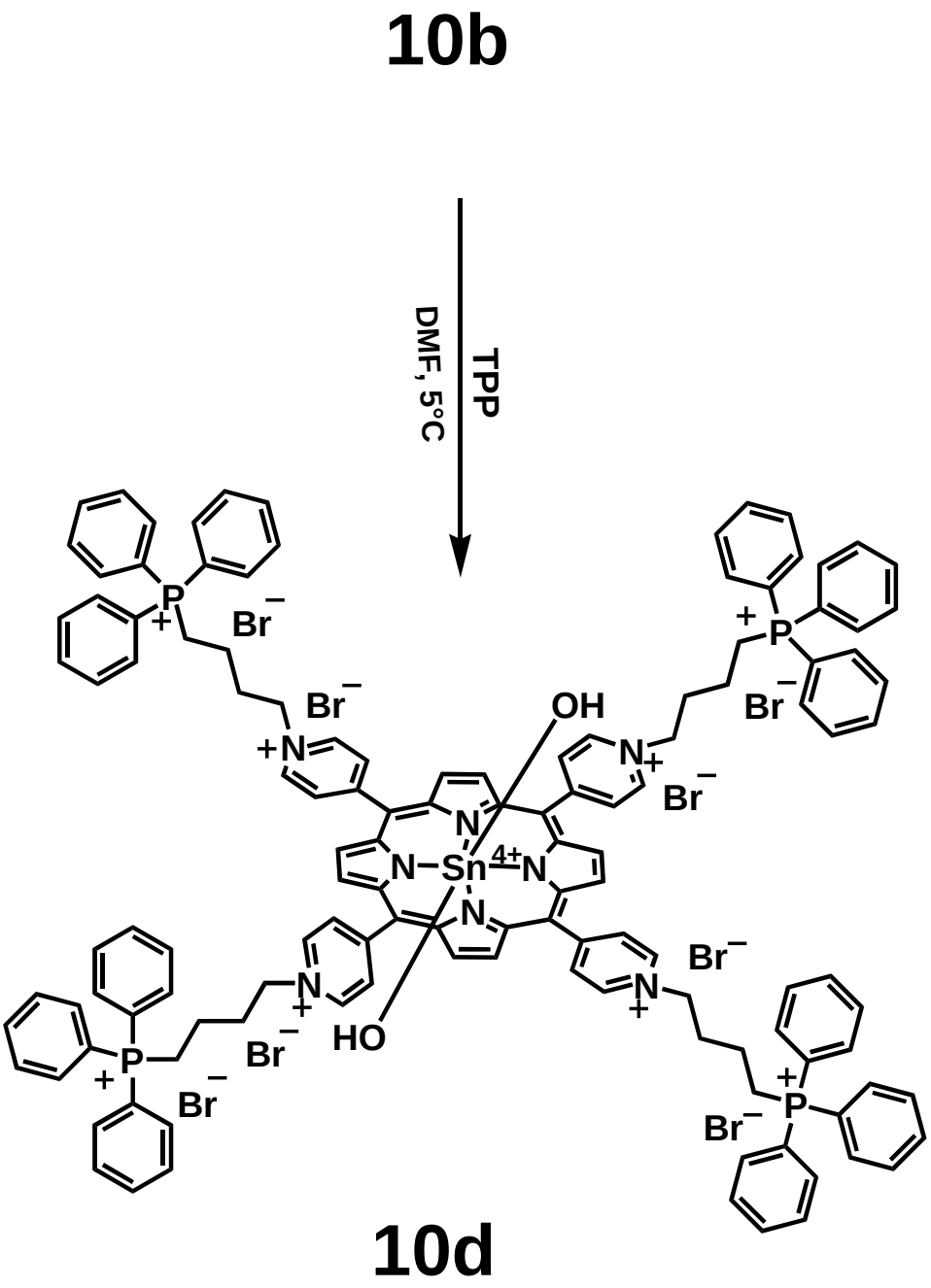

Scheme 2.8 Synthesis of **10d**.[177]

Lastly, for the porphyrin **10** series, 1 eq of **10d** was reacted with 4-hydroxypyridine under reflux in chloroform/methanol solution mixture (2:1 solvent ratio) for 3 h. The reaction was cooled, the solvent evaporated using a rotary evaporator, and the desired product **10e** was obtained by alumina gel column chromatography and chloroform as the mobile phase. The desired product was isolated as a purple solid (**Scheme 2.9**).

MALDI-TOF MS parent peaks could only be obtained for **10a** and 1**0b**, but ^{1}H NMR spectra were obtained for the entire porphyrin **10** series.

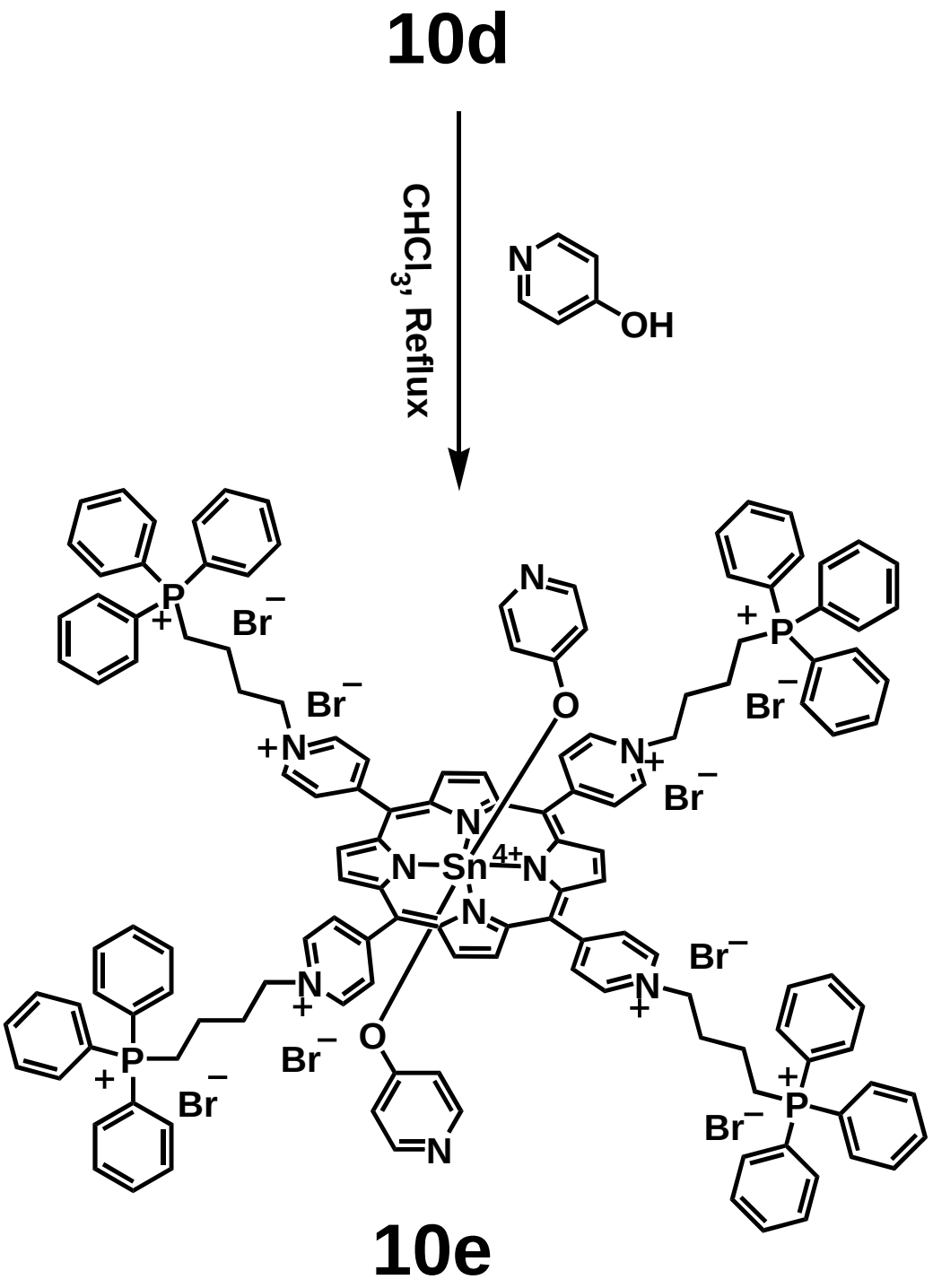

Scheme 2.9 Synthesis of porphyrin **10e**.[138]

TPP (2 g, yield; 98%); ^{1}H NMR (400 MHz, MeOD) δ 4.19 (q, *J* = 7.1 Hz, 2H), 3.65 (t, *J* = 6.3 Hz, 2H), 3.44 (q, *J* = 7.3 Hz, 2H), 3.38 – 3.32 (m, 2H), 2.08 – 2.02 (m, 3H), 1.95 (dd, *J* = 15.4, 7.5 Hz, 3H), 1.41 (t, *J* = 7.2 Hz, 6H), 1.33 (t, *J* = 7.1 Hz, 3H). [$C_{22}H_{23}BrP^{+}$]

10a (100 mg, yield; 40%); ^{1}H NMR (80 MHz, $CDCl_3$) δ 7.62 (d, *J* = 7.3 Hz, 16H), 6.14 (d, *J* = 7.4 Hz, 10H); MS (MALDI-TOF): m/z for $[M + H]^{+}$ = 619.24, (calc. 618.69 [$C_{40}H_{26}N_8$]).

10b (50 mg, yield; 95%); ^{1}H NMR (80 MHz, $CDCl_3$) δ 7.71 (d, *J* = 7.1 Hz, 16H), 6.18 (d, *J* = 7.1 Hz, 10H); MS (MALDI-TOF): m/z for $[M + H]^{+}$ = 771.18, (calc. 770.12 [$C_{40}H_{26}N_8O_2Sn^{4+}$]).

10c (20 mg, yield; 95%); ^{1}H NMR (80 MHz, $CDCl_3$) δ 9.63 (d, *J* = 6.5 Hz, 26H), 7.83 – 7.60 (m, 60H), 5.19 – 4.90 (m, 10H), 3.97 – 3.47 (m, 10H), 1.91 (m, 12H); UV-vis (DMSO) λ, nm (log ε) 427 (5.60), 521 (4.62), 558 (4.79),596 (4.32), 657 (4.01). [$C_{128}H_{118}N_8O_2P_4$]

10d (19 mg, yield; 95%); ^{1}H NMR (400 MHz, DMSO-d_6) δ 7.77 (d, *J* = 13.8 Hz, 8H), 7.53 (t, *J* = 12.2 Hz, 16H), 7.46 – 7.37 (m, 60H), 5.37 (s, 2H), 2.13 (m, 16H), 1.42 (m, 8H), 1.22 (m, 8H); UV-vis (DMSO) λ, nm (log ε) 427 (5.62), 563 (5.03), 604 (4.10), 640 (4.32). [$C_{128}H_{118}N_8O_2P_4Sn^{10+}$]

10e (15 mg, yield; 98%); ^{1}H NMR (400 MHz, $CDCl_3$) δ 7.89 (d, *J* = 13.8 Hz, 4H), 7.63 (d, *J* = 6.6 Hz, 12H), 7.53 (d, *J* = 12.2 Hz, 60H), 5.49 (s, 2H), 3.85 (d, *J* = 6.2 Hz, 6H), 2.48 (d, *J* = 17.7 Hz, 8H), 2.25 (d, *J* = 13.6 Hz, 16H), 1.53 (m, 6H), 1.34 (d, *J* = 6.0 Hz, 10H); UV-vis (DMSO) λ, nm (log ε) 424 (4.96), 561(5.21), 603 (4.53),634 (4.56). [$C_{138}H_{124}N_{10}O_2P_4Sn^{10+}$]

2.3.2 Synthesis of the β-substituted porphyrin 11 series

The precursor molecule, **PyB**, was synthesised by reacting equimolar amounts of 4-methylpyridine with bromobutane in toluene under reflux for 24 h (**Scheme 2.10**). The solid that formed after the reaction was cooled, washed with diethyl ether and stored in a desiccator.[178]

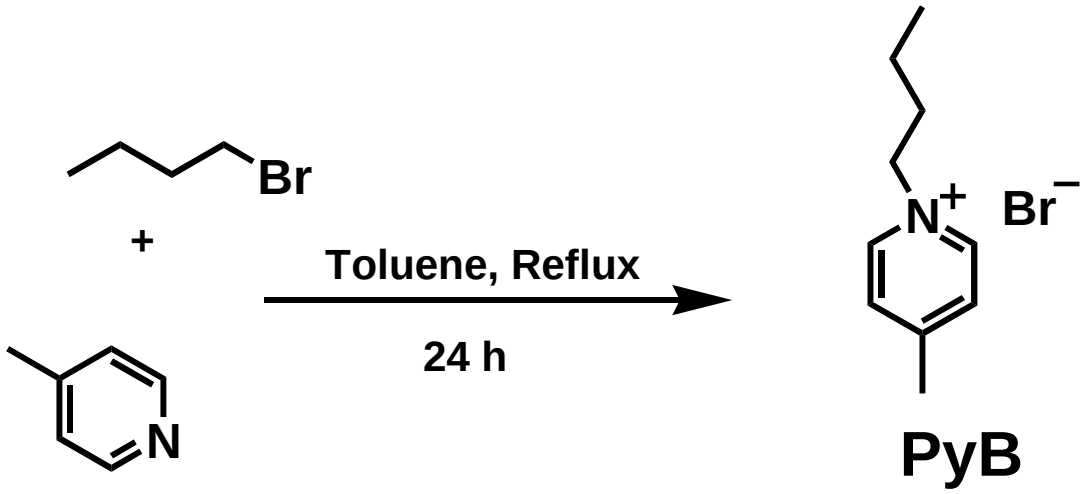

Scheme 2.10 Synthesis of the **PyB** precursor.[178]

Porphyrin **11a** was synthesised from formyl-tetraphenylporphyrin (**f-TPP**) and **PyB**.[178] Firstly, 1 eq of benzaldehyde was reacted with 2 eq of pyrrole in refluxing propionic acid for 3 h, and then the reaction was cooled. After cooling, the tetraphenylporphyrin product (**TPP'**) was obtained by vacuum filtration as purple solids. No further purification was required.

1 eq of **TPP'** was dissolved in chloroform, and when the mixture began to reflux, 2 eq of copper(II) acetate dissolved in methanol was added. This reaction was refluxed for a further 3 h, and after this reaction time, it was cooled. Water was added to dissolve the metal salt, and the copper porphyrin (**Cu-TPP'**) was extracted using chloroform.

The solvent was evaporated using a rotary evaporator, and the product obtained was washed with methanol and filtered to obtain a pure **Cu-TPP'**. Thirdly, 1.4 eq of dry DMF was added to the round-bottomed flask at 0°C under argon, and to this stirring solution, 1 eq of phosphoryl (IV) chloride was added. Stirring was continued until the formation of a golden-coloured slurry solution. Afterwards, 1 eq of **Cu-TPP'** dissolved in dichloroethane (DCE) was added, and the argon source was replaced with a drying tube. The reaction was warmed to room temperature, refluxed for 5 h, and cooled overnight. 20 ml of sulfuric acid was added, and stirring lasted for 10 min, and the resulting green two-phase solution was poured into ice-cold aqueous sodium hydroxide (51 g, 2 L). The compound of interest, **formyl-TPP'**, was extracted using chloroform, and the organic phase was washed with aqueous $NaHCO_3$ twice. The organic layer was then dried over anhydrous sodium sulfate, and the solvent was evaporated. Pure **formyl-TPP'** was obtained by silica gel chromatography using a 2:1 DCM/hexane solvent system (**Scheme 2.11**).

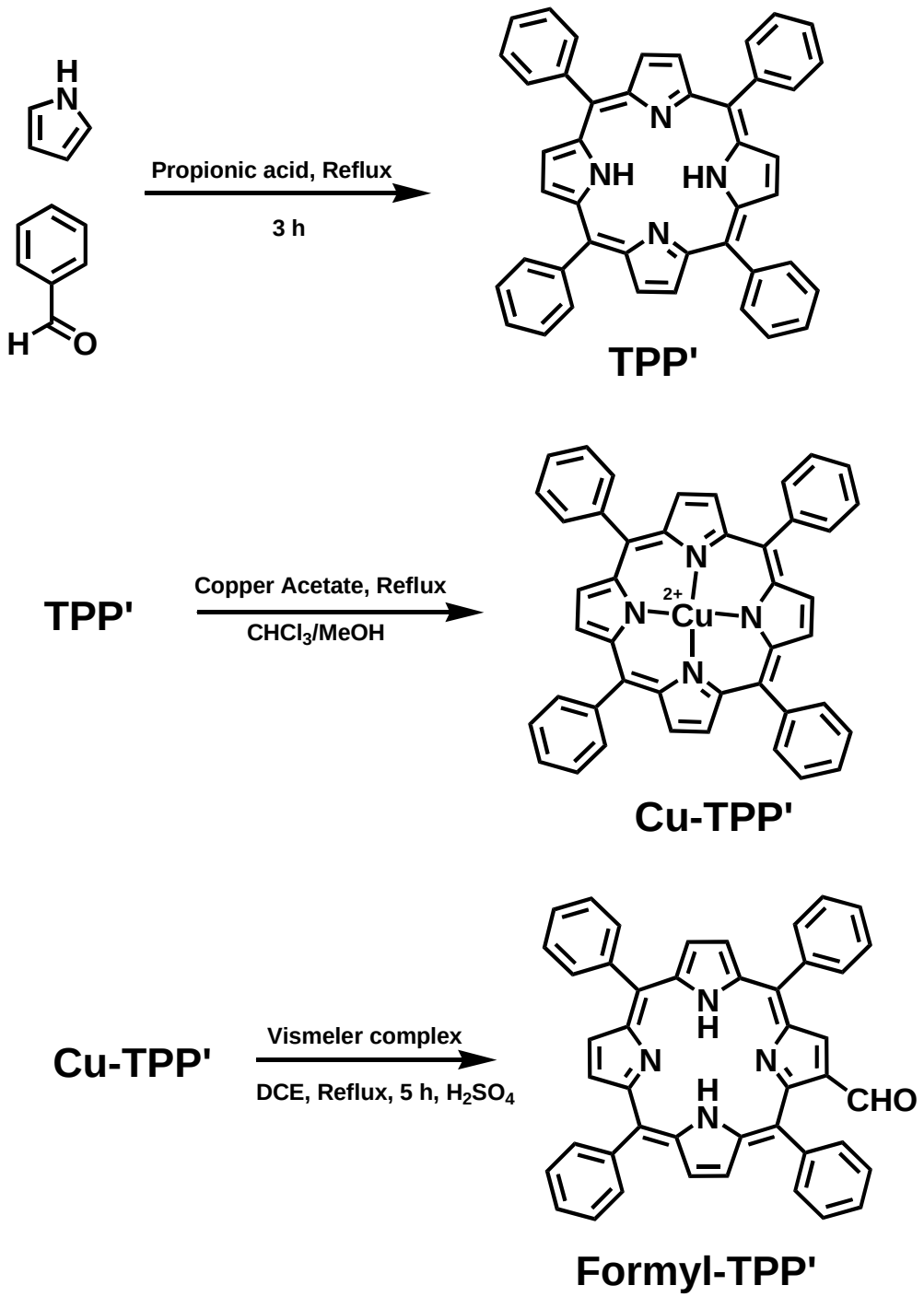

Scheme 2.11 Synthesis of **formyl-TPP'**.[145,146]

Lastly, to obtain **11a**, 1 eq **formyl-TPP'** was added to a stirring solution of 6 eq of K_2CO_3 in THF/methanol (2:1 ratio) maintained at 30°C. After 15 min of stirring, 2.1 eq of **PyB** was added and stirring continued for 1 h (**Scheme 2.12)**. The mixture was cooled to room temperature, and the solvent was evaporated under reduced pressure.

The residue was dissolved in chloroform and washed with water and brine. The organic phase was dried over anhydrous sodium sulfate, and the desired product (**11a**) was isolated from the crude material by column chromatography (silica gel; eluent: DCM/methanol = 9:1).[145]

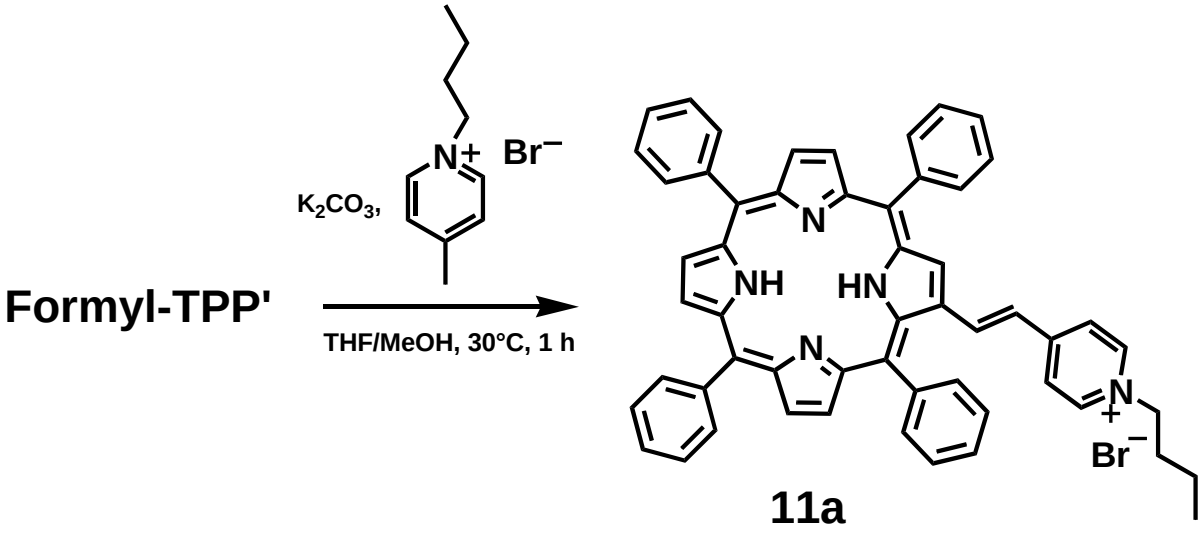

11a

Scheme 2.12 Synthesis of **11a**.[145]

In a similar manner to the analogous reactions for the porphyrin **10** series, the exact procedures reported in **Schemes 2.5** and **2.9** were followed for metalation of **11a** to obtain **11b** and the addition of 4-pyridyloxy axial ligands to obtain **11c** (**Scheme 2.13**).

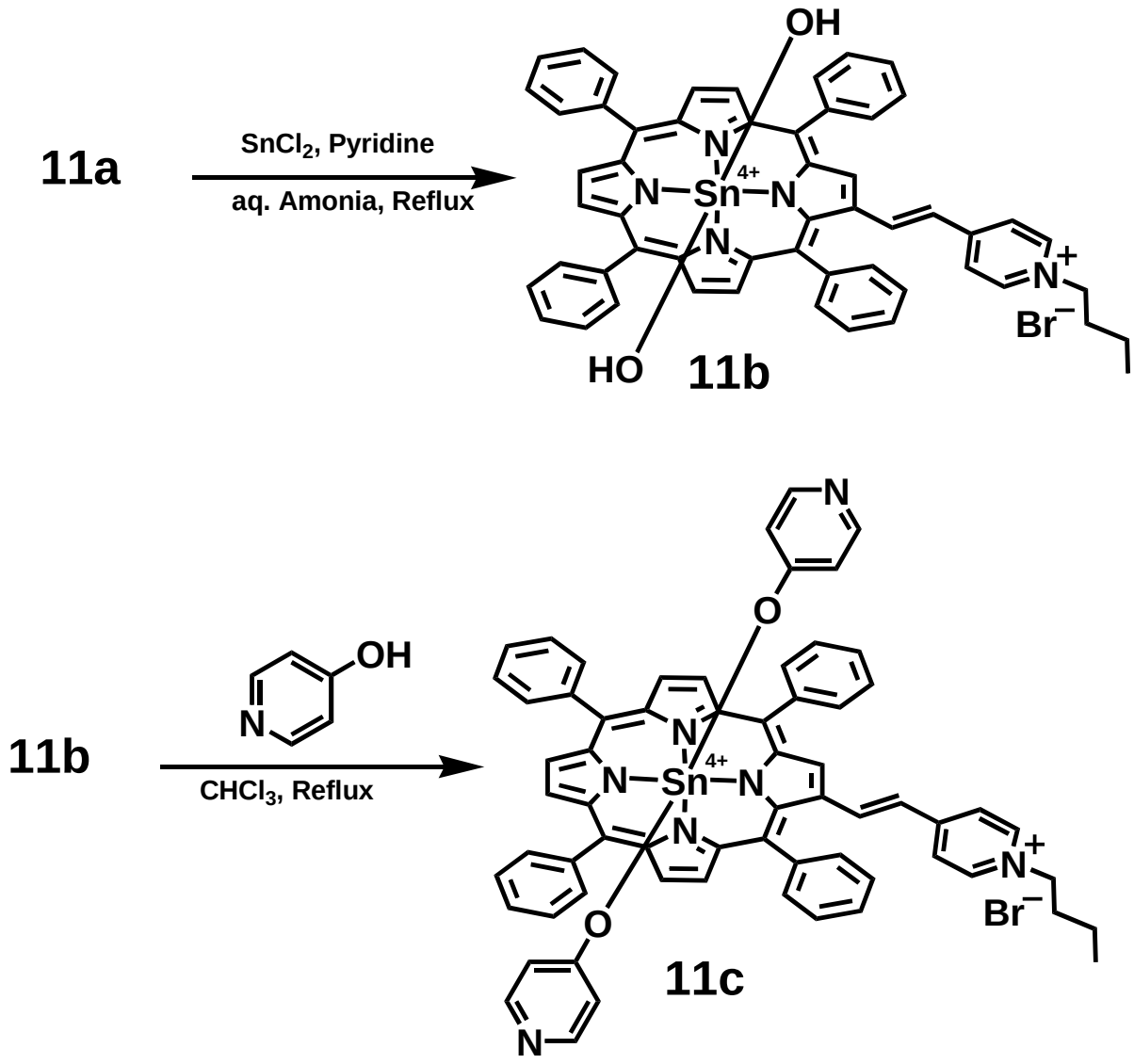

Scheme 2.13 Synthesis of porphyrins **11b** and **11c**.[138]

PyB (20 mg, yield; 98%); ^{1}H NMR (80 MHz, DMSO-d_6) δ 8.80 (d, J = 6.7 Hz, 2H), 7.70 (d, J = 6.3 Hz, 2H), 4.31 (t, J = 7.2 Hz, 2H), 2.79 (s, 3H), 1.75 – 1.32 (m, 2H), 0.91 (dd, J = 15.0, 6.7 Hz, 2H), 0.52 (t, J = 6.8 Hz, 3H). [$C_{10}H_{16}N^+$]

11a (60 mg, yield; 50%); ^{1}H NMR (80 MHz, $CDCl_3$) δ 7.16 (d, J = 8.2 Hz, 33H), 3.08 – 2.76 (m, 8H), 1.49 – 1.22 (m, 3H); MS (MALDI-TOF): m/z for $[M]^+$ = 774.61 (calc. 774.92 [$C_{55}H_{44}N_5^+$]); UV-vis (DMSO) λ, nm (log ε) 422 (4.82), 538 (4.63), 651 (5.20).

11b (15 mg, yield; 40%); ^{1}H NMR (80 MHz, $CDCl_3$) δ 9.68 (d, *J* = 6.3 Hz, 10H), 9.12 (d, *J* = 3.3 Hz, 10H), 7.74 (d, *J* = 4.8 Hz, 13H), 5.02 (d, *J* = 8.2 Hz, 2H), 3.97 – 3.53 (m, 6H), 2.18 – 1.68 (m, 3H); MS (MALDI-TOF): m/z for $[M + H]^+$ = 926.23 (calc. 925.68 $[C_{55}H_{44}N_5O_2Sn^{5+}]$); UV-vis (DMSO) λ, nm (log ε) 427 (5.32), 563 (4.56), 604 (4.53),640 (4.36).

11c (13 mg, yield; 30%); ^{1}H NMR (80 MHz, $CDCl_3$) δ 8.88 (d, *J* = 6.3 Hz, 7H), 8.30 – 8.16 (m, 20H), 7.86 – 7.68 (m, 12H), 3.77 (m, 2H), 1.95 – 1.91 (d, *J* = 4.7 Hz, 2H), 1.87 – 1.78 (m, 4H), 1.39 – 1.26 (m, 3H); MS (MALDI-TOF): m/z for $[M + H]^+$ = 1081.73 (calc. 1079.84 $[C_{65}H_{50}N_7O_2Sn^{5+}]$), for $[M - 3CH_3]^+$ = 1037.71 (calc. 1037.36), [M+H-(C_6H_5, CH_3, $2(CH_2CH)$]$^+$ = 947.64 (calc. 907.66), for $[M- 2L]^+$ = 925.55 (calc. 925.68); for [M- (2L-2OH)]$^+$ = 829.54 (calc. 829.24), for [M-(2L, CH_3, $2(CH_2CH)$]$^+$ = 835.55 (calc. 835.55); UV-vis (DMSO) λ, nm (log ε) 429 (4.51), 569 (4.62), 619 (4.36).

2.4 Photodynamic anticancer activity studies

2.4.1 Cell studies

The *in vitro* cytotoxicity studies for all the molecules were evaluated against MCF-7 and HeLa cells by using the MTT assay.[169] The cancerous cell lines were cultured in Dulbecco's modified Eagle's medium (DMEM) that contained 10% fetal bovine serum (FBS) and 0.01% antibiotics (penicillin and streptomycin-amphotericin B) in separate T75 cm^2 cell culture flasks. The cells were incubated at 37°C with a 5% CO_2 supply until they had attained a 100% growth confluence. The cells were then seeded (1 × 10^4/ well) in 96-well plates in DMEM medium and incubated for 24 h in an incubator with a 5% CO_2 supply. After this incubation, the old medium was replaced with a new DMEM medium containing different concentrations of compound (0.4−100 μM), and the cells were again incubated in the dark for 24 h. A separate set of 96-well plates were filled with fresh DMEM that did not contain the synthesised molecules, and these

plates were treated as controls. When the stated incubation period had elapsed, the medium containing the compounds was discarded and fresh DMEM without phenol red was added.

Next, the cells were irradiated for 30 min with a Thorlabs LED of appropriate wavelength for the compound under investigation mounted onto the housing of a Modulight 7710-680 medical laser. The clear DMEM medium was discarded, fresh DMEM-10% FBS was added, and the cells were incubated for a further 24 h. An additional set of cells treated with the compounds were prepared, and no irradiation was performed. These cells were incubated for 24 h, and after this time, the medium was removed, DMEM-10% FBS was added, and the cells were incubated for an additional 24 h.

After 24 h of incubation for both sets of cells, the medium was carefully discarded, 25 µL (5 mg/mL) MTT (dissolved in PBS (phosphate-buffered saline)) was added to each well, and the cells were incubated for 3 h in the dark. Afterwards, the medium was discarded carefully, and 200 µL of DMSO was added to dissolve the formazan crystals that formed. The absorbance of formazan at 545 nm was determined using a Molecular Devices Spectra Max M5 plate reader (**Figure 2.1**). The measure of cytotoxicity is obtained from the percentage ratio of the absorbance of the treated cells to the untreated controls. The IC_{50} values were determined by nonlinear regression analysis using GraphPad prism.

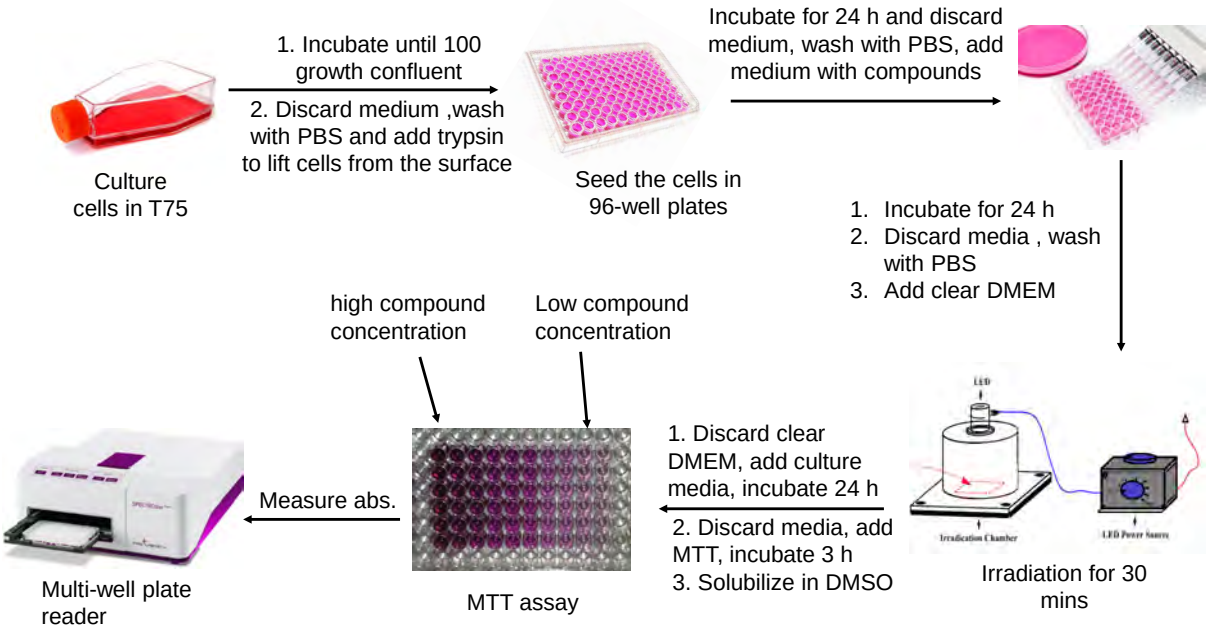

Figure 2.1 Schematic representation of MTT assay cytotoxicity protocol.

2.4.2 Cellular uptake

Time-dependant cellular uptake studies for the synthesised molecules were carried out at 6 μM according to reported methods.[184] A solution of the PS (6 μM) was added to the MCF-7 or HeLa cells seeded in 24 well cell culture plates, and incubation was carried out at regular intervals (6, 12, 24, 48 h). Consequently, the cells were washed with PBS, lysed with 30 μL of Triton-100X and solubilised with 70 μL of DMSO. The relative cellular uptake was monitored at the absorbance maxima of each molecule with an ELISA reader, and control experiments were carried out in the absence of the PS.

2.5 Lipophilicity

The shake-flask method (**Figure 2.2**) was used to determine the lipophilicity (log $P_{o/w}$) of the molecules under investigation.[184] 1 mg of the compounds were dissolved in 3 mL of 1-octanol, and the absorbance was measured (A_{int}). To this solution, 3 mL of

Millipore water was added, and the mixture was stirred for 3 h at room temperature. After 3 h, the mixture was allowed to separate into organic and aqueous phases, and the absorbance of the organic phase was measured (A_{oct}). A_{oct} was subtracted from A_{int} to derive A_{wat}, which represents the absorbance value of the compound in the aqueous phase. The log $P_{o/w}$ values were determined using the following formula, log P = log (A_{oct} / A_{wat}).[184]

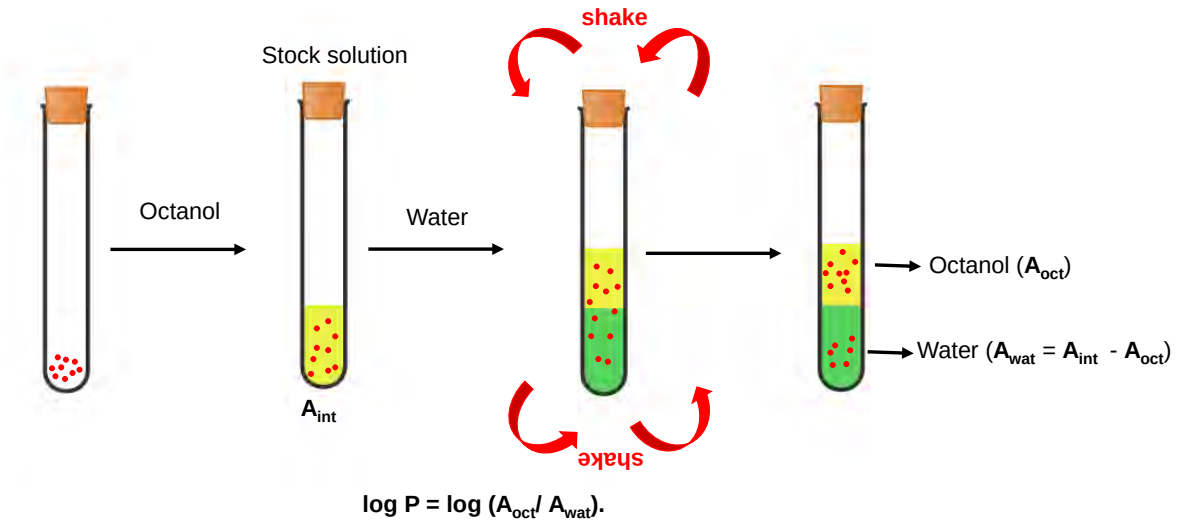

Figure 2.2 Shake flask method schematic illustration.

2.6 Photostability

Photostability studies were carried out in 1% DMSO/PBS solution of the compounds under investigation. This solution was irradiated at regular time intervals (6−30 min) using a Thorlabs LED of appropriate wavelength in the same arrangement used for the *in vitro* cell studies.

2.7 Antimicrobial method

Gram-(+) *Staphylococcus aureus* (ATCC®25923) was used for the antimicrobial activity studies. The bacteria were grown on an agar plate according to the

manufacturer's specifications to obtain an individual colony. Reported procedures in the literature were followed in the preparation of bacteria cultures.[178] The colony was inoculated into the nutrient broth and was incubated under agitation on a rotary shaker overnight at 37°C. The aliquots of the culture were later transferred to 5 mL of fresh broth and incubated to obtain a mid-logarithmic phase (OD 620 nm ≈ 0.6). A Ledetect 96 from Labxim Products was used to measure the optical density (OD) of the bacteria culture so that the log reduction values could be calculated in $CFU.mL^{-1}$. Once an optical density between 0.6 and 0.7 was observed, the broth was washed by centrifuging (4000 rpm for 10 min × 3) using PBS. The bacteria residues were resuspended in 100 mL PBS as the bacterial stock solution with a dilution factor of 10^{-2}.

The stock solutions of the compounds were prepared in 2% DMSO. A series of new stock bacteria-PS stock solutions were prepared with concentrations ranging from 2.5−80 μM. The bacteria-PS solutions were incubated for 30 min to internalise the PS, and later 3 mL (from a 6 mL stock solution of bacteria-PS) was pipetted into two separate 24-well plates. One plate was irradiated using a Thorlabs LED of appropriate wavelength mounted onto a Modulight 7710-680 medical laser for 90 min, while the other plate was kept in the dark (**Figure 2.3**). After 90 min, 100 μL for each sample concentration was pipetted out onto Petri dishes with nutrient agar. The plates were incubated at 37°C for 24 h in the dark. A Scan 500 Automatic Colony Counter from the Healthcare Technologies was used to measure the CFU values for the colonies that formed. A concentration dependence study was conducted to select a suitable PS concentration that exhibited optimal antimicrobial activity properties for subsequent time-dependence studies.

For irradiation time dependence studies, the same procedure described above was followed in preparing the bacteria-PS solution and placing the solution in 24-well plates. After each 10 min of irradiation, 100 µL of sample was pipetted out onto Petri dishes with nutrient agar, incubated for 24 h and CFU counting was carried out in a similar manner to that described above. The survival fractions were determined by comparing the control (Petri dishes with only bacteria) to those incubated with the PS. The studies were carried out in triplicate so a standard deviation can be determined.

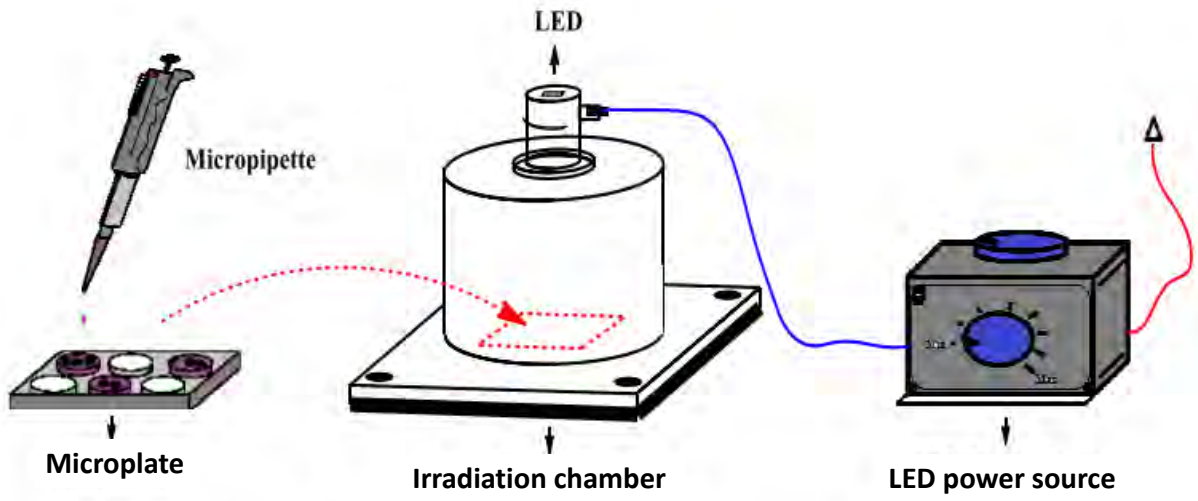

Figure 2.3 Schematic representation of antimicrobial light studies.

2.8 In silico studies

2.8.1 Time dependence density functional theory

Density functional theory (DFT) and time-dependent density functional theory (TD-DFT) were carried out by using the B3LYP exchange-correlation functional of the Gaussian 09 software package (version E01).[184] Geometry optimisations were performed at the B3LYP/6-31G(d) or B3LYP/SDD level of theory. The optimised B3LYP geometries were used to carry out excited state TD-DFT calculations by using

the CAM-B3LYP functional, which introduces a long-range correction. The visualisation of the generated MOs was carried out with Gassview or Chemcraft.

2.8.2 Molecular docking

2.8.2.1 Ligand and protein preparation

The three-dimensional structure of 5z0b of human serum albumin (HSB) was obtained from the Protein Data Bank[185] in pdb format. The protein was opened on BIOVIA Discovery Studio Visualizer 2020, and water molecules were removed along with other unnecessary ligands. The revised file was also saved in pdb format. Autodocks Tools-1.5.6 was used to modify the protein. The native ligand was removed, and the protein was saved as an apoprotein in pdb and pdbqt format. The ligands were constructed using ChemDoodle2D and loaded on BIOVIA Discovery Studio Visualizer 2020. Their geometry was cleaned after the addition of hydrogens. The ligands were converted to xyz files using the babel command, while the xtb –opt command was used for geometry optimisation, and the babel command was again used to convert the ligands to pdb format.

2.8.2.2 Active site determination

The co-crystallised protein was opened in BIOVIA Discovery Studio Visualizer 2020 to open the xyz atom attributes of the receptor site. After the xyz values were obtained, the apoprotein (pdbqt file) was opened in Autodocks, and a grid box was developed in the receptor region.

2.8.8.3 Receptor-ligand docking

The pdbqt files of the ligand and the protein were loaded on Autodocks Tools 1.5.6 to generate the grid parameter and docking parameter files. These files were transferred to the cluster, Autogrid was run to generate the maps, and docking was conducted. Later, the lowest energy ligand docking structure was visualised in Discovery studio.

2.8.8.4 Validation of the target protein-ligand binding

The native ligand was constructed using Chemdoodle. Its geometry was cleaned using BIOVIA Discovery Studio Visualizer 2020 and was optimised using the xtb command. Docking was carried out as described above.

2.9 Failed attempted synthesis

This section outlines the attempted synthetic procedures for a series of asymmetric porphyrin target structures that were rationally selected as potential photosensitizer dyes for photodynamic therapy.

2.9.1 Synthesis of β-substituted tetrapyridylporphyrin

1 eq of **10a** was dissolved in chloroform and refluxed. To this solution, 2 eq of copper acetate dissolved in methanol was added. The mixture was refluxed for 3 h, cooled, washed with water and the desired tetrapyridylporphyrin product (**TPYP**) was extracted with chloroform. After drying, the compound was added to a stirring solution of DMF and phosphoryl(IV) oxychloride (Vilsmeier complex) to form **formyl-tpyp** (**Scheme 2.14**). After purification by silica gel column chromatography, mass spectrometry was used for characterisation, and the mass of both **TPYP** and **formyl-tpyp** was not detected. After several attempts, the mass of **formyl-tpyp** could still not be detected. Thus, we could not proceed to prepare **12** and **12a** (**Scheme 2.14**).

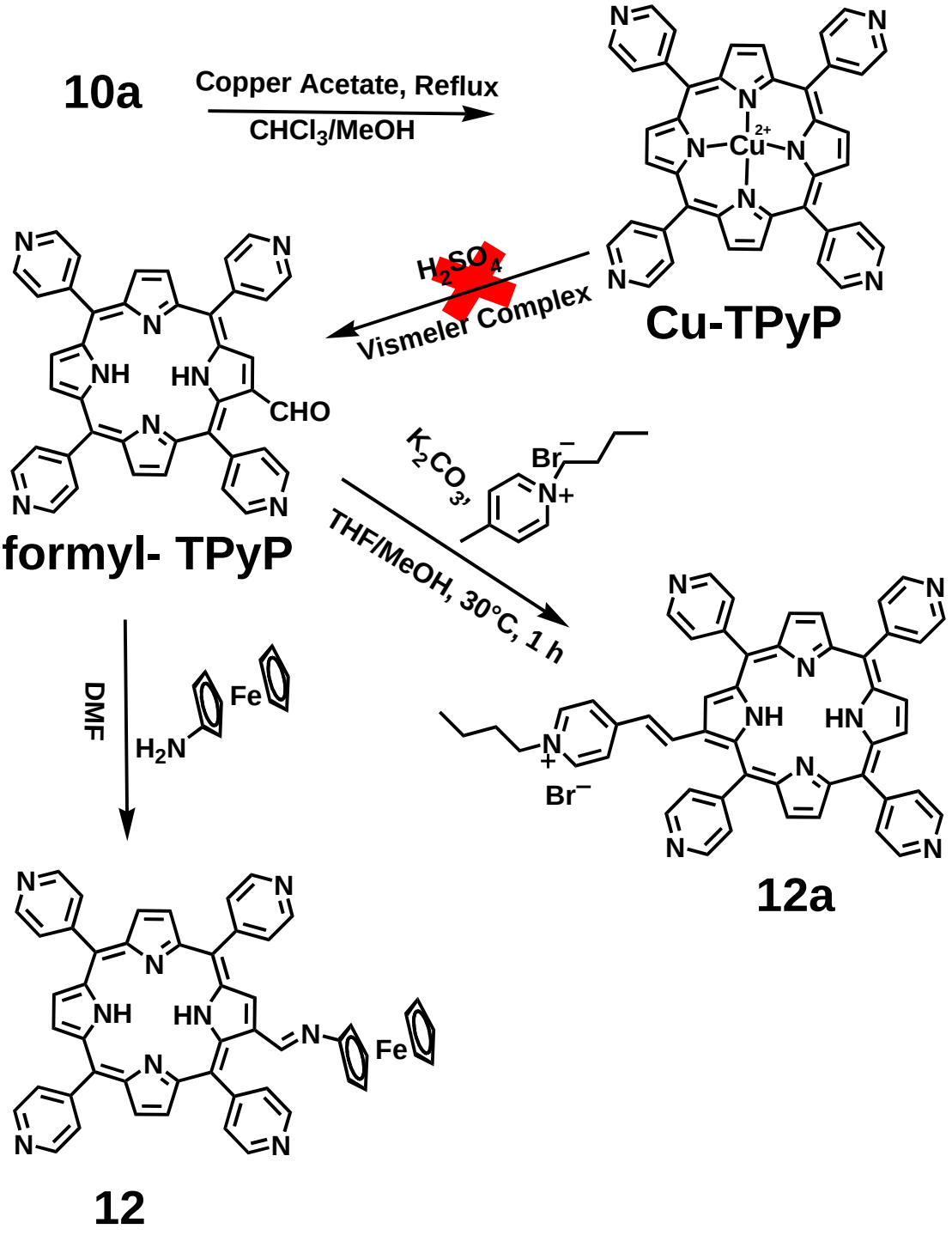

Scheme 2.14 Synthesis of β-substituted tetrapyridylporphyrin.[146]

2.9.2 Synthesis of mitochondria targeting β-substituted TPP'

The synthetic procedures for producing **formyl-TPP'**, β-substituted **TPP,** and the precursor were the same as those used in developing **formyl-TPP'**, **11a** and precursor

PYB. For the precursor, **TPP** was reacted with 4-methylpyridine just like in **Scheme 2.10** to obtain **PyBP**. **PyBP** was reacted with **formyl-TPP'** in the same manner as in **Scheme 2.12** to yield **13** (**Scheme 2.15**), and mass spectrometry was used to characterise the molecule. However, we could not detect the mass of **13**, nor were we able to obtain a satisfactory ^{1}H NMR spectrum.

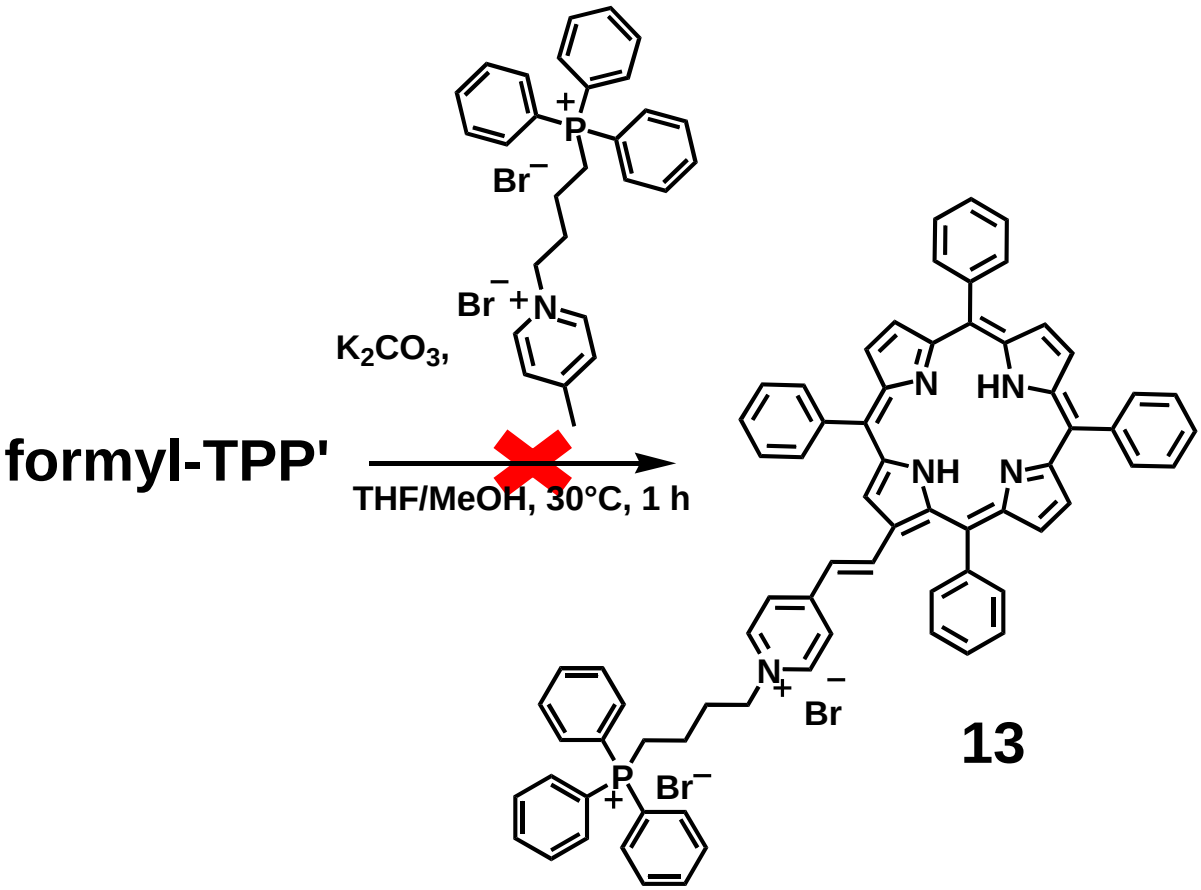

Scheme 2.15 Schematic synthesis of porphyrin **13**.[145]

2.9.3 Synthesis of ABAB porphyrins

The synthesis of ABAB type porphyrins with oppositely-arranged *meso*-aryl groups was carried out according to previously reported methods.[186] Firstly, a dipyrromethane (DPM) is synthesised from a reaction of pyrrole with an aldehyde in aqueous solution

at low pH. Secondly, the DPM is reacted with another aldehyde to afford an ABAB type porphyrin.

2.9.3.1 Synthesis of dipyrromethanes

1 eq of aldehyde and 3 eq of pyrrole were added to 100 ml aqueous HCl of 0.18 M (1.5:98.5, HCl/water (v/v)), followed by stirring of the reaction mixture at room temperature. The progression of the reaction was monitored using TLC. When there was formation of solids that stuck to the walls of the flask, a stirrer bar was used. Once the aldehyde could not be detected, stirring was stopped, and the solid was washed with water and filtered to obtain pure DPMs **a**, **b** and **c** (**Scheme 2.16**).

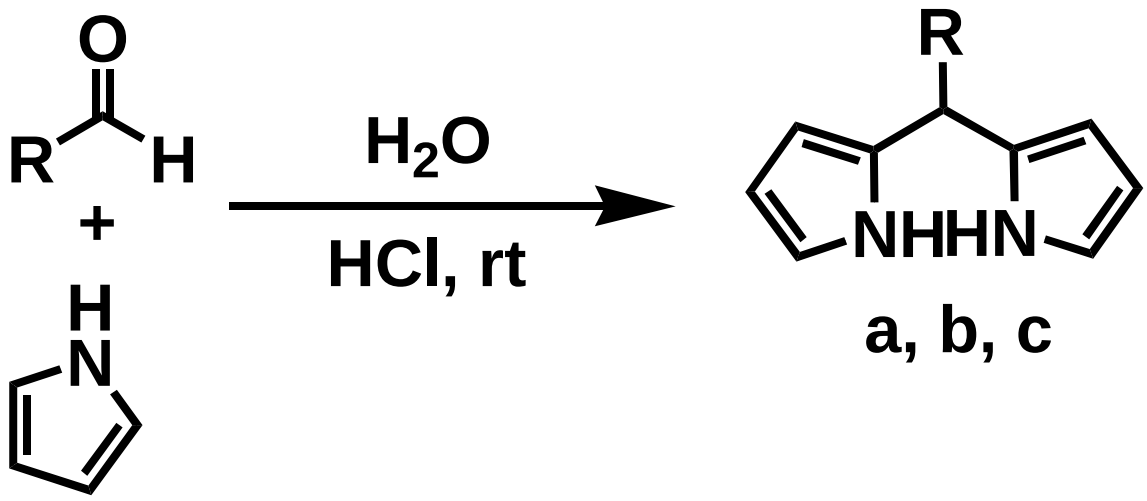

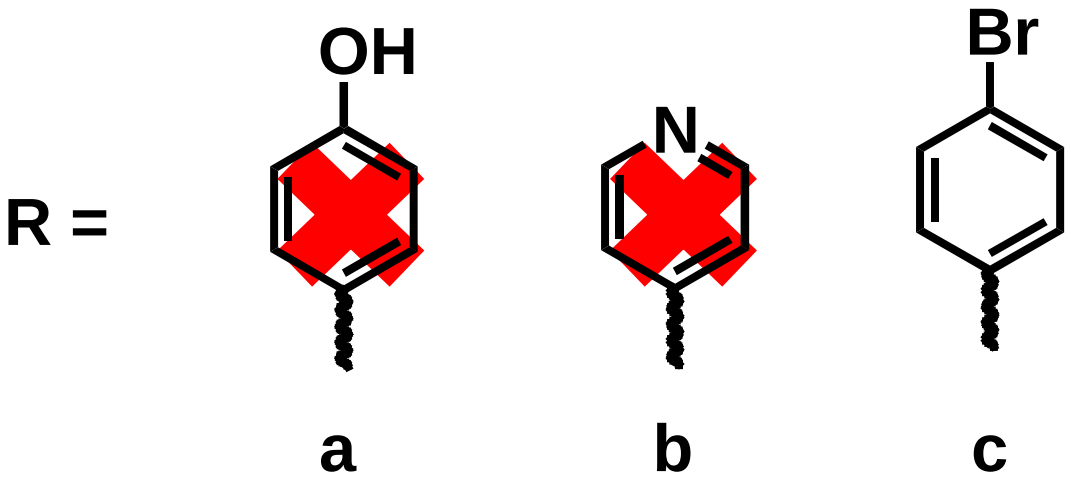

Scheme 2.16 Synthesis of dipyrromethane. The red cross indicates the unsuccessful formation of the DPM of interest.[186]

2.9.3.2 Synthesis of 5,15-bis(bromophenyl)-10,20-bis(pyridyl)porphyrin

1 eq of 4-pyridinecarboxaldehyde and 2 eq of **c** (DPM) were dissolved in DCM. This solution was stirred for 15 min at room temperature in the dark, and then 1 eq of 10% $BF_3{\cdot}OEt_2$ was added. After further stirring for 1 h, the reaction was quenched with aqueous sodium hydroxide, washed with water, and the product was extracted using DCM and dried over anhydrous sodium sulfate. When the product had dried, it was dissolved in acetonitrile, and 3.3 eq of NH_4Cl with 1 eq of DDQ were added before stirring the reaction for 1 h. The solvent was dried after the stated reaction time, and porphyrin **14** was isolated by silica gel column chromatography. We characterised the product by mass spectrometry. The mass obtained was m/z = 778.14 amu while the calculated was 774.50 amu. The difference of 4 amu between the actual and calculated mass was not convincing evidence that we obtained the porphyrin of interest, **Scheme 2.17**.

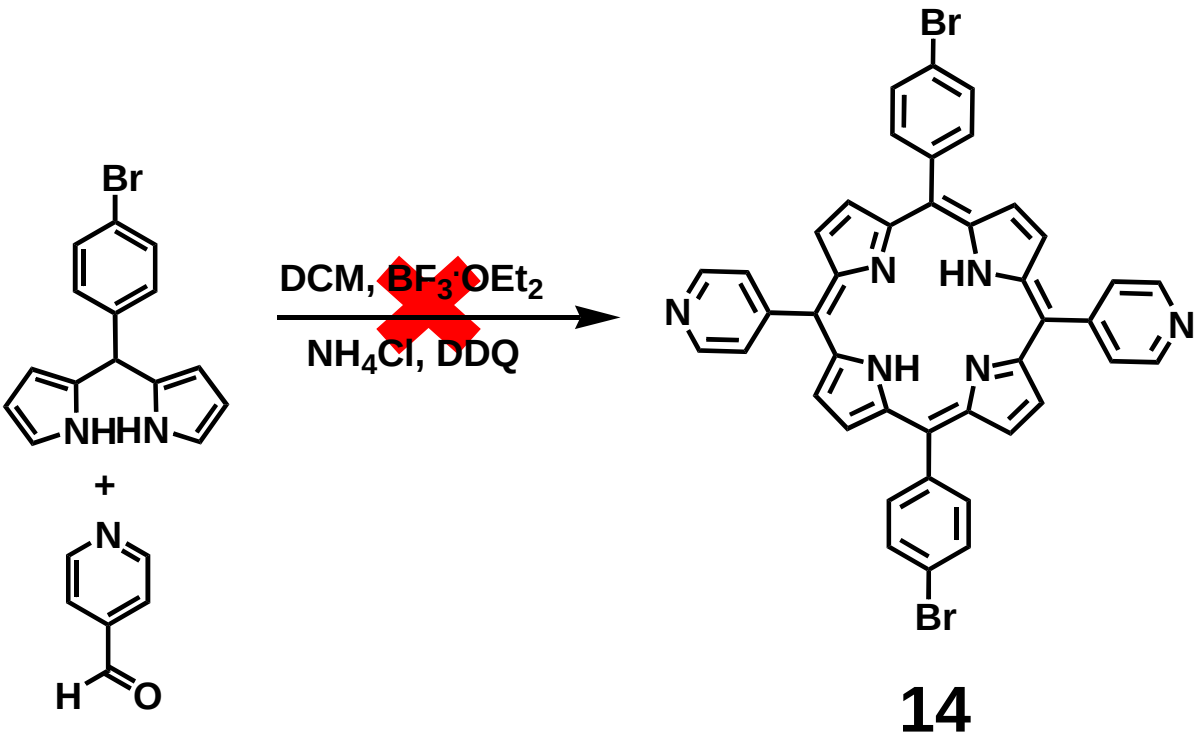

Scheme 2.17 Synthesis of 5,15-*bis*(bromophenyl)-10,20-*bis*(pyridyl)porphyrin (**14**).[186]

2.9.4 The rationale of the synthesis

Synthesis of asymmetric porphyrins was attempted with the aim of metalating the product with a Sn(IV) ion and adding axial ligands. Metalated porphyrins **12**, **12a,** and **14** would then be quaternized with bromobutane to afford cationic porphyrins that are mitochondria targeting. Additionally, the photophysicochemical properties of target porphyrins were to be compared with successfully synthesized porphyrins (**12**, **12a**, and **13** compared to **11**, while **14** would have been compared to **10**. The reactions used in these procedures are well known; nonetheless, unknown reasons caused the reactions not to be successful.

2.9.5 Synthesis of brominated tetraayrlchlorins

The exact procedure outlined in **Scheme 2.18** was followed in the synthesis of **TPP'** porphyrin. To synthesize a chlorin, the following steps were carried out; 1 eq of the porphyrin, 10 eq K_2CO_3 and 4 eq *p*-toluenesulfonylhydrazine were dissolved in 50 ml of dry pyridine. This reaction was refluxed for 12 h, and every 4 h, the exact stated amount of *p*-toluenesulfonylhydrazine was added. The reaction was halted when a band appeared at 730 nm, implying the reduction of two double bonds forming a bacteriochlorin. This reaction mixture was washed with water, extracted with chloroform, and trace amounts of *p*-chloranil were added while stirring at room temperature until the 730 nm band disappeared. The solvent was later removed using a rotary evaporator, and the residue was loaded on silica gel column chromatography using chloroform as the eluent to give a tetraphenyl chlorin.

Subsequently, 1 eq of the chlorin and 2 eq of NBS were dissolved in chloroform and stirred at room temperature. UV-visible absorption spectroscopy was used to monitor the formation of the brominated chlorin, while TLC was used to monitor the consumption of the chlorin. After the chlorin had been converted to the desired product, the reaction was washed with water, extracted with chloroform, and the solvent was evaporated. The crude product was loaded on a silica gel column to yield a brominated chlorin (**15**), but this turned out not to be the case; the chlorin was instead oxidised back to a brominated porphyrin (**16**) (**Figure 2.18**).

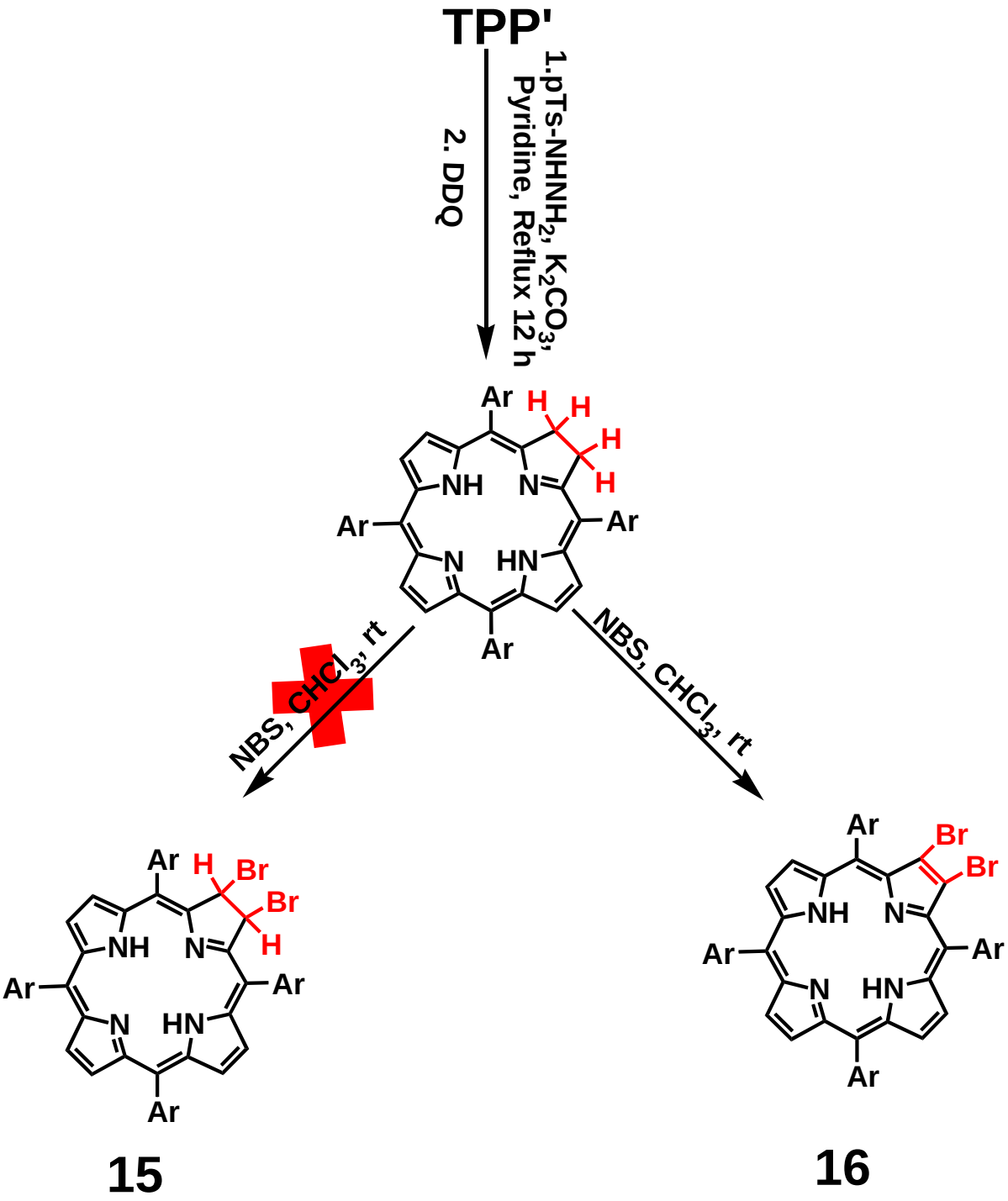

Scheme 2.18 General synthesis of brominated chlorin **15**.

2.9.4.1 Synthesis rationale

The synthesis of brominated chlorin was attempted to enhance the singlet oxygen generation compared to the previously reported tetraphenylchlorin.[176] The aim was to

metalate the molecule with Sn(IV), add axial ligands, and compare the physicochemical properties to those of the non-brominated tetraphenylchlorin reported previously.[176] Bromination of chlorins has been reported previously, but the reaction procedure failed for unknown reasons.

3.0 Concluding remarks

Novel BODIPY dyes and porphyrins were successfully synthesized using different synthetic routes. Mass spectrometry and ^{1}H NMR spectroscopy were used to characterise the target molecules and confirm their successful synthesis. *In silico* studies were conducted on the lengau cluster at the Centre for High Performance Computing in Cape Town. Additionally, the departmental cluster at the Department of Chemistry at Rhodes University was used for ligand docking studies with Autodock tools.

Results and Discussion

The section is divided into three chapters

Chapter 3: Synthesis, characterisation, photophysicochemical parameters and TD-DFT calculations.

Chapter 4: Lipophilicity, photostability and Molecular docking.

Chapter 5: Anticancer and antibacterial photodynamic activities

Chapter 6: Molecular modelling

Chapter 3

Detailed Synthesis, Characterisation, and Physicochemical Parameters of BODIPY Dyes and Porphyrins.

3. Synthesis, characterisation, and physicochemical parameters of BODIPY dyes and porphyrins

3.1 Synthesis

3.1.1 Synthesis of BODIPY core dyes

The BODIPY core dyes were synthesised *via* an acid-catalyzed one-pot three-step reaction using 2,4-dimethylpyrrole and aldehydes of interest in dry DCM. This reaction was conducted under an inert atmosphere. TFA was used as a Lewis acid catalyst to protonate the carboxyl oxygen, resulting in a partial positive charge, making the carbonyl vulnerable and prone to nucleophilic attack by pyrrole. This led to the formation of an unstable dipyrromethane, which was immediately oxidised to more stable dipyrromethene structures by using *p*-chloranil as an oxidant. After the formation of the dipyrromethene, TEA, which acts as a Lewis base, was added to deprotonate the nitrogens on the dipyrromethene. The complexation with BF_2 is achieved through the addition of $BF_3{\cdot}OEt_2$. This led to the synthesis of core dyes **1** and **2** (**Scheme 2.2**). The core dyes were further modified by electrophilic substitution of the protons at the 2,6-positions with either bromine, NBS, or NIS. This reaction resulted in the formation of halogenated core dyes **3**, **4,** and **5** (**Scheme 2.3**).

3.1.2 Synthesis of π-extended BODIPY dyes

The π-system of the dyes was extended using the Knoevenagel condensation reaction, where piperidine acts as a base and removes a proton from the methyl groups at the 3,5-positions. This leads to an addition reaction at the protonated carbonyl from acetic acid. Next, a second proton from the methyl groups is removed to form a double bond, and, in this process, the protonated oxygen is released in the form of water. The water is removed from the reaction using a Dean-Stark apparatus because it halts the reaction. This reaction mechanism is not specific; thus, it depends

on the reaction time to get mono, di, tri, or tetra π-extended dyes. In this work, this approach afforded both di- and mono-substituted for the BODIPY **6**-**9** series (**Scheme 2.3**).

3.1.3 Synthesis of porphyrins

Adler and Longo's synthetic method was followed for the synthesis of free-base porphyrins **10a** and **TPP'** (**Scheme 2.5** and **2.11**). Copper acetate was used to metalate **TPP'** to form **Cu**-**TPP'**, which enabled the synthesis of **formyl-TPP'**. This facilitated conjugation at pyrrolic positions to form the π-extended β-substituted porphyrin **11** series. A previously reported procedure[134] was used to insert a heavy Sn(IV) central metal ion. This also led to the incorporation of hydroxyl axial ligands, which were then further modified (**Scheme 2.13**).

3.2 Characterisation

^{1}H NMR spectroscopy and MALDI-TOF MS were used to confirm the successful syntheses of all the dyes.

3.2.1 Structural analysis of core dyes 1 and 2

Signals for all 21 protons of **1** were readily assigned in the ^{1}H NMR spectrum (**Figure 3.1**). The multiplets between 7.12−7.28 ppm integrate to 4 aromatic protons from the phenyl ring on the *meso*-position, while the singlet signal at 5.92 integrates to 2 protons at the 2,6-positions of the BODIPY core. The remaining singlet signals around 1.37−2.49 ppm were attributed to the methyl groups at the 3,5- and 1,7-positions. In contrast with a previous literature report of this dye, no ^{1}H NMR spectrum could be recorded for **2**, which contains a *meso*-ferrocenyl moiety.[158]

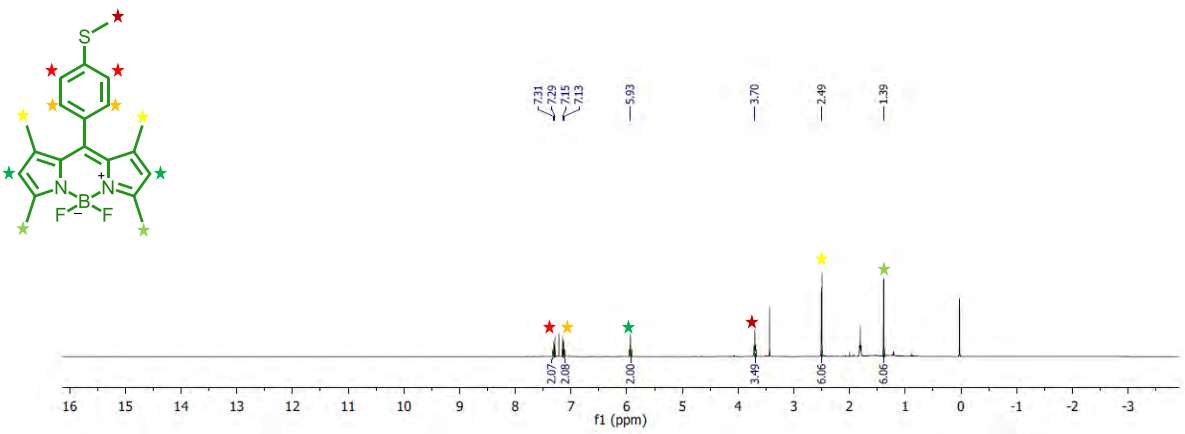

Figure 3.1 ^{1}H NMR spectrum of BODIPY core dye **1** in $CDCl_3$. The colour code of the stars shows the position and chemical shift of each proton on the dye. Peaks marked with an asterisk were identified as solvent impurities.

3.2.2 Structural analysis of halogenated core dyes 3-5

The phenyl *meso*-group protons of **3** and **4** lie in the 7.12−7.36 ppm region of the ^{1}H NMR spectrum for both compounds. The disappearance of the peak at 5.93 ppm found in **Figure 3.1** confirmed the successful synthesis of the halogenated core dyes **3** and **4** in **Figure 3.2**. The peaks for the methyl groups in all the molecules lie between 2.61−1.23 ppm. MALDI-TOF MS was used to further confirm the successful synthesis of the compounds. The calculated masses of 528.06 and 622.07 amu were in close agreement with the parent peaks observed at 528.45 and 622.79 m/z for **3** and **4**, respectively (**Figure 3.3**). In a similar manner to **2**, no ^{1}H NMR spectrum could be recorded for **5**, so the characterisation of this dye depends solely on MALDI-TOF MS and UV-visible absorption spectroscopy. For reasons that will be described in greater depth in section 3.4 and Chapter 4, **5** was found to be unsuitable for use in PDT and PACT applications, so no further efforts were made to characterise BODIPYs **2** and **5**.

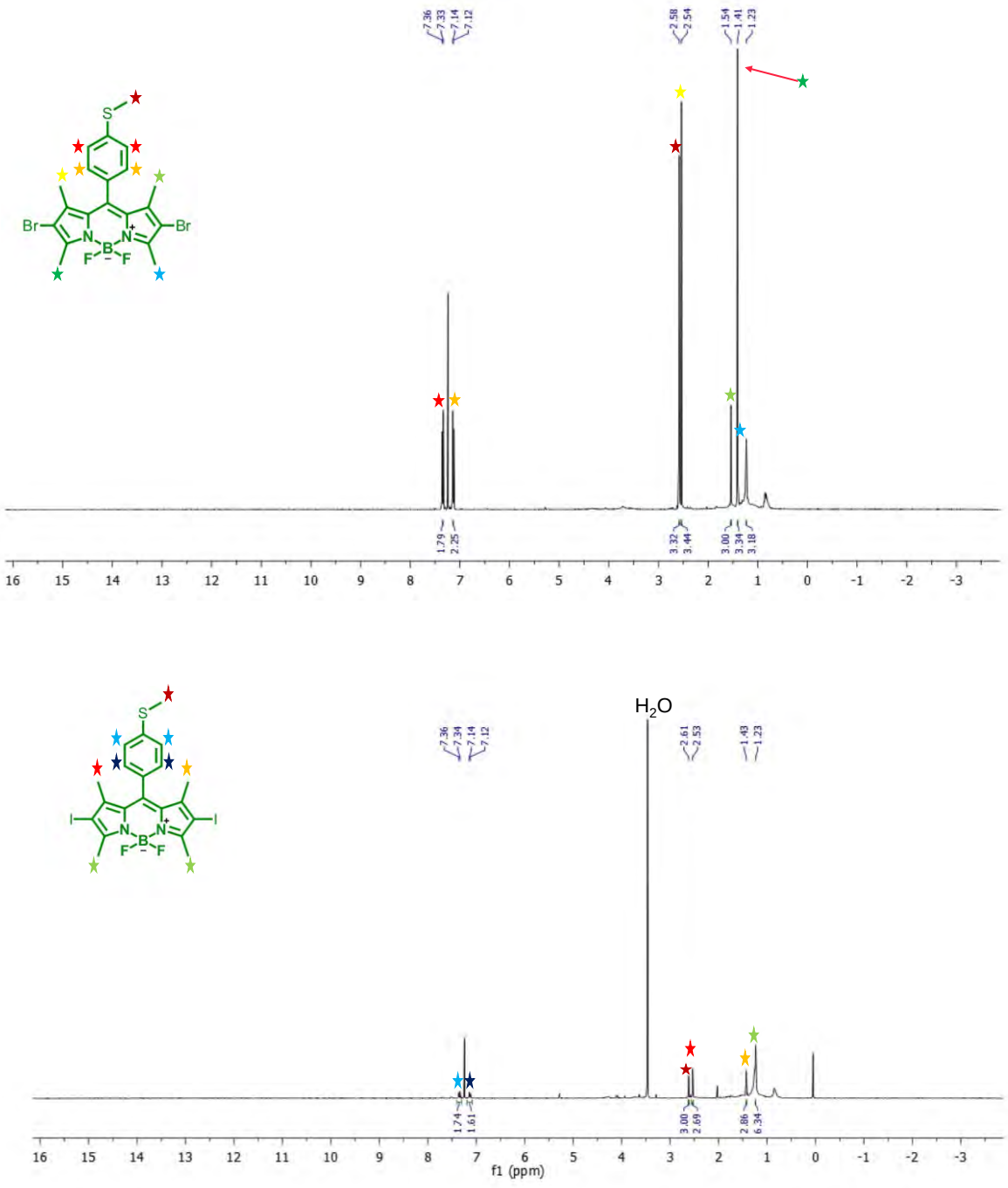

Figure 3.2 ^{1}H NMR spectra of **3** and **4** in $CDCl_3$.

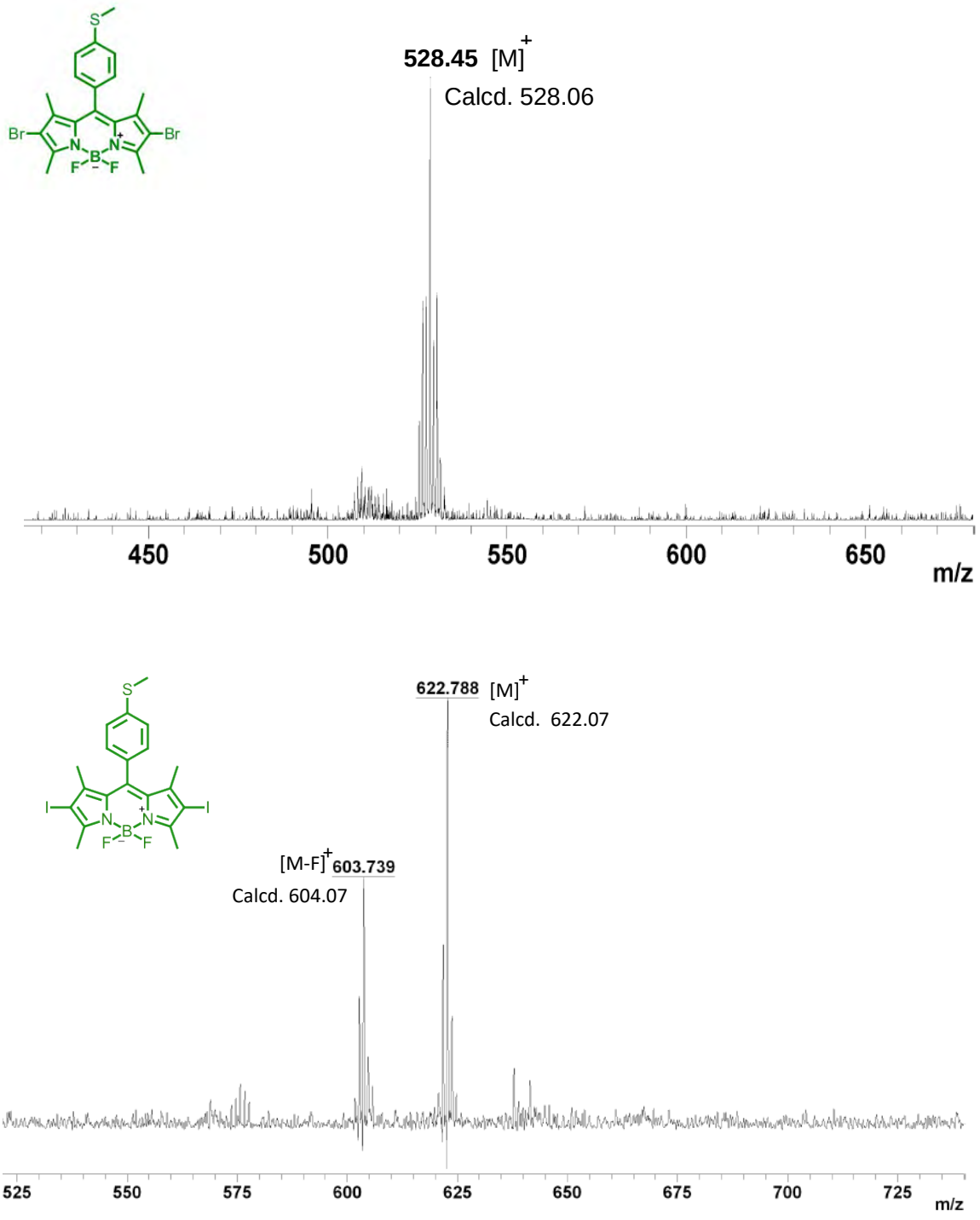

Figure 3.3 MALDI-TOF MS spectra of core dyes **3** and **4**.

3.2.3 Structural analysis of π-extended BODIPY dyes

In the ^{1}H NMR spectrum of BODIPY dye **6a**, additional proton peaks were observed in **Figure 3.4**, due to the styrylation of **3**. **Figure 3.4** displays a colour code proton

assignment corresponding to **6a**. The two protons at 8.61 ppm can be assigned to the first set of protons with yellow stars on the *meso*-phenyl group, and protons at 8.59 ppm can be assigned to the other set of protons in the same group. The protons marked with red stars from 8.86-7.19 ppm were assigned to the phenyl ring and vinylene protons of the styryl moieties. The protons in the 2.57−1.52 ppm region can be readily assigned to the methyl groups. MALDI-TOF MS was employed further to confirm the synthesis of **6a**. The calculated mass of **6a** was 706.25 amu. This mass is consistent with the parent peak at 708.04 for **6a** in **Figure 3.5**, if an $[M + H]^+$ species is assumed. The peaks in the ^1H NMR spectra and the MS data for the other π-extended BODIPY dyes can be readily rationalised in a similar manner.

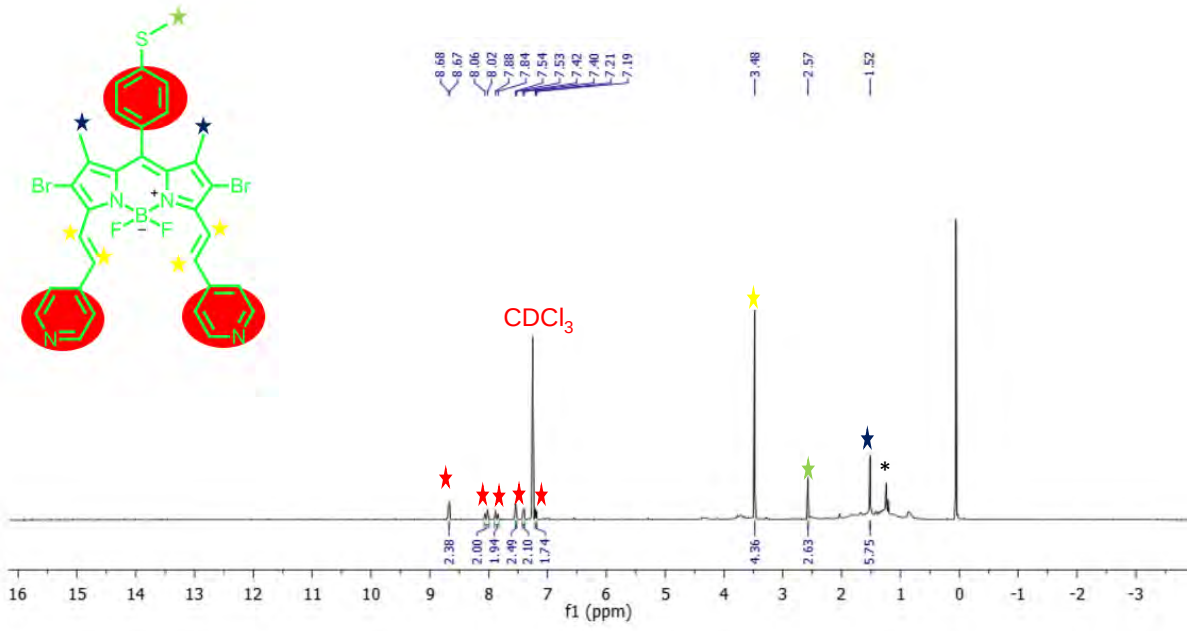

Figure 3.4 ^1H NMR spectrum of **6a** in $CDCl_3$.

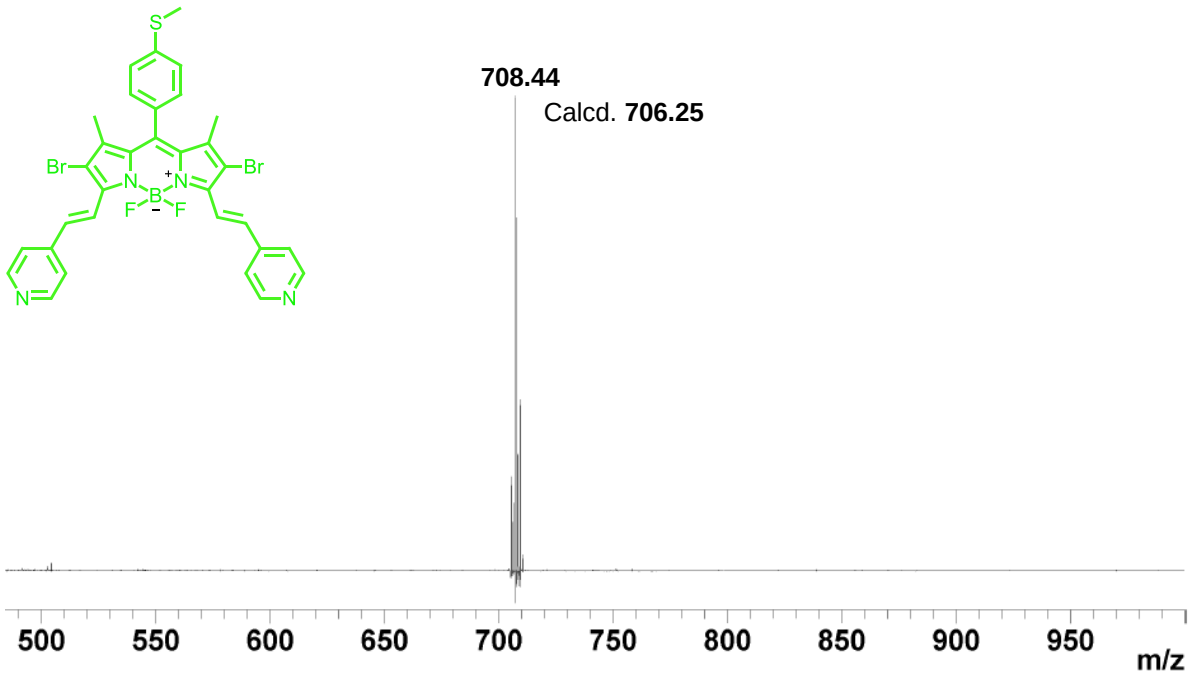

Figure 3.5 MALDI-TOF MS spectrum of **6a**.

3.2.4 Structural analysis for porphyrins

The porphyrin **10** series were characterised in a similar manner to the similar mitochondria targeting Sn(IV) porphyrin complex reported previously by Balaji et al.[133] For **10d**, a series of multiplets appeared between 3.75−1.21 ppm were attributed to the hydrocarbon chain of the linker, while additional sets of peaks in the 7.79−7.74 ppm, arise from the aromatic protons (**Figure 3.6)**. The remaining ^{1}H NMR spectra of the porphyrin **10** series were assigned in a similar manner. A similar rationale was used in characterising the ^{1}H NMR spectra of **11a**, **11b**, and **11c**. The ^{1}H NMR spectrum of **11c** is provided as an example in **Figure 3.7**. Identifying inner pyrrole NH peaks of free base compounds was problematic possibly due to exchange with the deuterated solvent.

The MALDI-TOF MS technique that was applied to the other dyes was also attempted to further elucidate the structure of these molecules, but, in contrast with **10a** and **10b**, **10c-e** did not ionise when a wide range of different matrices or no matrix were used. Thus, mass spectrometry data cannot currently be reported for these complexes due to time constraints. Attempts are currently underway to use a high-resolution ESI-MS instrument to rectify this. Other MS techniques will be attempted in future with the assistance of overseas collaborators should this also prove unsuccessful.

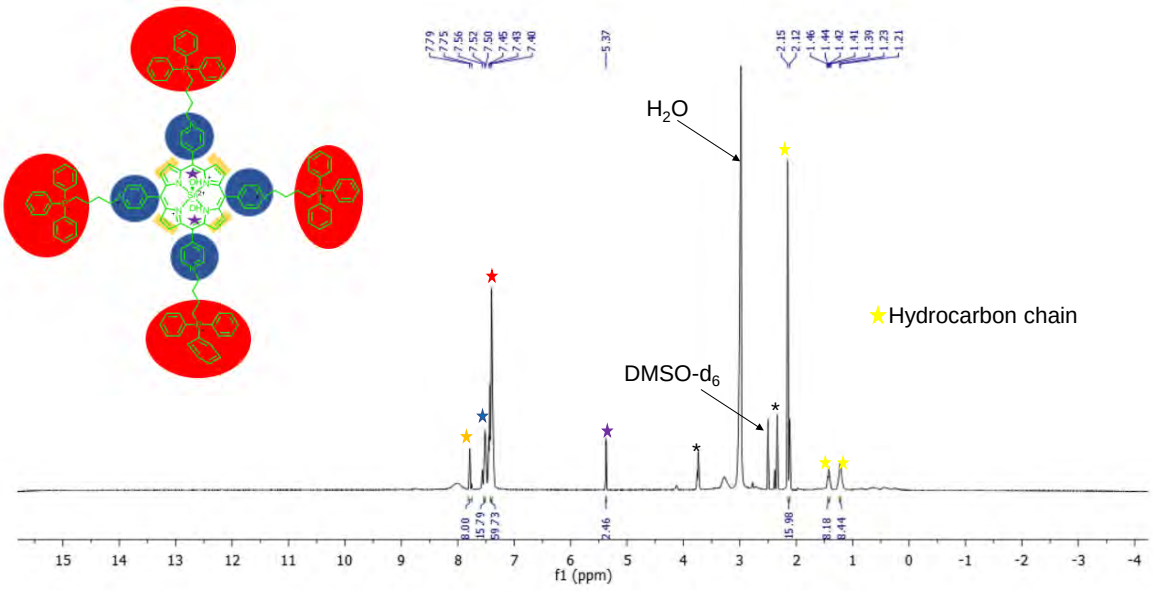

Figure 3.6 ^{1}H NMR spectrum for **10d** in DMSO-d_6.

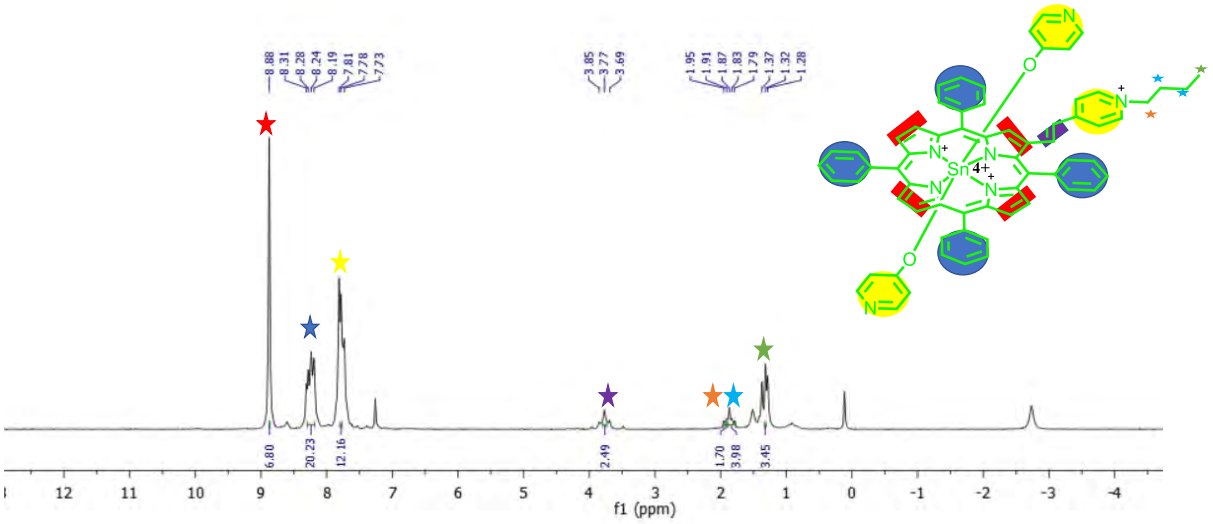

Figure 3.7 ^{1}H NMR spectrum for **11c** in $CDCl_3$.

3.3 Optical spectroscopy and TD-DFT calculations

3.3.1 BODIPY dyes

The BODIPY core dyes exhibit typical UV-visible absorption spectra for dyes of this type.[84] A major spectral band is observed at *ca.* 500 nm due to $S_0 \rightarrow S_1$ transitions, and a weaker vibrational shoulder band is observed at *ca.* 420 nm. The ground state absorption spectra of **1**-**5** are shown in **Figure 3.8**. A significant red shift of the main BODIPY spectral band is observed in the two sets of halogenated core dyes for reasons that will be described in greater depth based on an analysis of TD-DFT calculations in Chapter six. The *meso*-ferrocenyl moiety of **2** and **5** results in a bathochromic shift of the main spectral band relative to the spectra of **1** and **3**. Substitution with styryl groups at the 3,5-positions to form BODIPYs **6-9** results in a very large red shift of the main BODIPY spectral band so that it lies in the therapeutic window (**Figure 3.9**). The reasons for this will also be described in greater depth in the context of the analysis of the TD-DFT calculations in Chapter six.

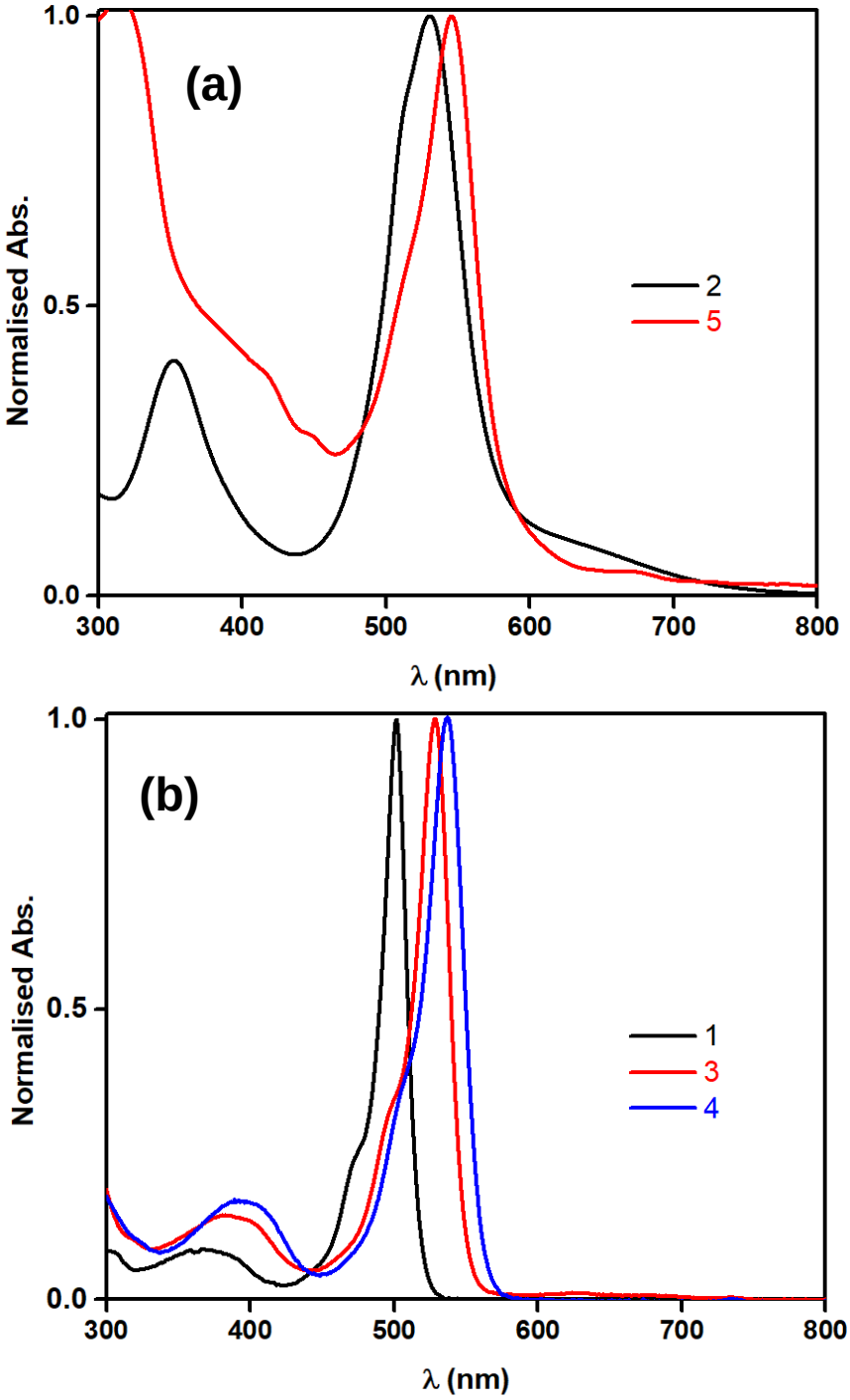

Figure 3.8 Normalised UV-vis absorption spectra of BODIPY core dyes (a) **2** and **5**, (b) **3**, **4** and **5** in DMSO.

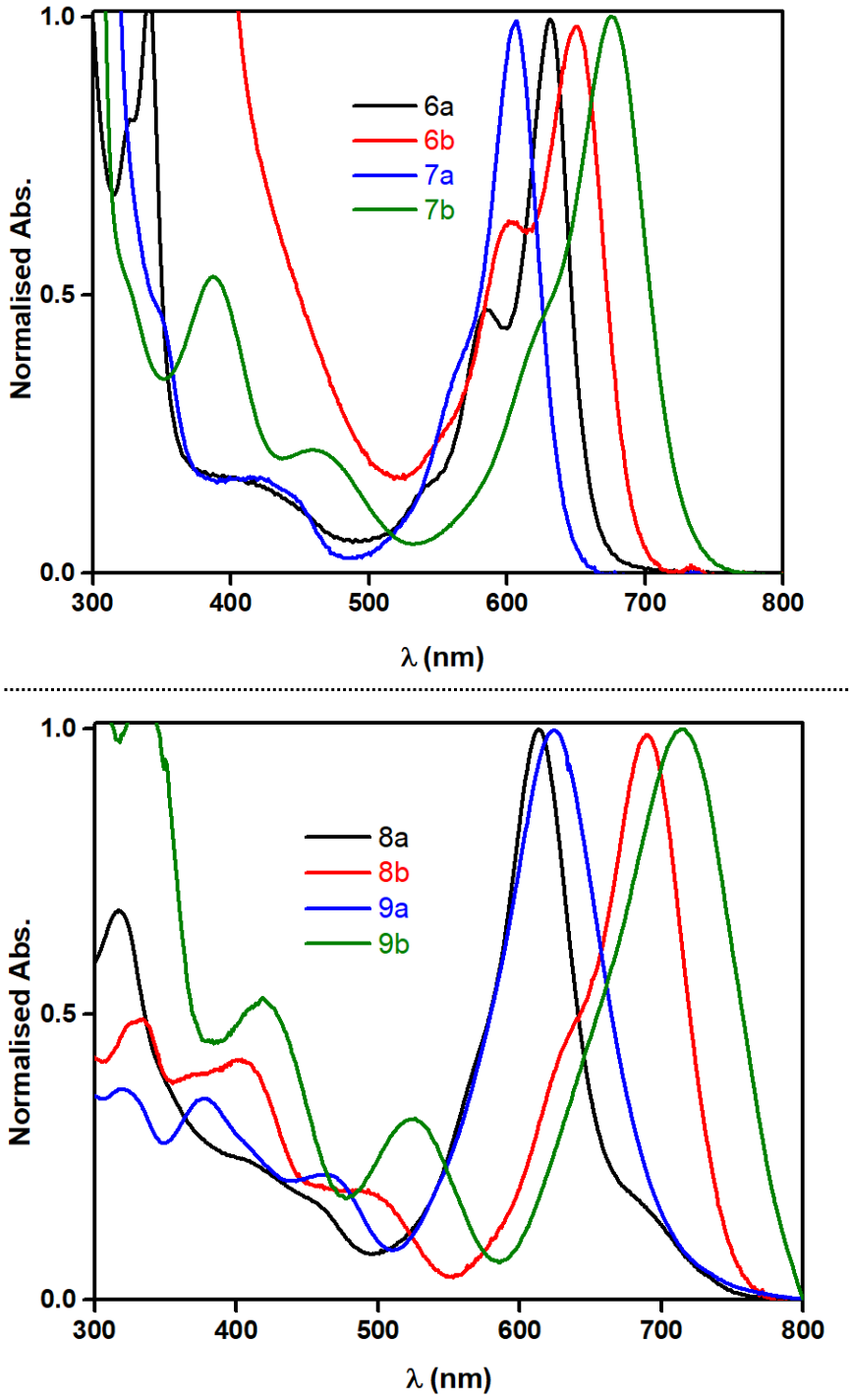

Figure 3.9 Normalised UV-visible absorption spectra in DMSO of BODIPY dyes **6**-**9** with an extended π−conjugation system.

3.3.2 Porphyrins

UV-visible absorption spectra were measured in DMSO for all the PS dyes at ambient temperature (**Figure 3.10**). The spectrum for **10c** had a broad B band at 427 nm and less intense Q bands. This band broadening may be related in part to aggregation effects. Upon metalation and introduction of the axial ligands, there was a narrowing of the absorbance band. This same trend was also observed in the spectra of **11a**, **11b,** and **11c**.

The TD-DFT calculations in Chapter six demonstrate that the introduction of the cationic triphenylphosphonium moieties at the *para* positions of the *meso*-aryl rings of the porphyrin **10** series had a minor effect on the electronic structure where the frontier π-MOs of the porphyrin ligand are concerned. Only a minimal bathochromic shift was observed (**Figure 3.10**). This can be ascribed to a stabilising inductive effect that affected the four frontier π-MOs of the porphyrin ligand to the same extent. There is a slight blue shifting of the B band of **10e**, which may be related to the electron-donating effect of the axial ligands.

The absorption spectrum for **11a** has an unusual band morphology. This can be ascribed to the disruption of the symmetry by the extended conjugation that occurs at the β-position or may be related in part to aggregation, which is typical of free-base porphyrins. This topic will be explored further in Chapter six. A typical metal porphyrin spectrum is observed when a central metal ion is incorporated.

Figure 3.11 provides the MCD spectra of the Sn(IV) complexes **10d** and **11b**. The magnetic circular dichroism (MCD) spectra of **10d** and **11b** contain the derivate-shaped A_1 or pseudo-A_1 terms corresponding to the B and Q bands.[187] The spectrum of **10d** is broadly similar to those of zinc tetraarylporphyrins,[121] which exhibit a sequence of two positive Faraday A_1 terms aligned with the Q band (Q_{00}) and a higher

energy vibronic band (Q_{01}). The Q_{00} and Q_{01} bands of D_{4h} symmetry metal porphyrins are *x/y*-polarised. An observed negative to positive sign sequence with ascending emerging in **Figure 3.16** is predicted by Michl's perimeter model in the MCD spectrum when there is a greater splitting of the MOs derived from the HOMO of the parent than those derived from the LUMO.[121,187,188] The negative 607 and positive 597 nm MCD bands of **10d** correspond to the 604 nm absorption peak, while negative 567 and positive 560 nm MCD bands correspond to the 563 nm absorption peak. However, the MCD spectrum of **11b** was different because it was dominated by a single negative pseudo-*A* term in the Q band region. The reasons for this are explored in Chapter 6 and may be related to the presence of an MO localised on the substituent introduced at the β-position.

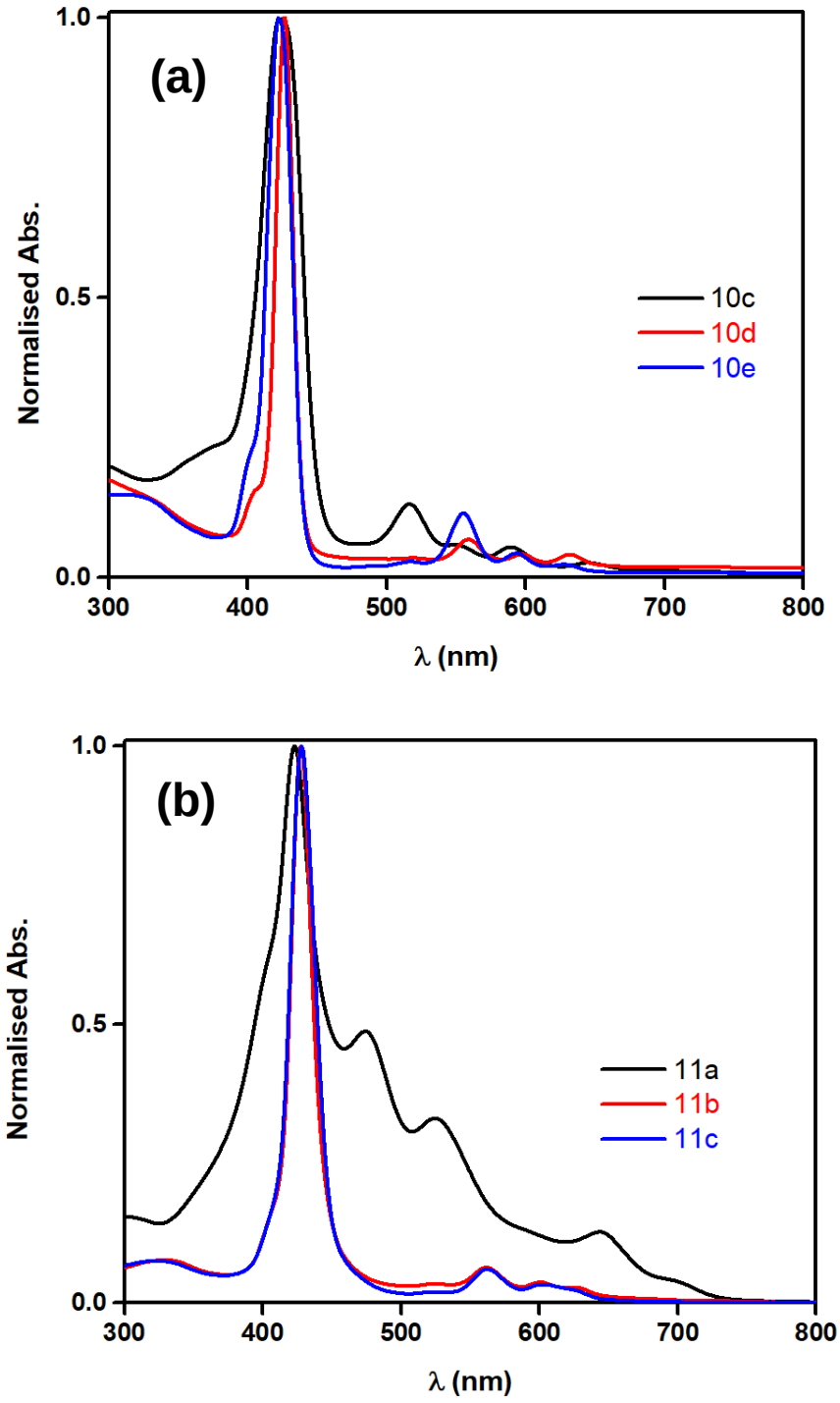

Figure 3.10 Ground state UV-visible absorption spectra of **11c**, **11d,** and **11e** in DMSO.

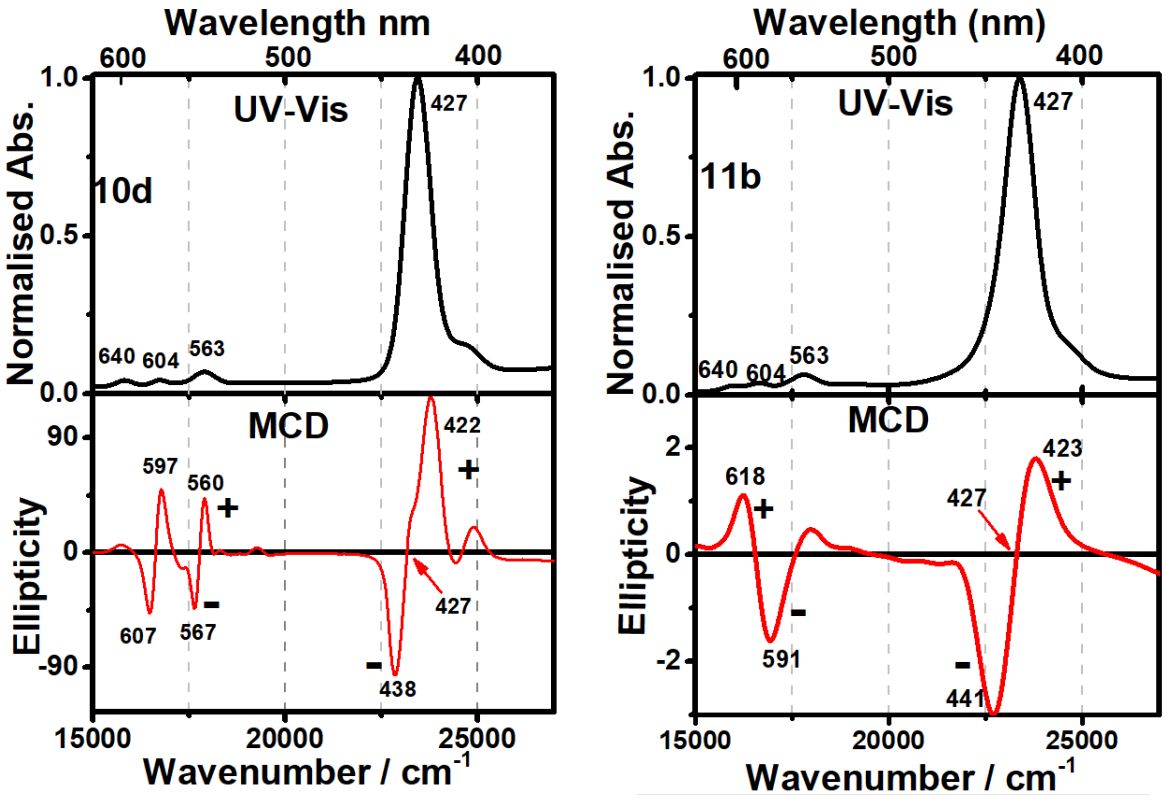

Figure 3.11 The UV-visible absorption and MCD spectra of the metal porphyrin complexes in DMSO.

3.4 Photophysicochemical parameters

All the physicochemical properties reported in **Table 3.1** were measured in DMSO.

Table 3.1 Photophysical properties of all synthesised PS dyes in DMSO

PS	λ_{abs} (log ε)	Φ_F	Φ_Δ	τ_T (μs)
1	500 (5.21)	0.61[a]	0.08[a]	ND[b]
2	541 (5.12)	0.009	-	-
3	530 (5.75)	<0.01	0.49	40
4	541 (5.61)	<0.01	0.78	122.8
5	555 (5.10)	<0.01	-	-
6a	630 (5.42)	<0.01	0.17	16
6b	651 (5.28)	<0.01	-	< 1
7a	668 (5.59)	<0.01	0.49	6.8
7b	600 (5.73)	<0.01	0.55	9.6
8a	693 (5.56)	<0.01	0.16	< 1
8b	619 (5.32)	<0.01	0.05	< 1
9a	714 (5.02)	<0.01	0.16	< 1
9b	616 (5.78)	<0.01	0.12	< 1
10c	427 (5.60), 521 (4.62), 558 (4.76), 596 (4.32), 657 (4.01)	<0.01	0.53	284
10d	427 (5.62), 563 (5.03), 604 (4.03), 640 (4.32)	<0.01	0.78	94
10e	424 (4.96), 561 (5.21), 603 (4.53), 634 (4.56)	<0.01	0.49	69
11a	422 (4.82), 538 (4.63), 651 (5.20)	<0.01	0.09	135
11b	427 (4.51), 563 (4.56), 604 (4.53), 640 (4.36)	<0.01	0.42	112
11c	429 (4.51), 569 (4.62), 619 (4.36)	<0.01	0.55	129

[a]Values taken from the MSc thesis of Jessica Harris, "BODIPY dyes for singlet oxygen and optical limiting applications", at Rhodes University in 2017. [b]Not determined.

3.4.1 Singlet oxygen quantum yields (Φ_Δ)

The ability of the PS to generate singlet oxygen is one of the most critical factors determining their utility for PDT and PACT applications. This property determines how effective the PS is because it is responsible for cell death through oxidative stress. Singlet oxygen studies were conducted in DMSO using DPBF and DMA as singlet

oxygen scavengers for BODIPY dyes and porphyrins, respectively. A comparative method **Equation 1.1**. MB (Φ_Δ= 0.52) was used as a standard for BODIPY dyes, while ZnTPP (Φ_Δ= 0.55) was used for porphyrins (**Table 3.1**). The degradation of the singlet oxygen scavenger band was observed at specific time intervals, delineated by **Figure 3.17** using porphyrins **10d**, **11c,** and BODIPY **7a** as examples. As expected, the halogenated BODIPY core dyes exhibited high singlet oxygen quantum yields due to the enhancement of ISC related to the heavy atom effect. Upon π-extension, there was a decrease in Φ_Δ value, possibly due to an increase in intramolecular electron transfer.[189] Mono-substituted BODIPY dyes have higher Φ_Δ values than di-substituted dyes, possibly because there is less scope for conformational flexibility. The BODIPY **8** and **9** series recorded the lowest Φ_Δ values. This may be due to greater conformational flexibility and/or intramolecular charge transfer properties.

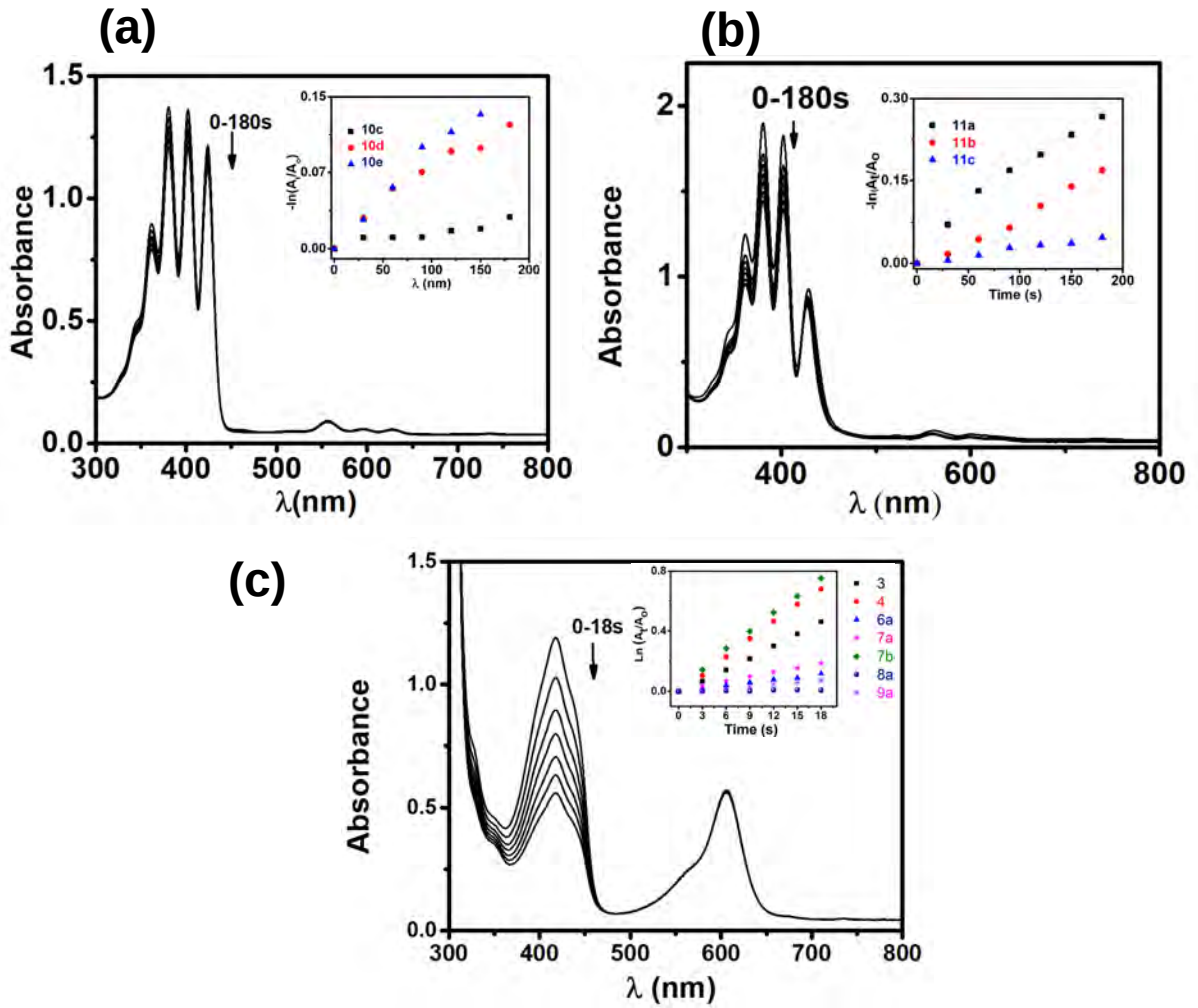

Figure 3.12 The change in absorbance of singlet oxygen scavengers (a) and (b) DMA while (c) is DPBF upon photoexciting the **PS** (a) **10d**, (b) **11c,** and (c) **7a** at specific time intervals. The insets are plots of ∆A values for DMA at 417 nm *vs* photoirradiation time in the presence of (a) the porphyrin **10** series, (b) the porphyrin **11** series, and (c) the BODIPY dyes, excluding the dyes that exhibited minimal DPBF band degradation.

In the context of the porphyrins, the free bases exhibited lower Φ_Δ values (0.53 for **10c** and 0.09 for **11a**) than the metal complexes, as would normally be anticipated in the absence of a heavy central ion. The lower Φ_Δ value of **11a** might arise from the π-extension at the β-position and enhanced photoelectron transfer (PET) effects. Upon metalation, there is an increase in the singlet oxygen quantum yield associated with the heavy atom effect. However, when OH axial ligands at the metal centre were

replaced with 4-pyridyloxy ligands in the porphyrin **11** series, there was an increase in the Φ_{Δ} value (**Table 3.1**). This was not observed for the porphyrin **10** series, however.

3.4.2 Fluorescence quantum yields and triplet state lifetimes

All fluorescence quantum yield measurements for the synthesised dyes were conducted in DMSO using the comparative method. ZnTPP (Φ_F = 0.039[184] in DMSO), Rhodamine 6G (Φ_F = 0.95 in ethanol[190]), and ZnPc (Φ_F = 0.20 in DMSO[191]) were used as standards. **Equation 1.2** was used to calculate the Φ_F values tabulated in **Table 3.1**. As anticipated, the Φ_F values of halogenated BODIPY core dyes **3**, **4**, and **5** were less than those of **1** (Φ_F = 0.61) and **2** (**Table 3.1**). This quenching is attributed to the addition of heavy atoms that enhance the rate of ISC. All the styrylated BODIPY dyes exhibited minimal fluorescence, since the heavy atoms at the 2,6-positions enhance the rate of ISC.

Normally free base porphyrins exhibit high Φ_F values, but it was not the case in this study. This can be ascribed to either the substituent at the β-position (porphyrin **11** series) or the TPP moiety (porphyrin **10** series) that enhances the PET effect. It was not surprising that the metal porphyrin complexes displayed very small fluorescence quantum yields because the central Sn(IV) ion enhances the rate of ISC.

Figure 3.18 shows triplet state decay curves using compounds **10e** and **11c** as examples. The ability of the PS to populate the triplet state is one of the determining factors of how effective the molecule is in causing oxidative stress during the bioassays. T_T studies were conducted in DMSO purged with nitrogen to eliminate the oxygen which receives energy from the PS that populates the triplet state during PDT and PACT. All dyes have values on the microsecond timescale ().

In the context of the BODIPY dyes, **4** had the longest triplet lifetime because of the iodines at the 2,6-positions. This enhances spin-orbital coupling and enables the PS to readily populate the triplet state. Nonetheless, after extending the π-system, there was a decrease in the triplet lifetime of the molecules. This arises from the enhancement of intramolecular electron transfer caused by PET in the singlet manifold. Hence there is lower ISC associated with styrylated BODIPY dyes.

Porphyrin molecules displayed remarkable long-lived triplet lifetimes, with free bases having the longest. This may be due to there being less intermolecular electron transfer.

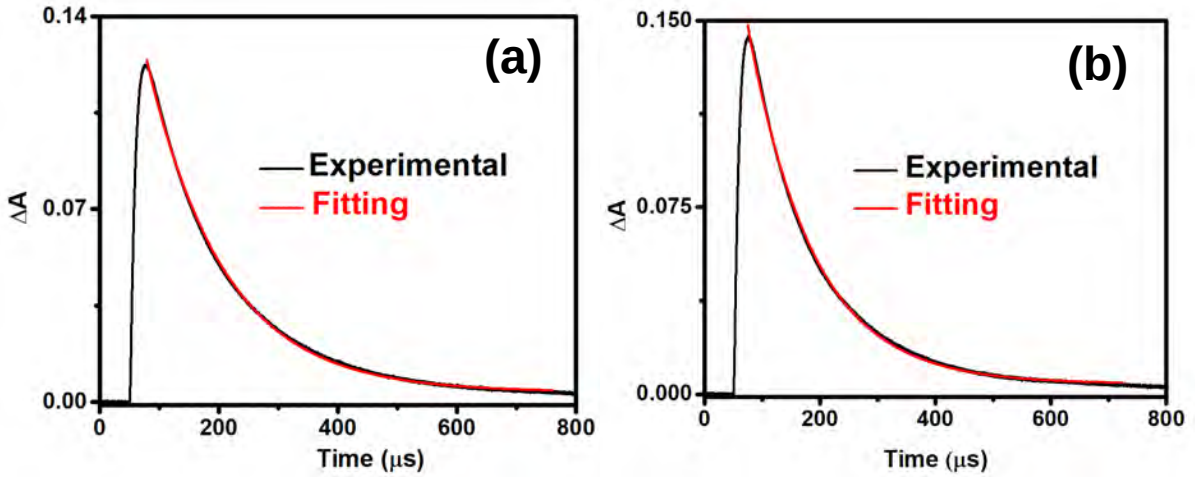

Figure 3.13 Triplet absorption decay curve of (a) **10e** and (b) **11d** in N_2 purged DMSO.

3.5 Concluding remarks

The synthesised dyes were characterised by mass spectrometry and ^{1}H NMR spectroscopy to confirm that the dyes were successfully synthesised. Additionally, photophysicochemical studies were conducted. The porphyrins exhibited superior properties to BODIPY dyes from the standpoint of PDT and PACT applications, since the porphyrins generated high singlet oxygen yields.

Chapter Four

Lipophilicity, Photostability, and Molecular docking.

4. Lipophilicity, cellular uptake, photostability and Molecular docking.

4.1 Lipophilicity, cellular uptake, and photostability

The lipophilicity of photosensitisers affects cellular uptake, which plays a vital role in maintaining the efficacy of the PS during PDT.[184] Generally, an increase in cellular uptake is accomplished by a PS with high lipophilicity/hydrophobicity, but dyes of this type usually aggregate in an intracellular aqueous environment, lowering ROS production. In contrast, PS dyes which are highly hydrophilic, tend to remain unaggregated, but their ability to cross the cell membrane is impaired. Hence, a PS with balanced lipophilic/hydrophilic properties is required to attain high cellular uptake and PDT efficacy.[192]

The lipophilicity (Log P) values of the BODIPY dyes and porphyrins were obtained using the shake-flask method.[193–195] The BODIPY dyes recorded smaller log P values than the porphyrins except for dye **6b**, which was cationic. This difference is credited to either the TPP^+ and the PyB^+ moieties that were conjugated to the porphyrins. According to Lipinski's Rule of 5, Log P values must fall between 1 and 5 for the molecule to achieve a balance between aqueous solubility and cell permeability.[196–198] All the dyes in this study displayed desirable Log P values except for **7a**, which has a value that lies slightly outside the range (**Table 4.1**).

The concentration dependence in the cellular uptake of the dyes was studied on MCF-7 and Hela cells for 24 h, and the absorbance of the internalised dye was measured. Using BODIPY dyes **7** and **9** as examples in **Figure 4.1**, it can be noted that the dyes were able to internalise in the cells. This trend was also observed for the other dyes studied.

Table 4.1 Percentage photostability, binding energy and Log P values

PS	%Photostability	Binding Energy (Kcal/mol)	Log P
2	20	+11.53	0.45
5	50	+71.53	0.53
6a	98	−5.53	0.49
6b	97	−5.92	1.12
7a	98	+467.99	−0.06
7b	99	−5.63	0.63
8a	97	+462.77	0.54
8b	96	−5.14	0.34
9a	98	$+3.63 \times 10^3$	0.24
9b	99	−5.27	0.20
10c	96	-	2.51
10d	96	-	1.25
10e	95	-	1.01
11a	98	$+1.77 \times 10^3$	0.89
11b	98	−6.24	0.56
11c	99	$+1.89 \times 10^3$	1.15

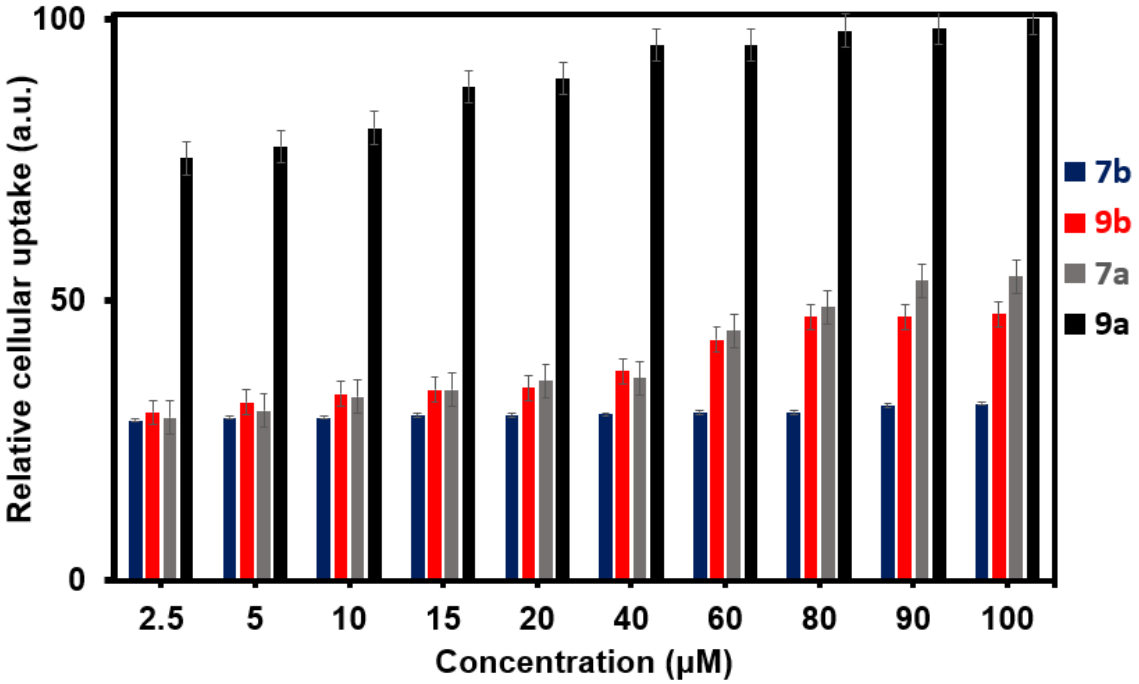

Figure 4.1 Concentration dependence cellular uptake of BODIPY dyes **7a**,**7b**, **9a** and **9b** by MCF-7 cells. The error bars denote standard deviation.

Additionally, the photostability of the molecules was determined under the same conditions as that of the bioassays. The PS dyes were irradiated for 30 minutes. All the molecules showed great photostability except for BODIPY dyes **2** and **5**, which contain *meso*-ferrocenyl moieties. **Figure 4.2** provides examples of the photostability studies for the porphyrin **11** and BODPY dye **7** series. The percentage photostability values determined for the remaining dyes are tabulated in **Table 4.1**.

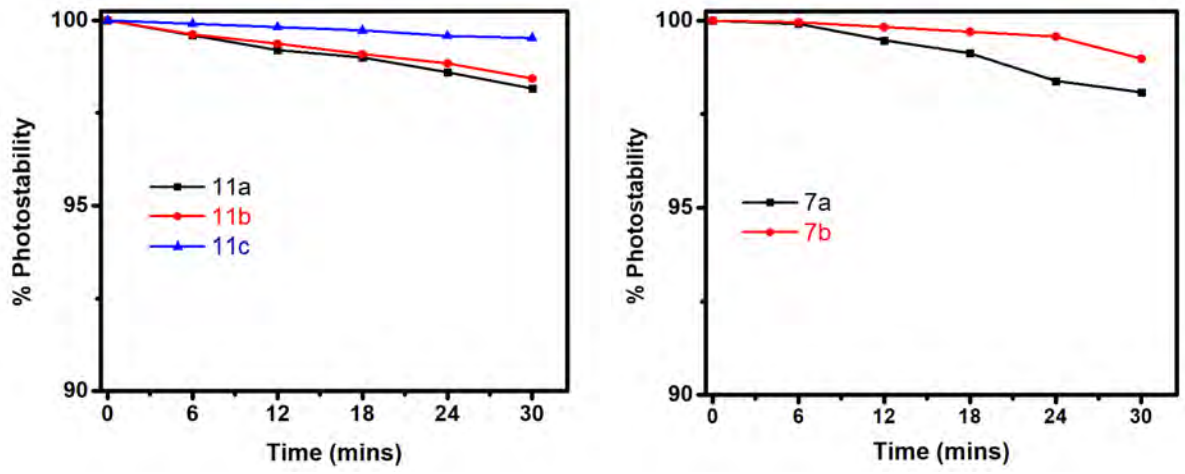

Figure 4.2 Percentage photostability of **7a**, **7b**, **11a**, **11b,** and **11c** under the exact conditions of the bioassay studies.

4.1 Molecular docking

In silico molecular docking was carried out using Human Serum Albumin (HSA), the most abundant protein in human plasma.[199–202] This protein can deliver drugs to their target organs/tissues when the drug moiety binds to it. Thus, HSA does not only alter the pharmacokinetic and pharmacodynamic properties of the drug but influences the *in vivo* drug distribution and protects the drug from oxidation.[185] Bearing in mind the high concentration of HSA in the blood, the ability of drugs to bind to HSA is a vital factor to consider when designing new PS drugs. Moreover, the capacity of drugs to simultaneously bind to HSA can potentially modulate the final therapeutic efficiency of

the drug and also change the binding behaviour of HSA.[185] Therefore, it is vital for the PS to bind simultaneously to HSA to improve its bioavailability to the target site, thus, enhancing its efficacy during *in vivo* PDT studies. The binding energies in **Table 4.1** display both positive and negative binding energies. A PS with a negative binding energy can spontaneously bind to HSA. This results in greater efficacy because their biodistribution will be enhanced. On the other hand, a PS dye with a positive binding energy will have poor bioavailability due to nonspontaneous binding to HSA.

Figure 4.3 shows how well the PS dyes fit in the receptor pocket using the BODIPY **7** and porphyrin **11** series as examples. All the dyes found a place to occupy on the protein. This trend was observed with the rest of the PS dyes. Additionally, despite the dyes with negative binding energies finding a place further away from the ligand-receptor pocket, this was still within the grind box. **Figure 4.4** displays a 2D diagram of PS dyes interacting with the amino acids of the protein. The BODIPY **7** series is used as an example. From this figure, **7a** has more interactions than **7b**. This is consistent with how well the dye fits in the receptor pocket in **Figure 4.3**.

The interaction of the porphyrin **10** series with HSA was not investigated as they are too large to be treated as a ligand in molecular docking. Docking validations were performed by reconstructing the cocrystallised ligand, and later redocking was conducted. The reconstructed ligand was fit in the same exact location as the cocrystallised ligand (**Figure 4.4**) with a binding energy of −6.43 kcal/mol, proving that docking was carried out efficiently.

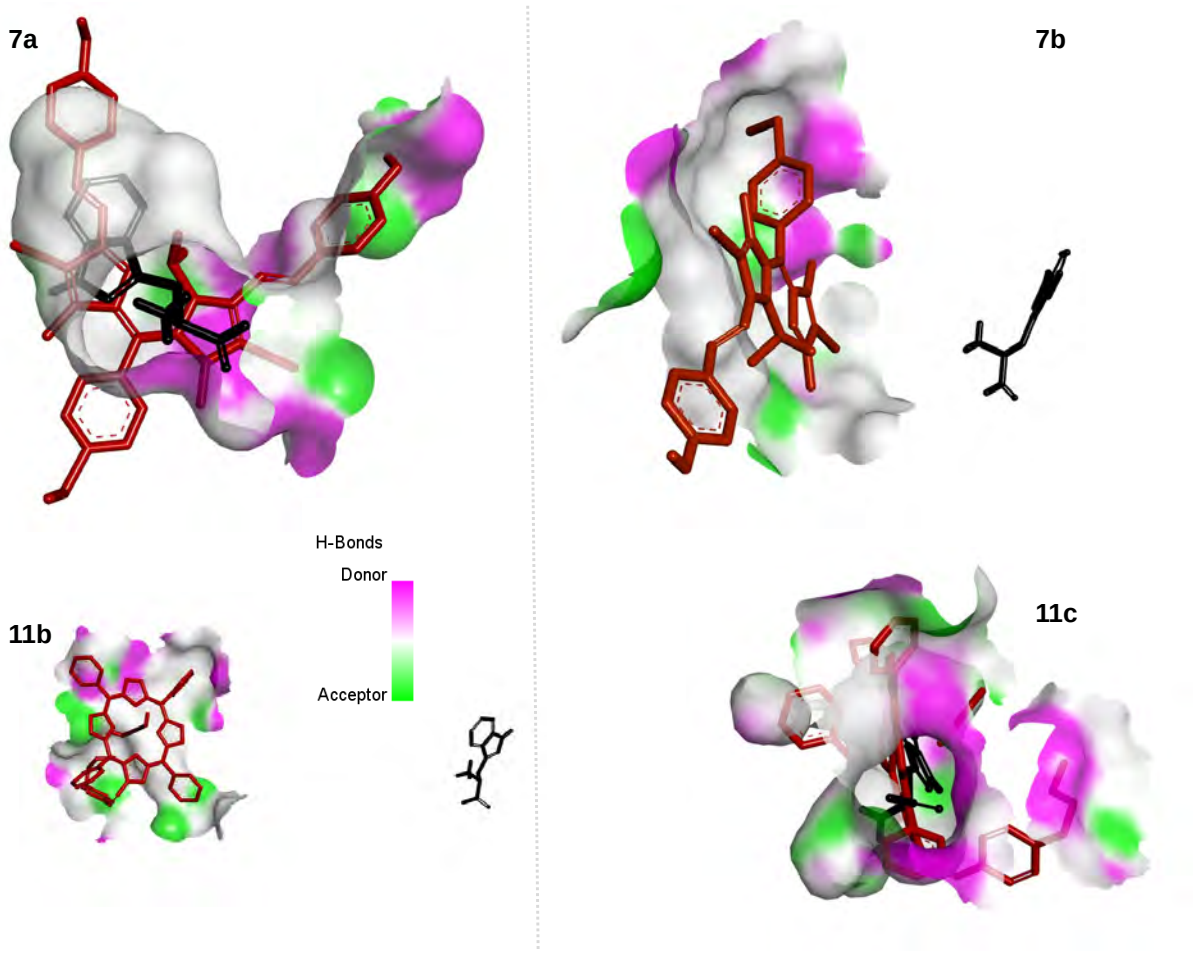

Figure 4.3 3D receptor-ligand interaction of compounds **7a**, **7b**, **11b,** and **11c** in red and the cocrystallised ligand in black.

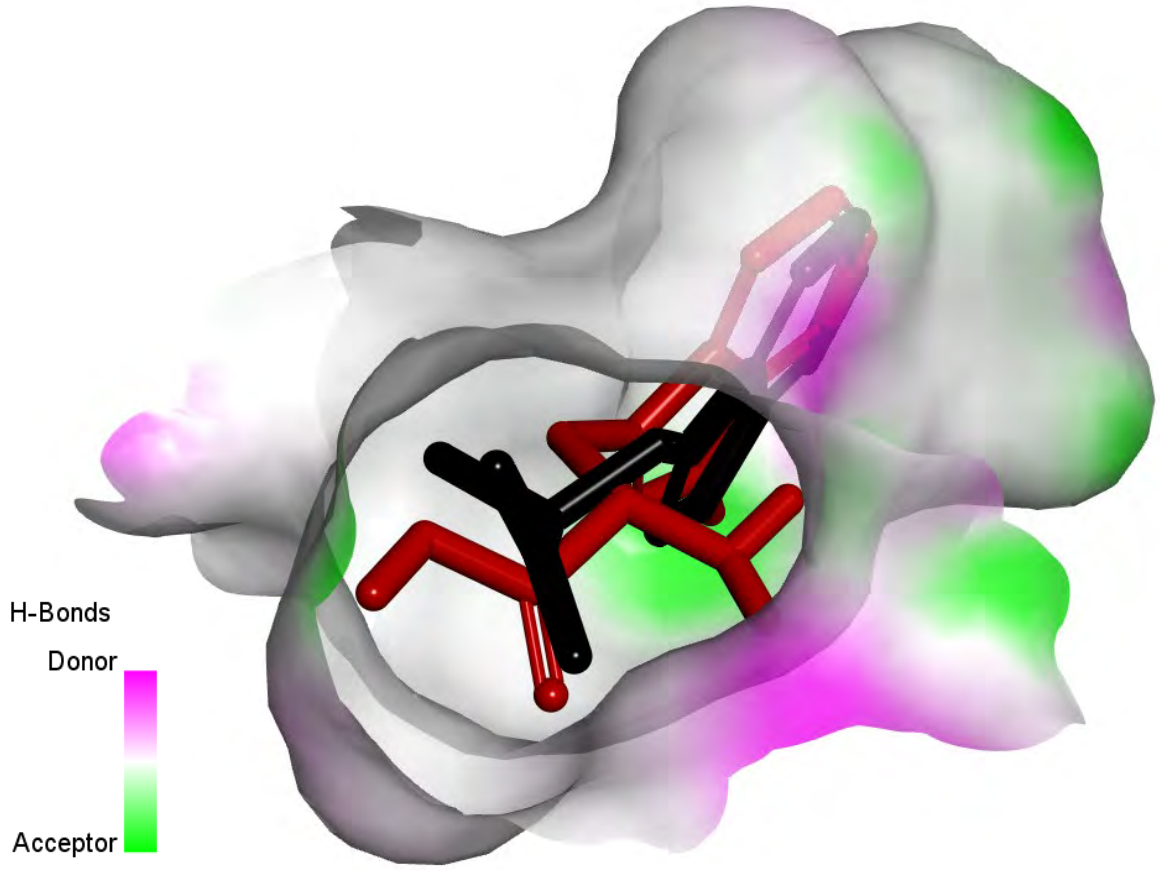

Figure 4.4 3D receptor-ligand interaction of the redocked ligand in red and the cocrystallised ligand in black.

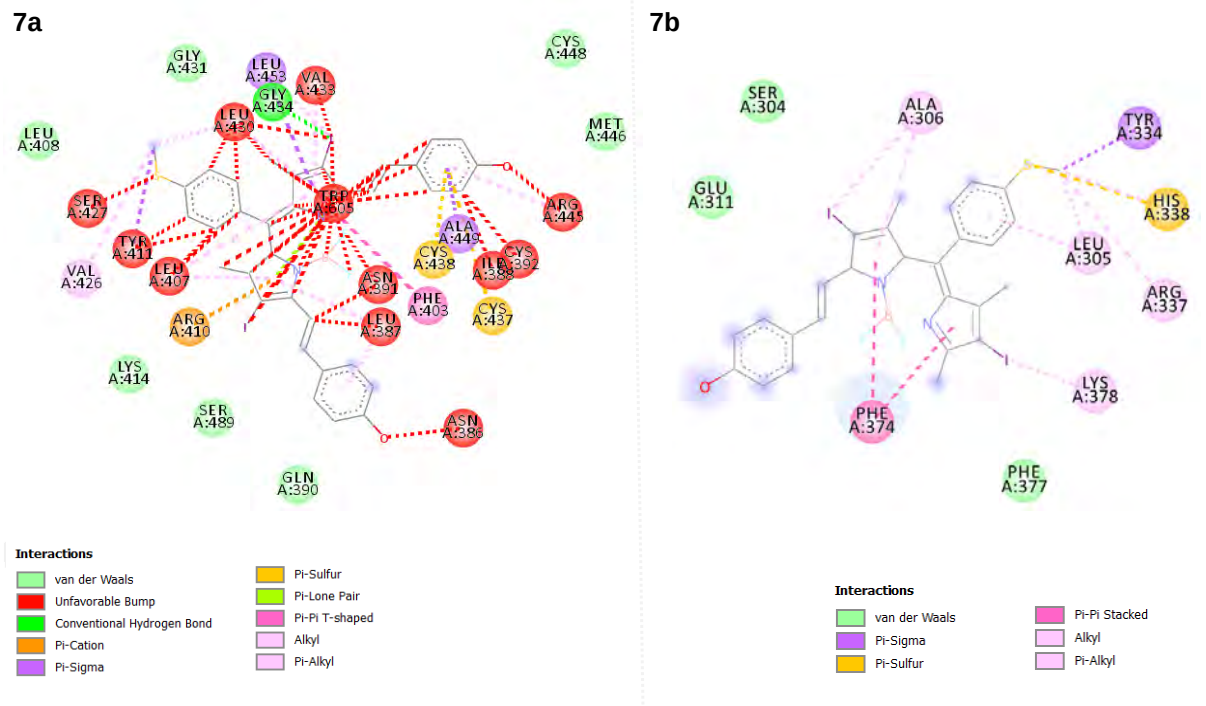

Figure 4.5 2D receptor-ligand interaction of **7a**, **7b**, **11b** and **11c**.

4.2 Concluding remarks

Lipophilicity, photostability, and molecular docking studies were carried out successfully. All the molecules had favourable lipophilicity properties for PDT except for **7a,** which had a value that was out of the range recommended by Lipinski's Rule of Five. Regarding photostability, the porphyrins were more photostable than the BODIPY dyes. However, in the context of molecular docking with HSA, the BODIPY dyes were predicted to have better binding energies than the porphyrins. Specifically, the mono-substituted BODIPY dyes had lower binding energies than the di-substituted dyes. The mono-substituted dyes recorded negative binding energies, implying that their binding to HSA was spontaneous.

Chapter five

This chapter contains the anticancer and antibacterial photodynamic activities.

5. Bioassays

5.1 Anticancer photodynamic activities

All anticancer studies were conducted using 1% DMSO since some of the dyes were not cationic and had poor solubility in aqueous solution. The *in vitro* studies were carried out in triplicate for assurance, validation, and reliability of the results using the MCF-7 breast cancer cell line and HeLa cells. MTT assay was used to determine the percentage viability of the cells treated with the dyes under investigation. In these experiments, both the light and dark toxicity of the compounds were evaluated, and this was accomplished by calculating the half-maximal inhibitory concentration (IC_{50}) value. IC_{50} is a measure of the efficacy of a substance in inhibiting a specific biological or biochemical process, and it also indicates how much of the pharmacological agent is required to inhibit the biological activity by half.[133] **Table 5.1** provides a summary of IC_{50} values for all the compounds, and **Equation 5.1** was used to quantify the %viability of the cells.

$$\% \text{ cell viability} = \frac{(A - B)}{A} \times 100 \qquad \textbf{5.1}$$

5.1.1 *In vitro* cytotoxicity studies in the dark and light of BODIPYs 6a, 6b and 9a, 9b.

5.1.1.1 Photodynamic effect

The *in vitro* toxicity studies against MCF-7 breast cancer cell lines were executed under illumination and dark to determine the potential utility of **6a**, **6b**, **9a,** and **9b** as photosensitisers in PDT. These studies were carried out at a concentration range of

1.5−100 µM. A Thorlabs M625L3 625 nm light-emitting diode (LED) with an irradiance value of 240mW/cm^2 mounted on the Modulight® Medical 7710-680 laser was used for light studies of **6a** and **9b**, while Thorlabs M730 730 nm light-emitting diode (160 mW/cm^2) and M660L4 660 nm light-emitting diode (280 mW/cm^2) were used to photosensitise **9a** and **6b**, respectively. The cells were irradiated for 30 min after being incubated with the dyes for 24 h. All the photosensitisers exhibited minimal dark cytotoxicity, but their cytotoxicity was enhanced upon light exposure. BODIPY dyes **6a** and **6b** had more desirable IC_{50} values in **Table 5.1** than **9a** and **9b**, which had an IC_{50} > 15 µM. The enhanced cytotoxicity in light studies is probably primarily related to the greater ability of the molecules to generate singlet oxygen.

Additionally, **6a** and **6b** have higher phototoxicity index values in **Table 5.1** than **9a** and **9b**. Thus, this makes them more desirable for use as photosensitisers. The photodynamic activities of **6a**, **6b**, **9a,** and **9b** are displayed in **Figure 5.1**.

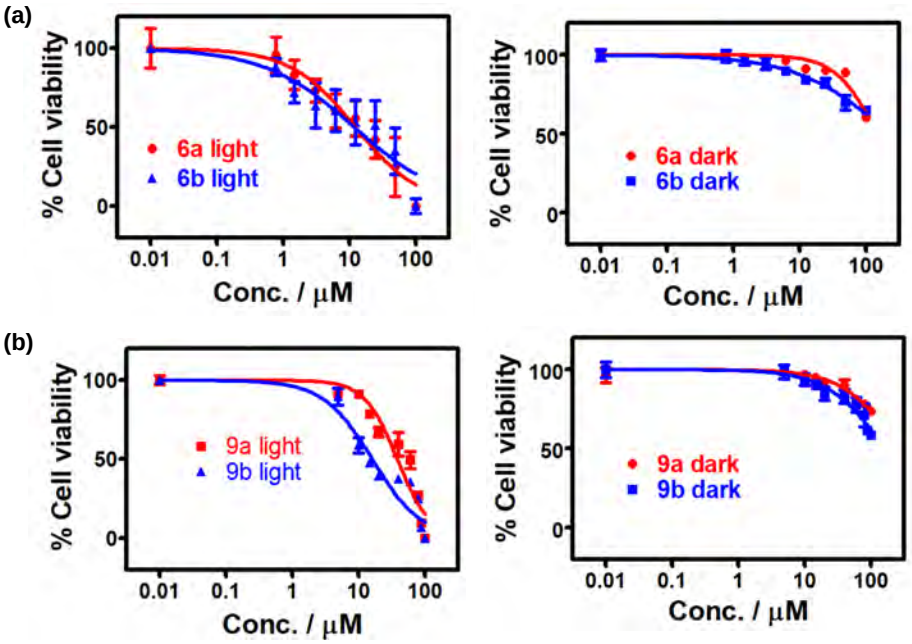

Figure 5.1 Cytotoxicity of BODIPY dyes (a) **6a**, **6b** and (b) **9a, 9b** against MCF-7 cells after an incubation time of 24 h in the dark. The MTT assay was used to evaluate the phototoxicity. The error bars denote standard deviation.

5.1.1.2 Cell imaging

Figure 5.2 displays the effect on MCF-7 cells of **6a** and **9b** (used as examples) before and after 30 min irradiation or associated dark toxicity studies. The cells in the control studies were fully confluent, but upon light treatment, there was a decrease in the MCF-7 cell confluence, with **6a** having greater phototoxicity. Both compounds exhibited minimal dark cytotoxicity. This can be observed from the cell confluence that is maintained in the dark toxicity studies.

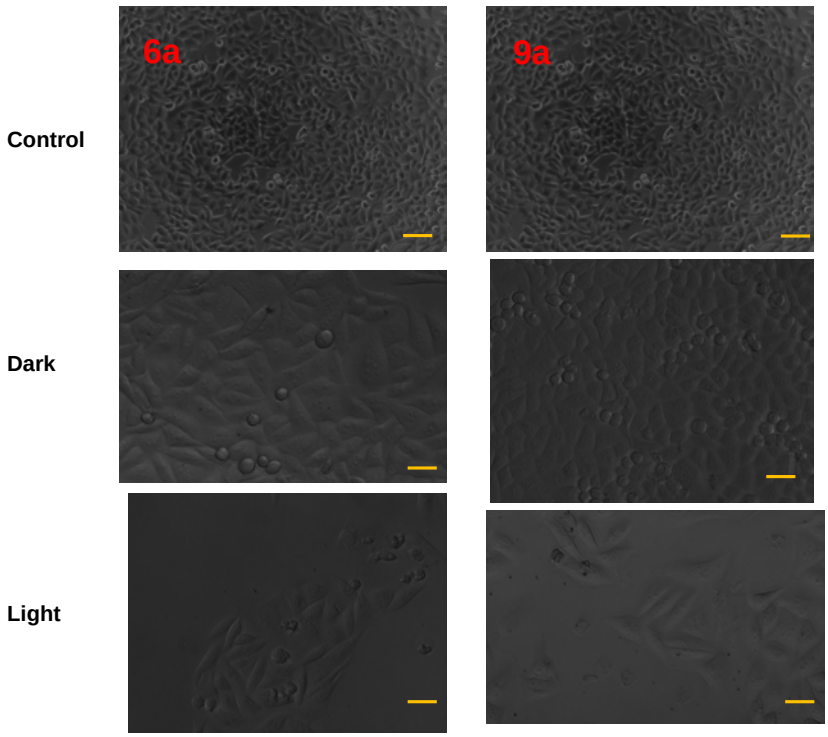

Figure 5.2 MCF-7 morphological changes observed before treatment with **6a** and **9a** (control) at 12 μM, in the absence of irradiation (dark) and after irradiation with a Thorlabs LED of an appropriate wavelength (light studies) (Scale bar 200 μm).

5.1.2 *In vitro* cytotoxicity studies in dark and light for BODIPYs 7a, 7b and 8a, 8b.

5.1.2.1 Photodynamic effect

In vitro studies of BODIPY dye (**7a**, **7b**) and (**8a**, **8b**) were carried out over a concentration range of 1.5−100 μM. A Thorlabs M660L4 660 nm light-emitting diode

(280 mW/cm^2) was used to photoexcite compounds **7a** and **8a**, while an M625L3 light-emitting diode (240mW/cm^2) was used for mono-styryl dyes **7b** and **8b**. The 96 well plates containing MCF-7 cells were treated with the dyes and incubated for 24 h to allow for drug uptake by the cells. The plates were irradiated with LED as stated above for 30 min. The BODIPY **8** series has lower dark toxicity than the BODIPY **7** series, **Table 5.1** and **Figure 5.3**. All the dyes display activities characteristic of singlet oxygen generation during bioassay studies, since there is a marked enhancement of cytotoxicity in light studies compared to dark. From **Table 5.1** the BODIPY **7** series have lower IC_{50} values than the BODIPY **8** series, as would be anticipated based on the singlet oxygen quantum yield results in **Table 3.1**, which showed BODIPY **7** had high singlet oxygen quantum yield values.

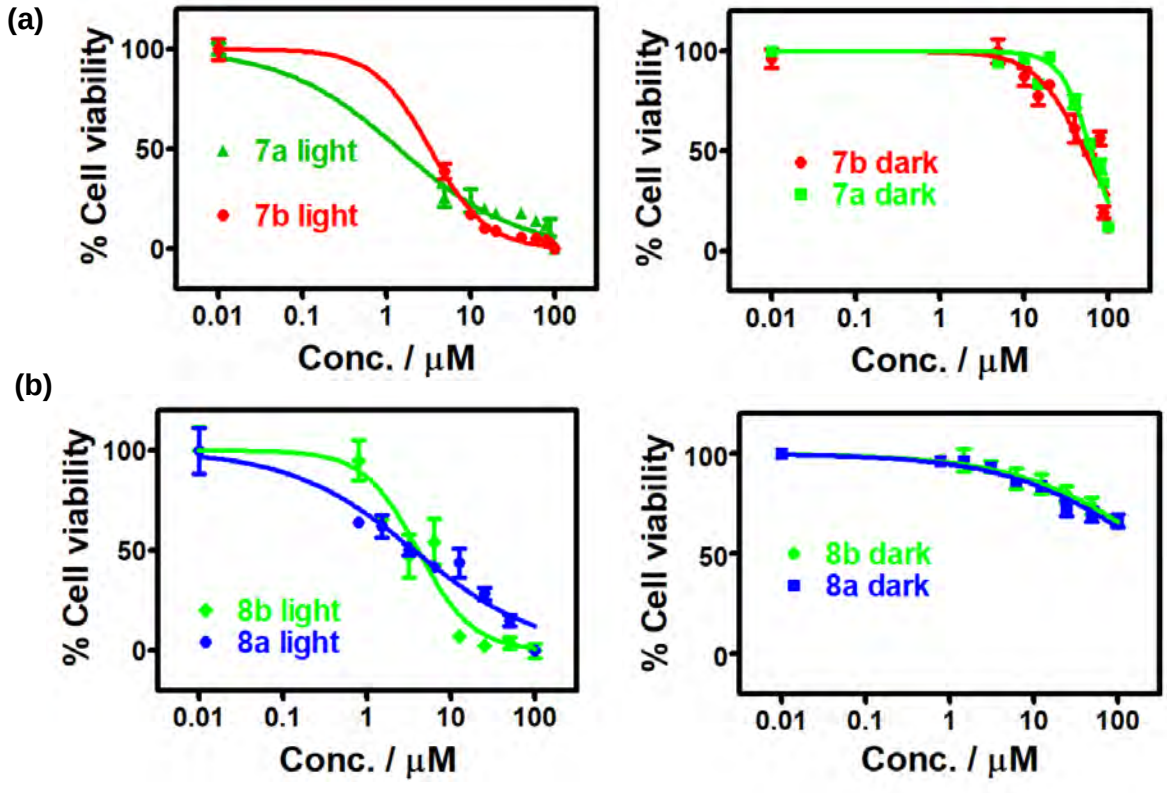

Figure 5.3 (a) and (b) Cytotoxicity of BODIPY dyes **7a**, **7b** and **8a**, **8b** against MCF-7 cells after an incubation time of 24 h in the dark, and MTT assay was used to evaluate the phototoxicity. The error bars denote standard deviation.

5.1.2.2 Cellular imaging

Figure 5.4 shows the cellular morphology of MCF-7 cells before photosensitise loading (control), after photosensitiser loading (dark), and after photosensitising with the PS (light) using **7b** and **9b** as examples. There was less morphological damage caused by both compounds in the dark, as anticipated based on the high IC_{50} value of the compounds, **Table 5.1**. Nonetheless, upon photosensitising with both PS dyes, there was an enhancement in the cell shape damage experienced by MCF-7, which was attributed to the ability of the molecules to produce singlet oxygen in **Table 3.1**. The BODIPY **7** series caused more morphological damage in light studies because of their relatively high singlet oxygen quantum yield values.

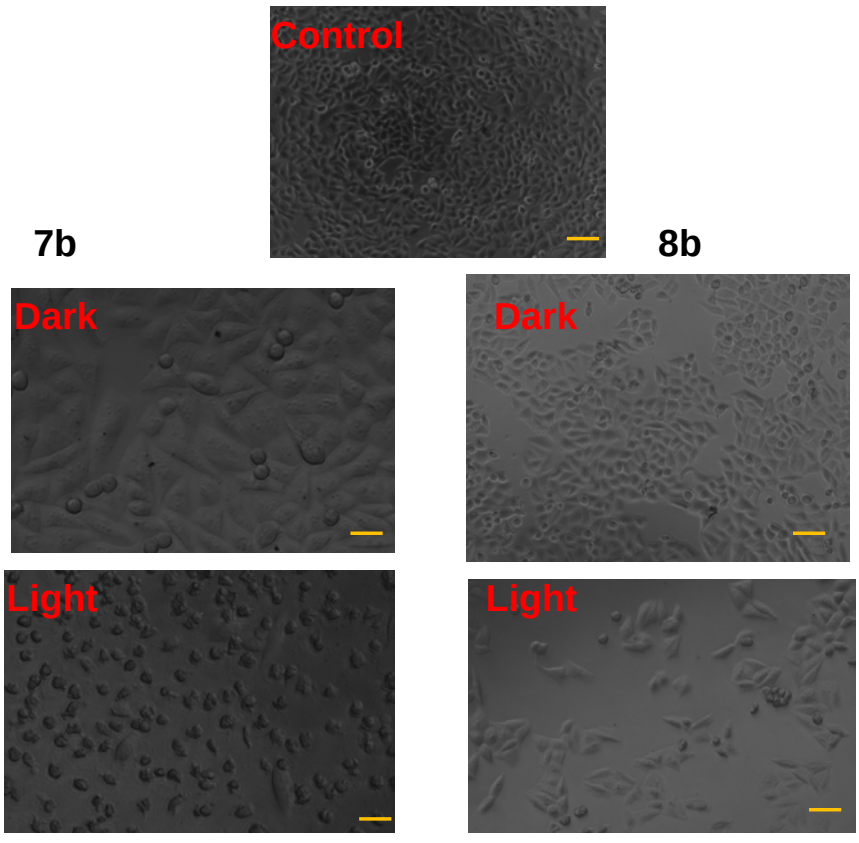

Figure 5.4 MCF-7 morphological changes observed before treatment with **7b** and **9b** (control), minus irradiation (dark) and after irradiation with a Thorlabs LED of an appropriate wavelength (light studies) at 12 μM (scale bar 200 μm).

5.1.3 In vitro cytotoxicity studies in dark and light of porphyrin 10 and 11 series

5.1.3.1 Photodynamic studies

The *in vitro* photodynamic activities of porphyrin **10** and **11** series on HeLa cells were carried out by using the MTT assay. These studies were conducted over a range of 1.5−100 μM, and all the compounds were solubilised in 1% DMSO. A Thorlabs M625L3 625 nm light-emitting diode (240 mW/cm^2) mounted on a Modulight® 7710-680 Medical Laser was used for the light studies. The free base porphyrins were used as control compounds. Interestingly, all the compounds exhibited minimal dark cytotoxicity with IC_{50} values > 100 μM for all the porphyrin dyes, **Figure 5.6**.

After 24 h of incubation with the photosensitiser, the cells were irradiated for 30 min, and the dose-dependent photocytotoxicity is shown in **Figure 5.5**. The IC_{50} values were determined based on the dosage response curve. The free base controls for both porphyrin series exhibited the highest and hence least favourable IC_{50} values because they had the lowest singlet oxygen quantum yield value in **Table 3.1**. **11c** has the more favourable IC_{50} value, but both compounds had similar phototoxicity index values. Porphyrin **10d** had a lower IC_{50} value than the analogous metallated porphyrin **11b**, and the same trend was observed for **10e** and **11c**. It can be noted that the porphyrins with axial ligands exhibited much more desirable IC_{50} values. This is attributed to the axial ligands eliminating the problem of aggregation, which can lower the efficiency of the photosensitisers because nonradiative decay mechanisms are enhanced. When

the activity of the porphyrins is compared to that of the BODIPY dyes, the porphyrins were found to have significantly enhanced cytotoxicity due to their high singlet oxygen quantum yield values.

Additionally, the **10** porphyrin series had better cellular uptake due to their cationic and mitochondria targeting properties. It has been proven in previous studies that the mitochondria of cancer have high membrane potential ($\Delta\Psi_m$ = −220 mV)[203] compared to normal cells (−160 mV).[203] This means that cationic compounds localise preferentially in the mitochondria. Hence, we observe greater reactivity for the porphyrin **10** series because it is more cationic than the porphyrin **11** series.

5.1.3.2 Cellular imaging

The morphological damage on HeLa cells caused by porphyrin **10e** and **11c** (used as examples) is shown in **Figure 5.6**. Since these porphyrins had minimal dark toxicity, it was expected that the cells in the dark would still maintain a high confluence (i.e. cover a large surface area). When the dyes were photosensitised, the dose-dependent response was enhanced. Thus, we observe a decrease in cell confluence under light studies corresponding to the results reported in **Figure 5.5** and **Table 5.1**.

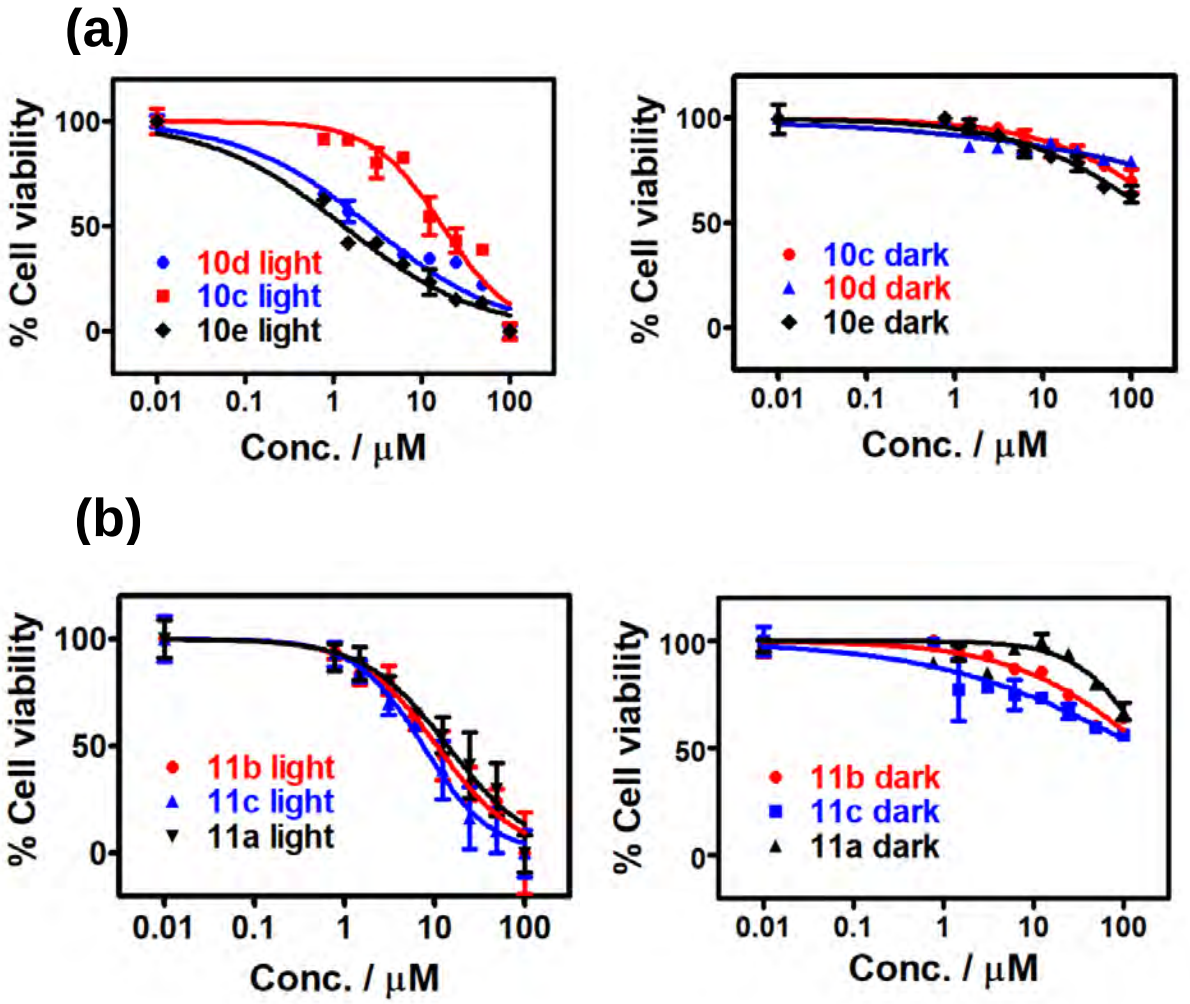

Figure 5.5 (a) and (b) dose-dependent photocytotoxicity response of the porphyrins against HeLa cells in the dark and upon irradiation with a Thorlabs M625L3 625 nm LED (240 mW/cm^2). The error bars denote standard deviation.

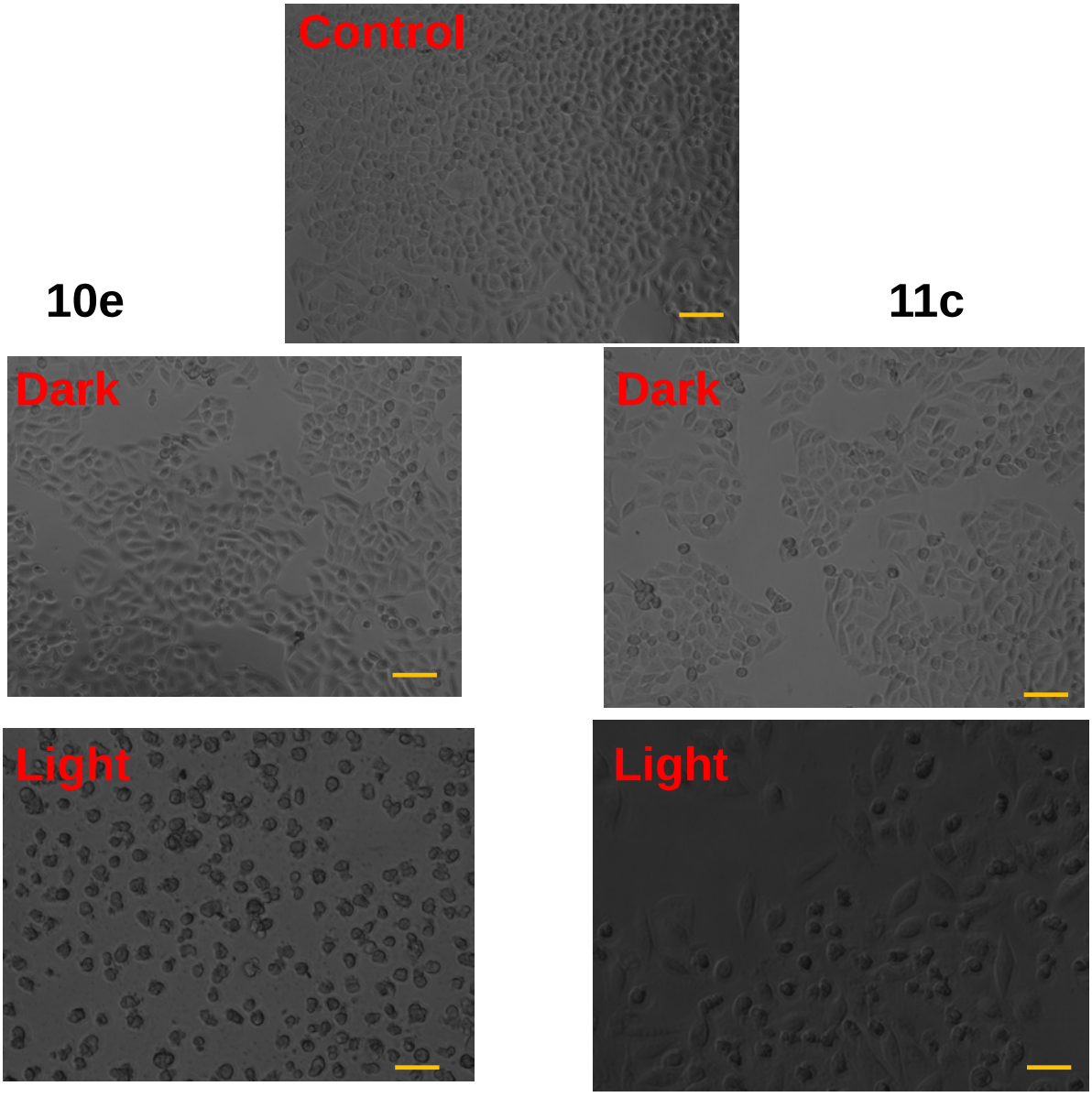

Figure 5.6 Morphological changes observed in HeLa cells before treatment with **10e** and **11c** (control), in the absence of irradiation (dark) and after irradiation with Thorlabs LED of appropriate wavelength (light studies) at 12 μM (scale bar 200 μm).

Table 5.1 IC_{50} values of the synthesised compounds against MCF-7 cells for BODIPY dyes and HeLa cells for porphyrins

	IC_{50} (μM)		PI[c]
	light[a]	dark[b]	
6a	12.5	> 100	> 8.0
6b	12.0	> 100	> 8.3
7a	3.34	> 50	> 15.0
7b	1.43	> 50	> 35.0
8a	4.04	> 100	> 24.8
8b	3.64	> 100	> 27.5
9a	34.2	> 100	> 2.9
9b	15.4	> 100	> 6.5
10c	17.6	> 100	> 5.7
10d	2.70	> 100	> 37.0
10e	1.34	> 100	> 74.6
11a	14.2	> 100	> 7.0
11b	10.8	> 100	> 9.3
11c	7.61	> 100	> 13.1

[a] 24 h incubation in the dark followed by irradiation with a Thorlabs LED of appropriate wavelength.
[b] 24 h incubation in the dark.
[c] Phototoxicity index (PI) ratio of dark and light IC_{50} values.

5.2 Photodynamic antimicrobial chemotherapy (PACT)

All the antimicrobial studies were carried out in 2% DMSO to enhance compound solubility. *Staphylococcus aureus*, a gram-positive bacterium, was used. PACT studies were conducted using a previously reported procedure for turbidimetric studies.[177] **Equations 5.2** and **5.3** were employed to quantify % colony viability and log reduction, respectively.

$$\% \text{ Colony viability} = \frac{(A - B)}{A} \times 100 \quad \textbf{5.2}$$

$$\text{Log reduction} = \text{Log}(A) - \text{Log}(B) \quad \textbf{5.3}$$

Where A is the number of colonies before treatment with the photosensitiser while B represents the number of colonies after treatment with a photosensitiser. A lower percentage colony viability indicates higher photosensitiser potency, and such molecules record a high log reduction. A log reduction of 3 is the minimum value which has been recommended by the FDA for this application for a dye to be considered a photoantimicrobial agent.[204]

5.1.1 Concentration optimisation studies

The concentration optimisation studies were conducted both in the dark and under illumination. These studies were carried out to identify the minimum concentration capable of completely eradicating the colonies upon light exposure. BODIPY dye **7a** and **7b** are used as examples. **Figure 5.7** displays the concentration optimisation of these molecules, while **Figure 5.8** displays the colony morphological damage. From this figure, it is noteworthy that PACT activity increases at higher dye concentrations and both dyes exhibit minimal dark toxicity.

Nevertheless, the molecules did not exhibit significant antimicrobial activities upon light exposure for 80 min, and a similar lack of activity was observed for the rest of the BODIPY dyes that were synthesised. The insignificant cytotoxicity for this series of dyes was caused by unknown reasons, which are currently being investigated by other researchers in the research group. In contrast, the porphyrin **11** series exhibited high PACT activity at 2.5 μM. The porphyrin **10** series was not studied for PACT due to time constraints.

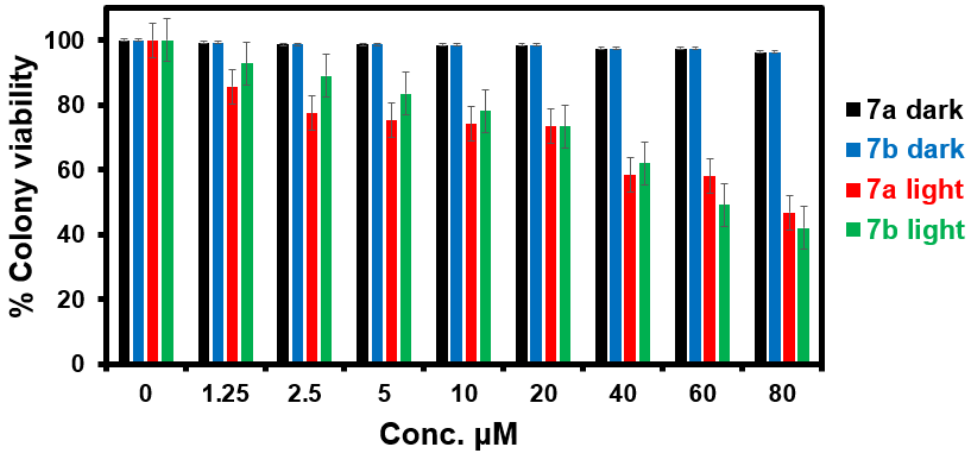

Figure 5.7 Concentration optimisation studies for BODIPY **7a** and **7b** against *S. aureus*. 625 and 660 nm Thorlabs LEDs were used for studies with **7b** and **7a**, respectively. The error bars denote standard deviation.

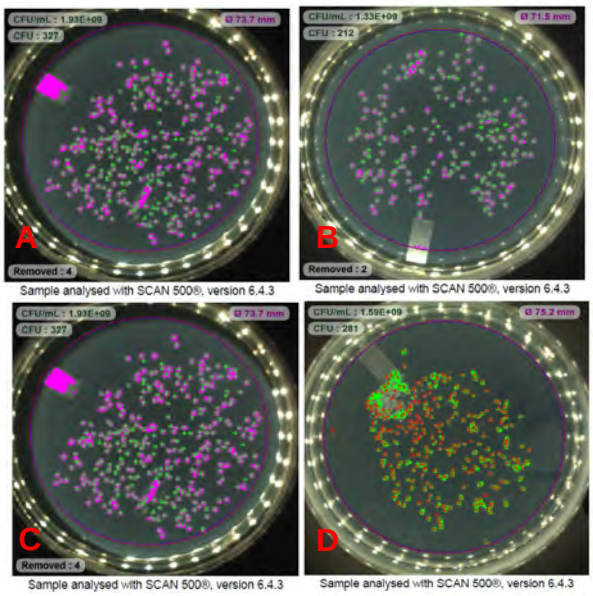

Figure 5.8 Images of *S. aureus* colonies formed (A) in the dark (control) (B) upon irradiation at 660 nm with a Thorlabs M660L3 LED using **7a** at a concentration of 80 µM. (C) and (D) are the corresponding images for **7b**, where (C) is the dark control and (B) is after light exposure.

5.1.1 Time-dependent antimicrobial studies of porphyrin 11 series

The PACT activity studies of **11a**, **11b**, and **11c** are shown in **Figure 5.9**, while **5.10** displays the morphological damage of the remaining colonies of *S. aureus* at time zero

(control) and after 80 min. A concentration of 2.5 μM was used, and a time interval of 10 min was employed. Porphyrin **11c** with axial ligands completely eradicated the bacteria after 40 min of light exposure, while **11b** had this property after 50 min (**Figure 5.9**). **11a**, which was used as a control, did not completely eliminate colonies, **Figure 5.10**, resulting in a low log reduction value of 0.11 with a percentage colony survival of 24.3. Porphyrins **11b** and **11c** had log reductions of 8.21 and 9.11, respectively, at zero colony survival. The antibacterial activity of both compounds is attributed to their high singlet oxygen quantum yield values. Additionally, cationic molecules have a property of high cellular uptake; thus, they eradicate bacteria with great efficiency.

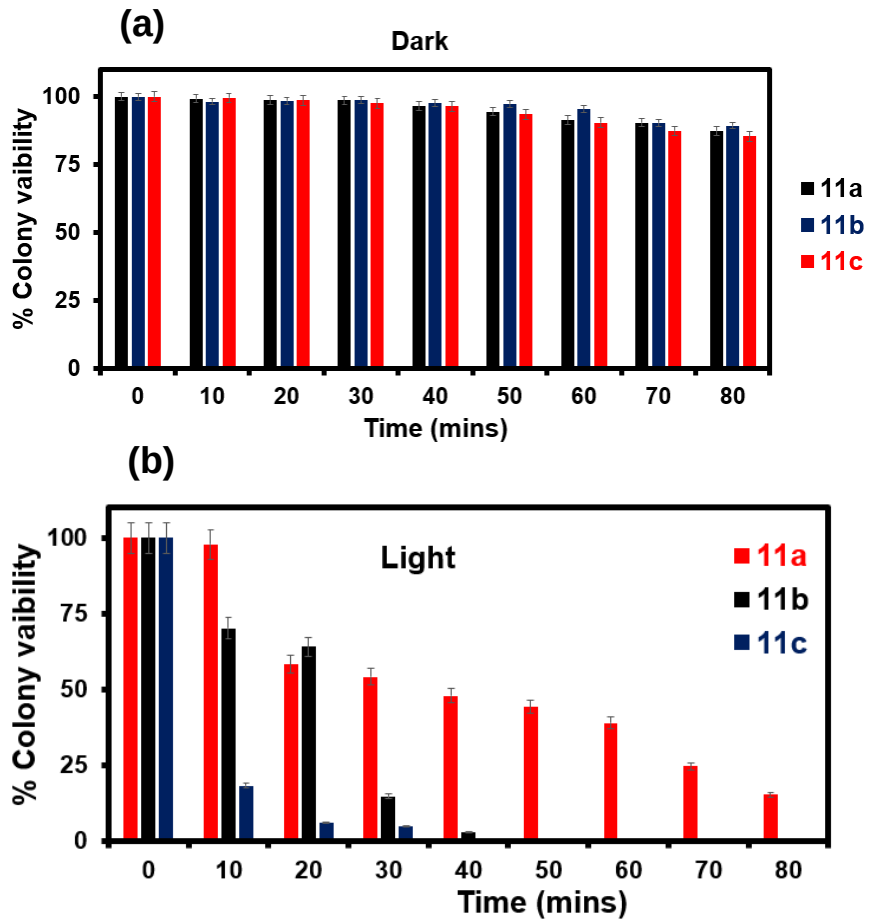

Figure 5.9 (a) Dark studies, (b) light studies upon irradiation at 625 nm with a Thorlabs M625L3 LED. The error bars denote standard deviation.

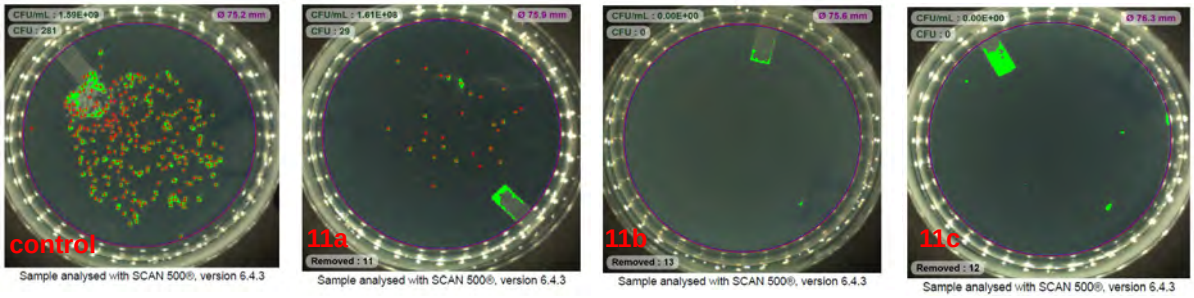

Figure 5.10 Images of *S. aureus* colonies formed after an irradiation time of 80 min using a Thorlabs M625L3 625 nm LED.

5.3 Concluding remarks

The *in vitro* photodynamic anti-cancer properties of all the molecules other than the BODIPY core dyes were evaluated. The cytotoxicity of all the dyes was enhanced upon light irradiation, and this was seen in the reduction of cell viability. It was observed that the difference in PDT activity was greatly dependent on the magnitude of the singlet oxygen value. The porphyrin **10** series displayed better photocytotoxic properties due to its ability to target the mitochondria. All the dyes had minimal dark toxicity. Additionally, the porphyrin **11** series were used as PS dyes for PACT, and their anti-bacteria properties upon exposure to light were investigated, and these molecules displayed favourable phototoxicity behaviour against *Staphylococcus aureus*.

Chapter Six

This chapter contains molecular modelling studies of BODIPY dyes and porphyrins.

6. Molecular modelling

6.1 In silico studies

In silico studies in the form of theoretical calculations were used to further elucidate the relationship between the electronic structures and optical spectra of BODIPY dyes and porphyrins that were selected for study. This process was achieved by optimising the molecular geometries, which were then used in time-dependent density functional theory (TD-DFT) calculations. The Gaussian 09 software package was used for all geometry optimisation calculations with the Becke 3-parameter, Lee-Yang-Parr (B3LYP) exchange-correlation functional and either 6-31G(d) or SDD basis sets.[205] SDD basis sets were preferred for BODIPY dyes and Sn(IV) porphyrins because it offers reasonable approximations for heavy atoms such as bromine and iodine.[84] The Coulomb-attenuated B3LYP (CAM-B3LYP) exchange-correlation functional was used for TD-DFT calculations since it contains a long-range correction that incorporates an increasing fraction of Hartree-Fock (HF) exchange as the interelectronic separation increases.[84]

6.2 Molecular modelling of BODIPY dyes

As stated in the Introduction, BODIPY dyes are usually compared to *s*-indacene dyes, which are related to aromatic $C_{12}H_{12}^{2-}$ cyclic perimeter. The nodal patterns of π-MOs in the core BODIPY dyes have a similar sequence to that of a $C_{12}H_{12}^{2-}$ cyclic perimeter; however, the presence of the boron atom and the pyrrole nitrogens lifts the MO degeneracies, and this gives rise to a well-separated non-degenerate HOMO and LUMO.[84] The energies of these frontier MOs can be rationally modified by introducing substituent groups that have either inductive or mesomeric, electron-withdrawing, or donating effects at different positions on the BODIPY core.[84]

6.2.1 Molecular modelling of BODIPY core dyes

Calculations were carried out for core dyes **1-5**, and 1,3,5,7-tetramethyl-*meso*-phenylBODIPY model complexes with protons (**H_2**), bromines (**Br_2**) and iodines (**I_2**) at the 2,6-positions. Previous studies have demonstrated that substitution with aryl rings that occurs at the *meso*- position of 1,3,5,7-tetramethylBODIPY core dyes usually has a minimal effect on the HOMO−LUMO gap. This has been attributed to the perpendicular orientation of the aryl group relative to the plane of the BODIPY core, which is caused by steric hindrance with the methyl groups.[91] In addition, the HOMO has no major MO coefficient at the *meso*-position, since it lies on a nodal plane. This means that substitution at this position has a minimal effect on the HOMO energy (**Figures 6.1**, **6.2**, and **6.3**), since only inductive effects are involved. Thus, no significant shift of the main BODIPY absorption band is observed when phenyl rings are added at the *meso*-position (**Figure 6.4**) since both the HOMO and LUMO were stabilised (**Figure 6.3**).

Figures 6.1 and **6.2** display the impact of further structural modifications on the predicted MO energies. When the *meso*-phenyl group is replaced with a ferrocene ring, the LUMO of **2** is stabilised relative to those of **H_2** and **1**, which leads to a narrowing of the HOMO−LUMO gap (**Figure 6.3**), and a red shift of the main BODIPY spectral band in **Figure 6.4**. The presence of low-lying d→d transitions associated with the ferrocene moiety accounts for the low singlet oxygen quantum yields that were obtained for **2** and **5**, which led to these dyes being set aside where the PACT and PDT studies reported in Chapter 5 were concerned. When heavy atoms are introduced at the 2,6-positions of core dye to form **3**, **4**, and **5**, the mesomeric effect associated with the halogen lone pairs alters the relative energies of the frontier π-MOs. The HOMO is destabilised relative to the LUMO (**Figure 6.3**), since it has larger MO

coefficients at the 2,6-positions, resulting in a marked bathochromic shift of the main BODIPY spectral bands of **3**, **4** and **5** (**Figure 6.4**).

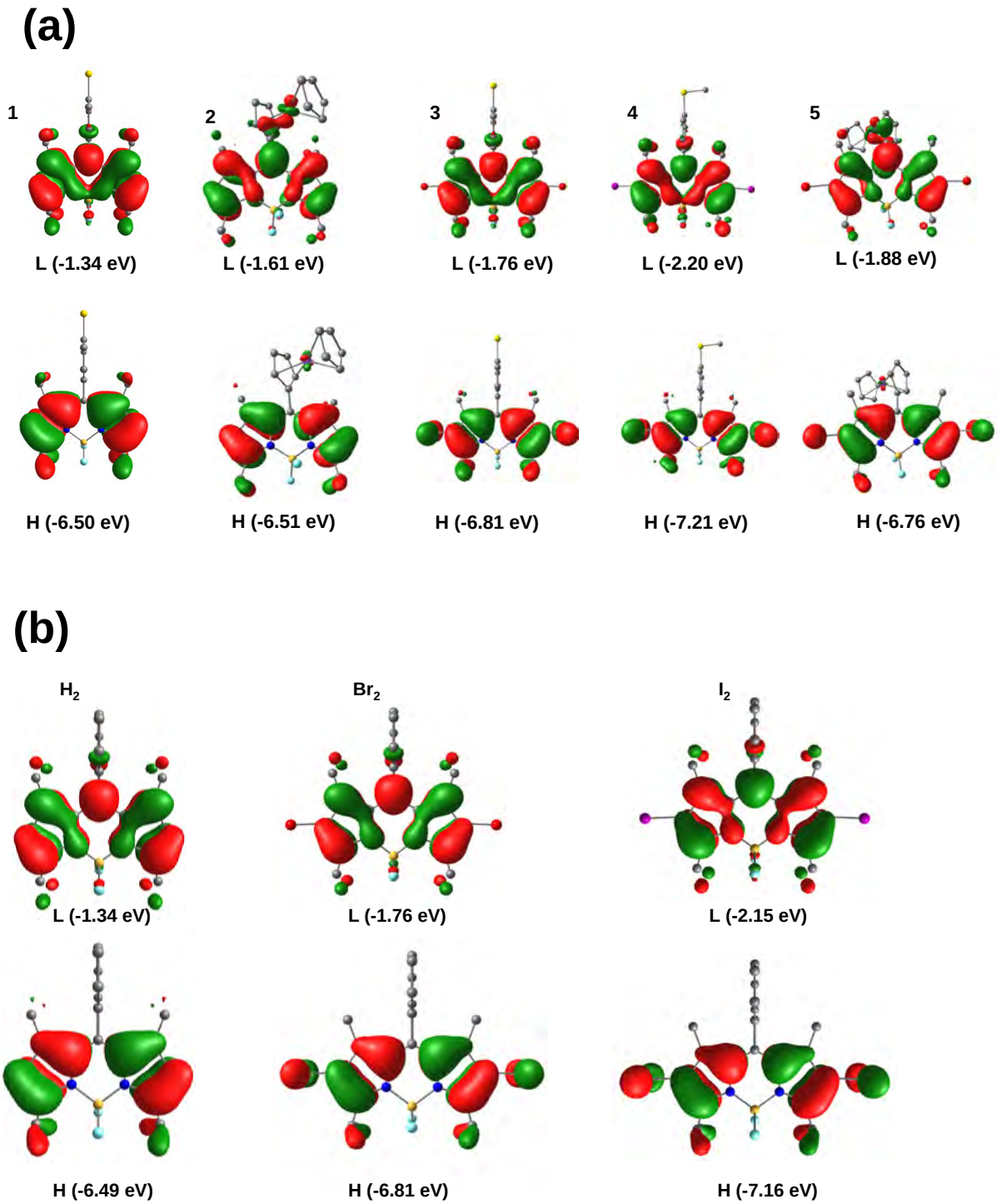

Figure 6.1 Energies and angular nodal patterns of HOMO and LUMO for BODIPY (a) core dyes **1-5** and (b) core dye **H_2**, **Br_2**, **and I_2** substituted with a phenyl ring at the

meso-position. The isosurface value was 0.03 a.u. The HOMO and LUMO are denoted as H and L, respectively. The hydrogen atoms were removed for picture quality purposes.

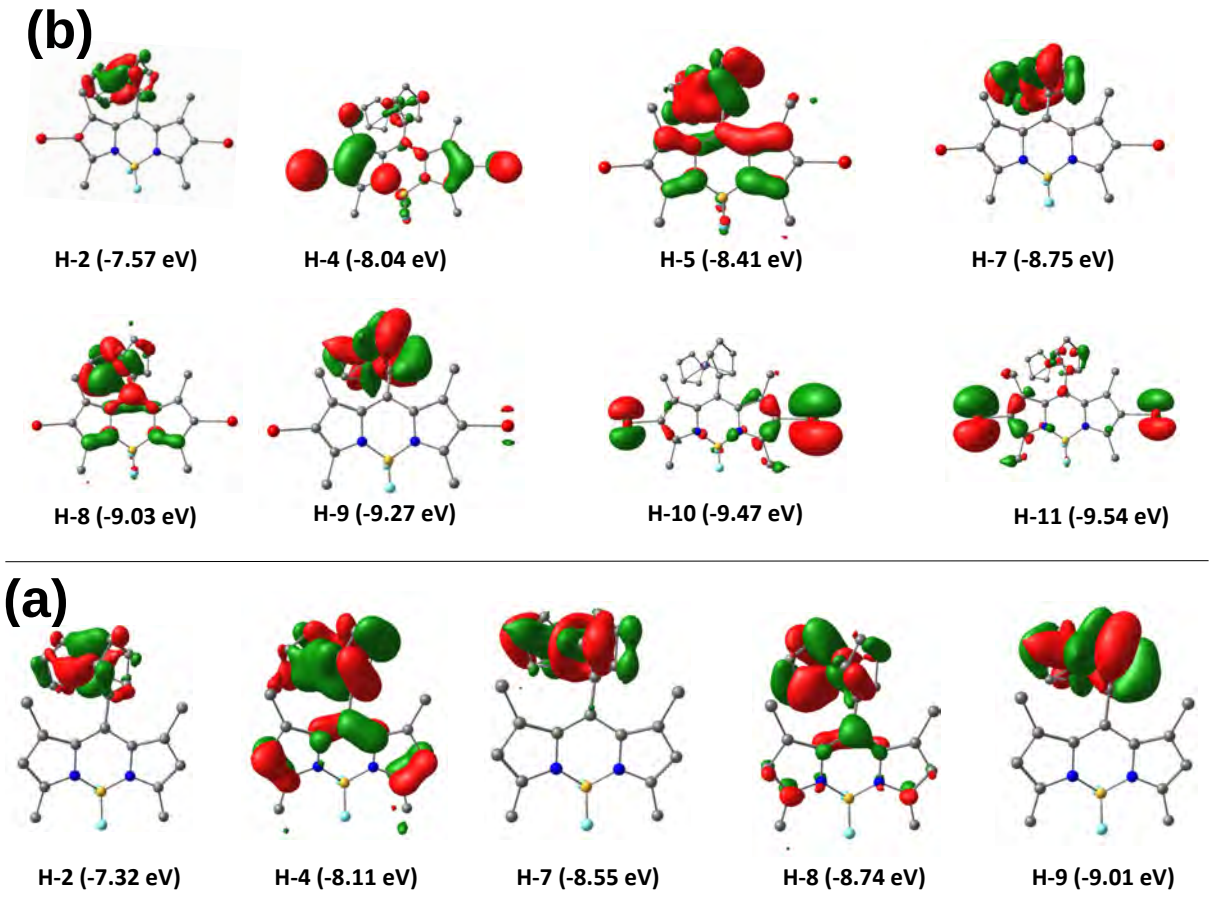

Figure 6.2 Energies and angular nodal patterns of additional MOs that are primarily localised on ferrocene moieties of dyes (a) **2** and (b) **5**. Hydrogen atoms are removed for clarity.

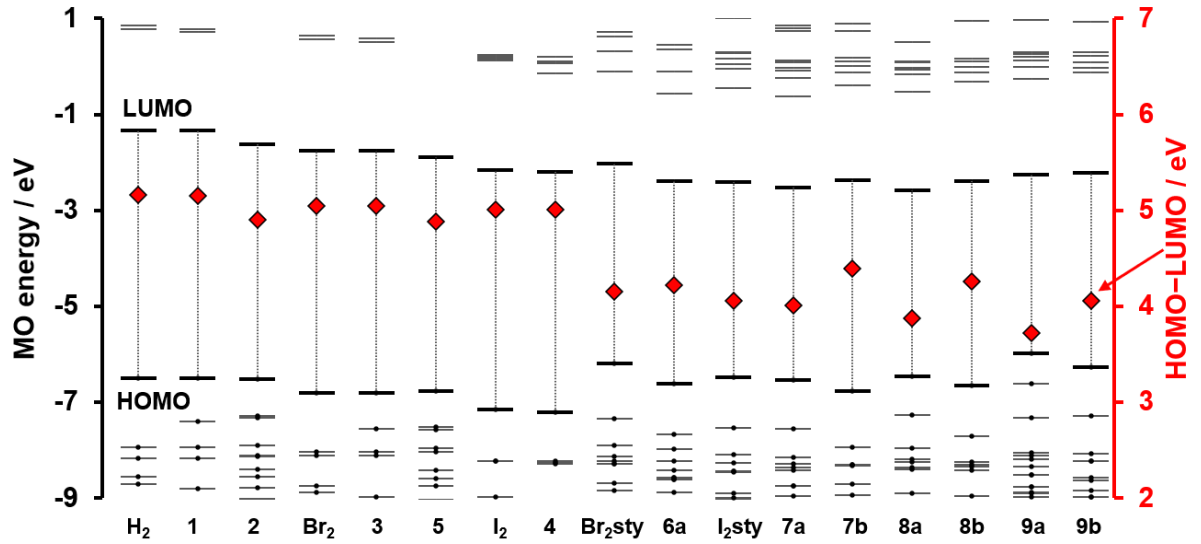

Figure 6.3 MO energies at CAM-B3LYP/6-31G(d) level of theory for synthesised BODIPY dyes. The HOMO and LUMO are highlighted with thick black lines, and the HOMO−LUMO gap values are highlighted with red diamonds and plotted against a secondary axis. Small circles are used to identify the occupied MO.

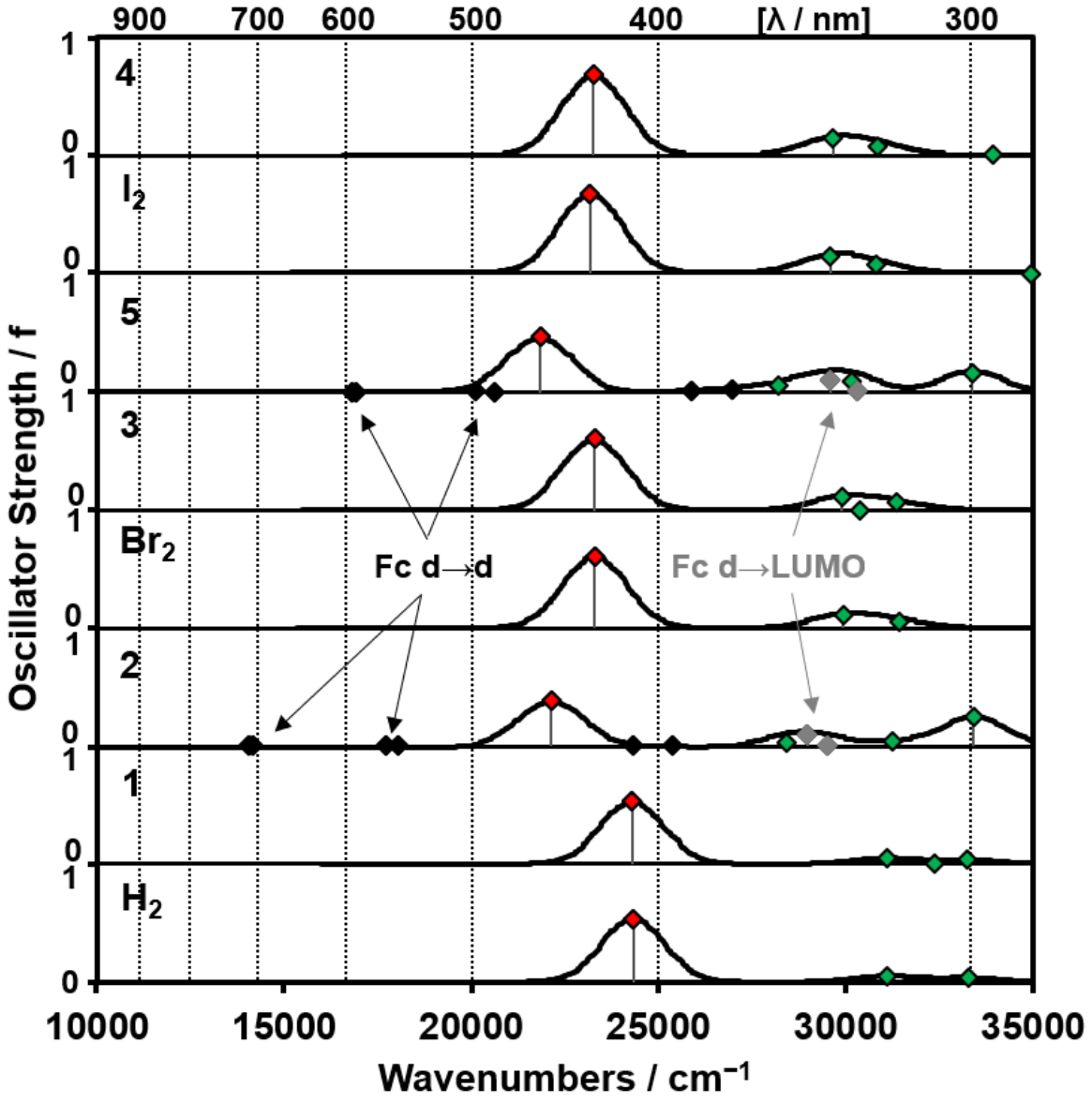

Figure 6.4 The calculated spectra of BODIPY core dyes at the CAM-B3LYP/SDD level of theory. Chemcraft was used to generate the simulated spectra at 2000 cm^{-1} bandwidth. The red diamonds represent the main absorption band. Details of the spectra are provided in the Appendix as **Table 8.2**.

6.2.2 Molecular modelling of π−extended dyes

Figure 6.1 provides the angular nodal patterns of the core dyes. It can be noted that the HOMO of all the dyes contain major MO coefficients at the 3,5-positions. This implies that modification with substituents providing an electron-donating mesomeric effects at these positions will cause a destabilisation of the HOMO relative to the LUMO, leading to a narrowing of the HOMO−LUMO gap. In this study, π-extension of the BODIPY chromophore was achieved through Knoevenegal condensation reactions of **3** and **4** with 4-pyridinecarboxaldehyde, 4-acetoxybenzaldehyde, 3,4-dihydroxybenzaldehyde, and morpholinecarboxaldehyde.

Calculations were carried out for π-extended dyes **6a**, **7a**, **7b**, **8a**, **8b**, **9a**, **9b** and 1,7-dimethyl-3,5-distyryl-*meso*-phenylBODIPY model complexes with bromines (**Br_2sty**) and iodines (**I_2sty**) at the 2,6-positions. The π-extension with styryl substituents at the 3,5-positions disrupts the electron density of the HOMO relative to the LUMO due to the major MO coefficients at these positions. This results in a relative destabilisation of the HOMO (**Figures 6.3**, **6.5**, and **6.6**) caused by the larger mesomeric effect associated with the extension of the π-conjugation system. As anticipated on this basis, the HOMOs of di-substituted BODIPY dyes **7a**, **8a** and **9a** undergo a more significant destabilisation than mono-substituted dyes **7b**, **8b** and **9b**. This causes a narrowing of the HOMO−LUMO gap, resulting in a large red shift of the main BODIPY absorption bands (**Figures 6.7**), with compound **9a** having the greatest shift, while smaller red shifts are predicted for the mono-substituted dyes (**Figure 6.7**).

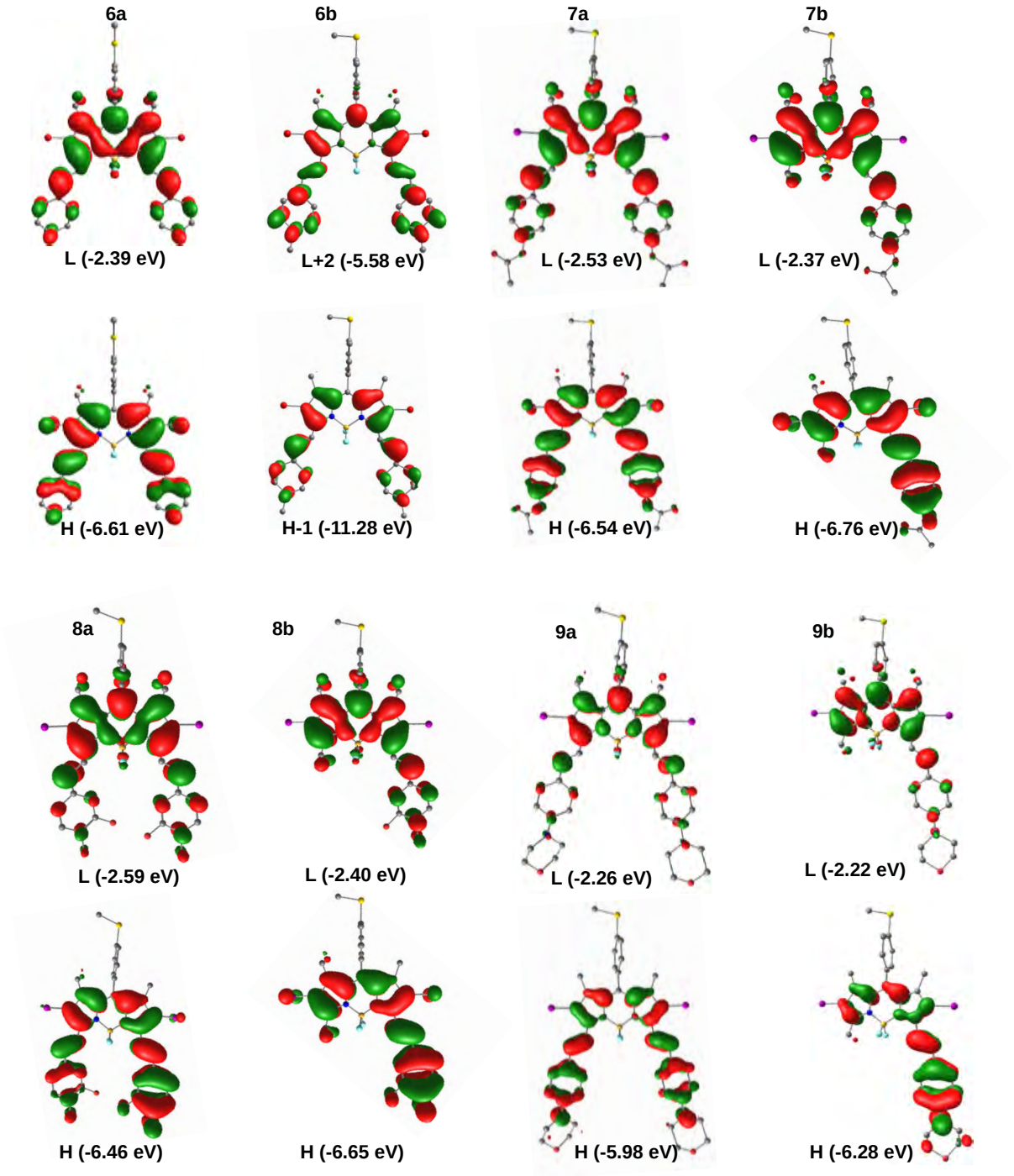

Figure 6.5 Energies and angular nodal patterns of HOMO and LUMO for dyes with an extended π-conjugation system. The isosurface value was 0.03 a.u. The HOMO and LUMO are denoted as H and L, respectively. Hydrogen atoms were removed for clarity.

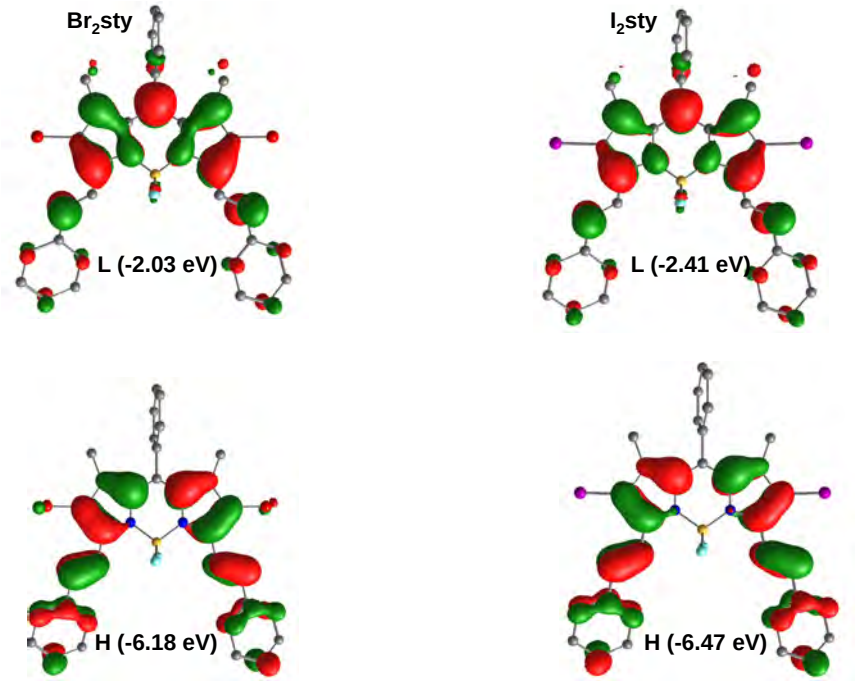

Figure 6.6 Energies and angular nodal patterns of HOMO and LUMO for dyes with a phenyl ring at the *meso*-position and an extended π-conjugation system. The isosurface value was 0.03 a.u. The HOMO and LUMO are denoted as H and L, respectively. Hydrogen atoms were removed for clarity.

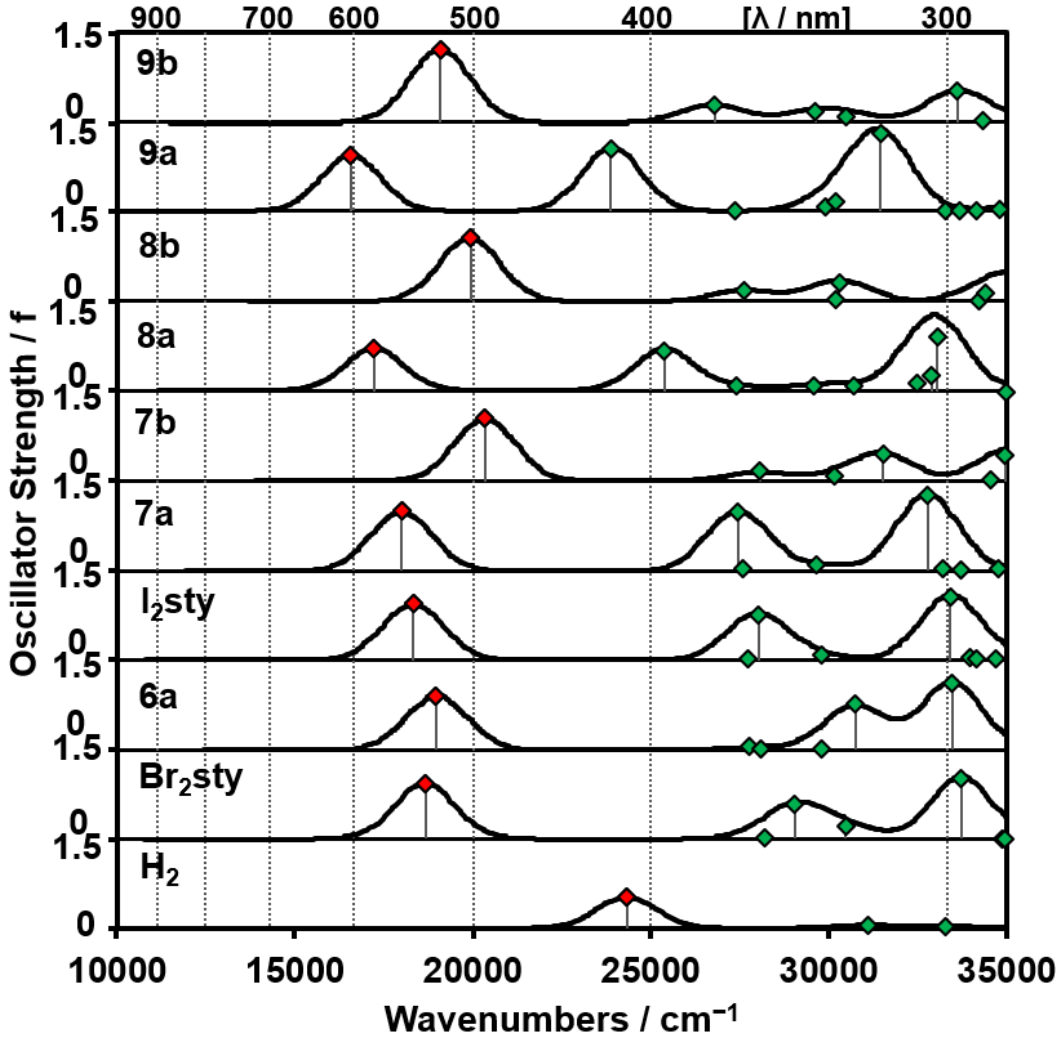

Figure 6.7 The calculated spectra of BODIPY dyes with a π-conjugation system that is extended at the CAM-B3LYP/SDD level of theory. Chemcraft was used to generate the simulated spectra at 2000 cm^{-1} bandwidth. The red diamonds represent the main absorption band. Details of the spectra are provided in **Table 8.1**.

6.3 Molecular modelling of porphyrins

Gaussian 09 software was used to carry out the DFT and TD-DFT calculations (**Figures 6.8**, **6.9, 6.10**, and **6.11**) for the **10** and **11** series of porphyrins and Sn(IV) tetraphenylporphyrin (**SnTPP**) and Sn(IV) tetrapyridylporphyrin (**SnTPyP**) model complexes with hydroxyl axial ligands. The *x*-axis inner-NH tautomer of **11a** is predicted to be −1.7 kCal/mol more stable than the *y*-axis tautomer, so this structure

of **11a** was used for this chapter. Michl's perimeter was used as a conceptual framework.[121] The four frontiers π-MOs derived from the HOMO and LUMO of a parent $C_{16}H_{16}^{2-}$ perimeter are termed **a**, **s**, **-a,** and **-s**, respectively.[184] The naming is dependent on whether a nodal plane (**a** and **-a**) or atoms with significant MO coefficients (**s**, -s) are aligned with the *y*-axis. The energy gap between the **a** and **s** MOs is called the ΔHOMO value, while that between the **-a** and **-s** MOs is referred to as the ΔLUMO value.[133]

Figure 6.10 (a) shows the frontier MO energies of the porphyrin **10** series. Upon substitution at the *meso*-pyridyl nitrogens of **SnTPyP**, where there are small MO coefficients (**Figure 6.8**), there is a stabilisation of the **a**, **s**, **-a,** and **-s,** MOs due to the inductive effect of the added hydrocarbon chains. This has only a minor effect on an average HOMO−LUMO gap value calculated from the energies of the **a**, **s**, **-a,** and **-s** MOs, which ignores MOs that are localised on the peripheral cationic substituents that do not have a significant impact on the Q and B bands. The **a**, **s**, **-a,** and **-s** MOs of the metalated **10d** complex are stabilised relative to those of the free base **10c** in **Figure 6.10**, but the ΔHOMO and ΔLUMO remain small in each case, so only minor changes are predicted in the average HOMO−LUMO gap. Large apparent shifts of the B bands of **11a-c** are predicted in the TD-DFT spectra (**Figure 6.11** (a)) that are not observed experimentally. This is probably due to problems related to how the calculations predict configurational interaction between the B excited state and other higher energy states associated with MOs introduced by the peripheral and axial substituents. This is particularly evident in the calculated spectrum of **11c**, where the most intense band in the B band region

The MO energies of the porphyrin **11** series were also examined. Upon extension of the π-system at the β-position of **SnTPP**, the **s** and **-a** MOs of **11a** are destabilised to

a minor extent relative to the **a** and **-s** MOs (**Figures 6.8**, **6.9**, and **6.10**) since they contain larger MO coefficients at the β position (**Figures 6.8** and **6.9)**. The **a**, **s**, **-a,** and **-s** MOs are stabilised when the central metal and axial ligands were added on **11b** and **11c**, respectively, but the ΔHOMO and ΔLUMO values remain relatively small, and there are only small differences predicted in the average HOMO−LUMO gaps of **11a-c** (**Figure 6.10** (b)). The calculated TD-DFT spectra (**Figure 6.11** (b)) are not in close agreement with the experimental spectra because the Q-bands in the experimental results are not as intense relative to the B band as those in the predicted theoretical calculations. The effect of an intruding pyridylvinylene MO (py) on the Q band region is not successfully predicted by the TD-DFT calculations (**Figure 6.10** (b)). As described in Chapter 3, the presence of the py MO means that the MCD sign sequences in the Q band region will no longer be related to the relative magnitudes of the ΔHOMO and ΔLUMO values.

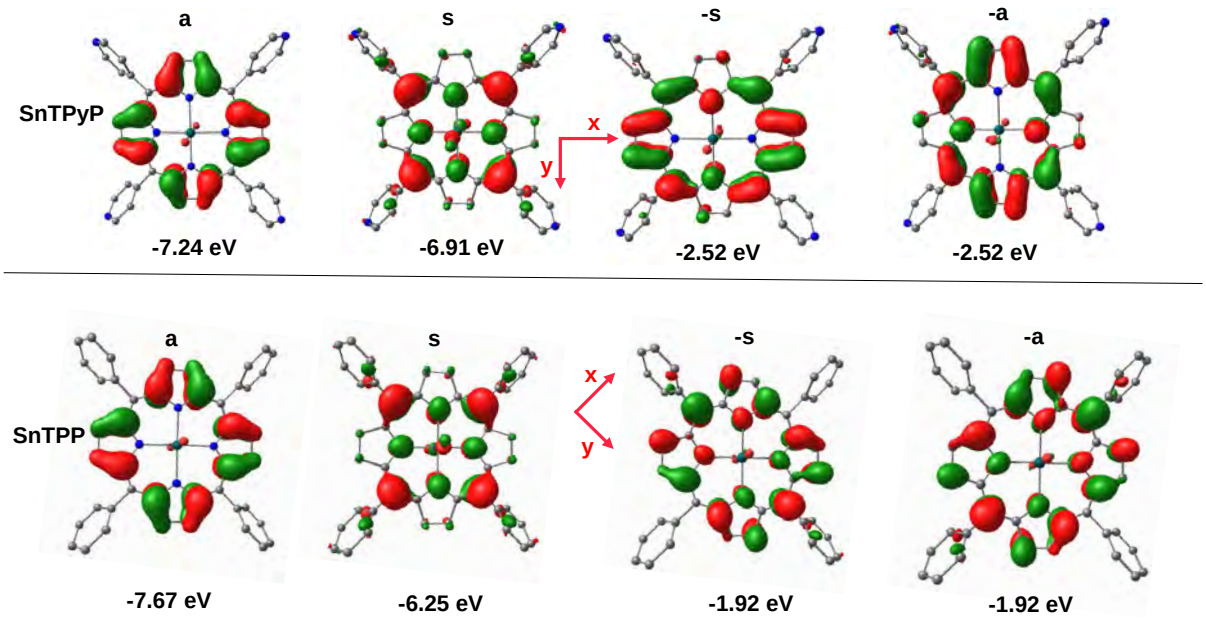

Figure 6.8 Angular nodal patterns and energies of the **a**, **s**, **-a**, and **-s** MOs of **SnTPP** and **SnTPyP**. Hydrogen atoms were removed for clarity, and the isosurface value was 0.03 a.u.

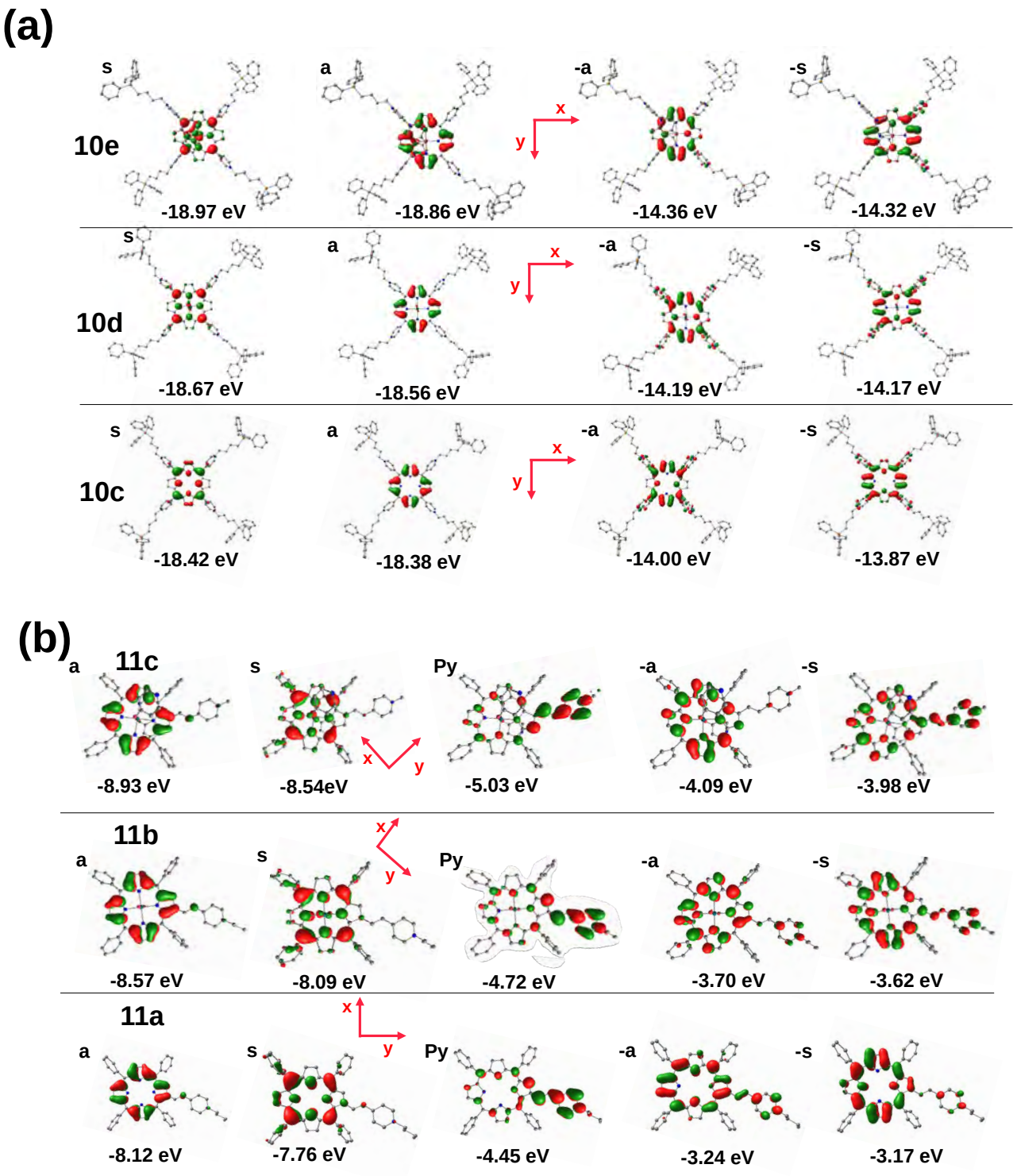

Figure 6.9 Angular nodal patterns and energies of the **a**, **s**, **-a,** and **-s** MOs of the porphyrin (a) **10** and (b) **11** series, and an intruding pyridylvinylene MO (py) that is introduced to the structures of **11a-c** as a result of the substitution at the β-position. The Hydrogen atoms were removed for picture quality purposes. The isosurface value was 0.03 a.u.

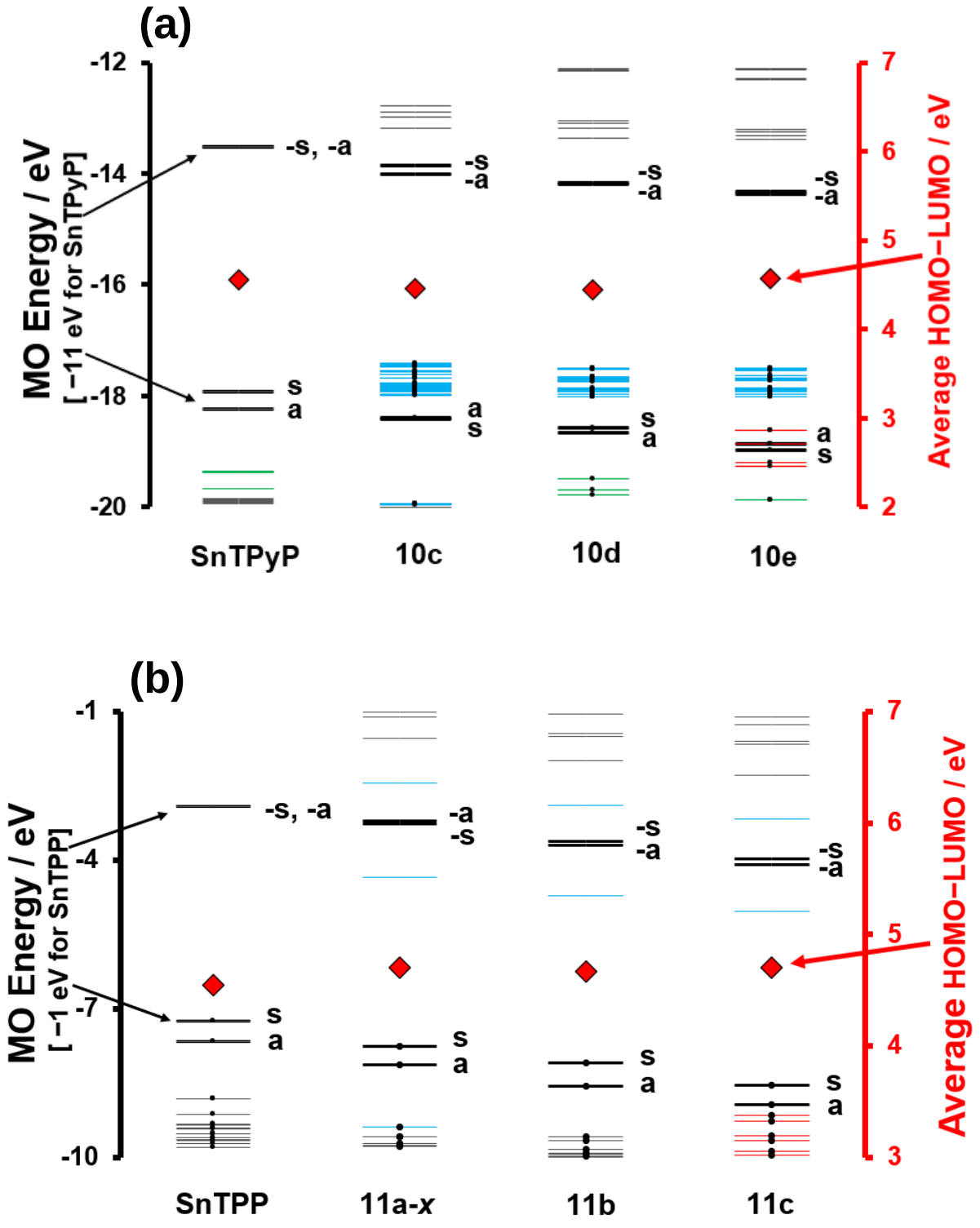

Figure 6.10 MO energies of the porphyrin (a) **10** and (b) **11** series at the CAM-B3LYP level of theory. The red diamonds plotted against the secondary axis denote the HOMO−LUMO band gap values. Occupied MOs are highlighted with black circles, while black rods denote the **a**, **s**, **-a** and **-s** MOs. The blue, red, and green lines in (a)

represent MOs arising from the peripheral groups on the *meso*-carbons, the axial ligands, and axial oxygen lone pairs, respectively. The blue lines in (b) denote MOs arising from the porphyrin being β-substituted, while the red lines are MOs arising from the addition of axial on the porphyrin. **SnTPP** denotes tin tetraphenyl porphyrin, and **SnTPyP** is tin tetrapyridyl porphyrin.

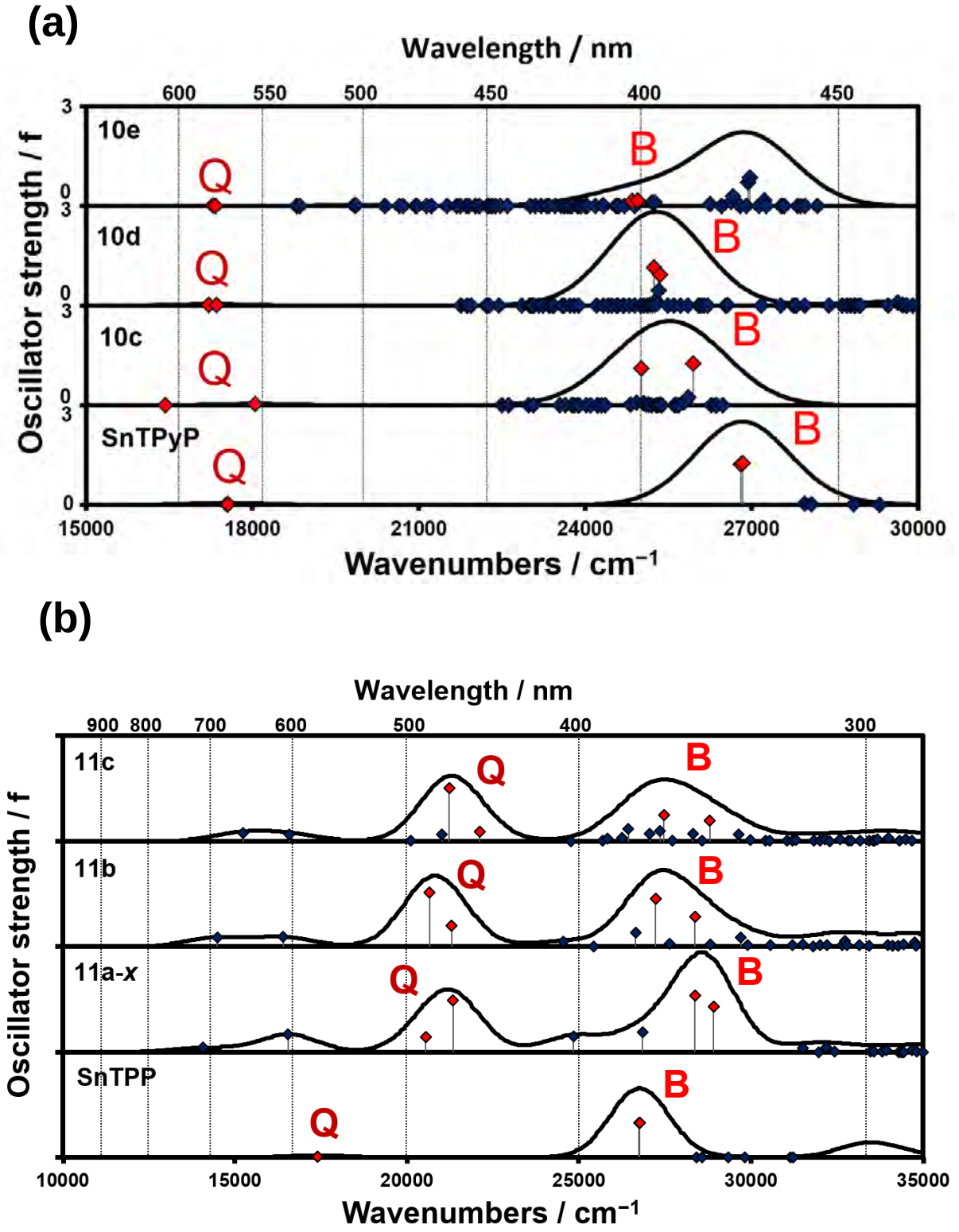

Figure 6.11 Spectral shifts of BODIPY dyes as per TD-DFT calculations of the (a) **10** series and (b) **11** series of porphyrins. Chemcraft was used to generate the simulated spectra at 2000 cm^{-1} bandwidth. Red diamonds highlight the Q and B absorption band. Details of the spectra are given in **Table 8.1**.

6.4 Concluding remarks

Key trends in the spectral properties and MO energies of the BODIPY dyes and porphyrins that were selected for study were investigated using TD-DFT calculations and the CAM-B3LYP functional. The π-extended BODIPY dyes exhibited a narrow HOMO−LUMO gap compared to core dyes. The calculations predicted highly red-shifted main spectral bands for halogenated di-substituted dyes so that they lie well within the therapeutic window. The TD-DFT calculations for porphyrins were problematic and did not successfully predict the trends observed in the experimental spectra. They demonstrated, however, that the Q and B bands remain the dominant transitions in the context of the porphyrin **10** series and that the presence of an intruding MO localised on the pyridylvinylene group close in energy to the **-a** and **-s** MOs of the porphyrin **11** series accounts for the anomalous MCD sign sequences reported in Chapter 3.

Chapter Seven

Conclusion

7. Conclusion

The main aim of this work was to synthesise and characterise a series of structurally modified novel BODIPY dyes and porphyrins that are suitable for use as photosensitiser dyes in PDT and PACT. The target structures for the BODIPY dyes were selected to have hydrogen bond accepting properties to enhance their solubility in aqueous solutions. On the other hand, the porphyrin target structures have cationic properties to achieve this.

The novel BODIPY dyes **6a**, **6b**, **7a**, **7b**, **8a**, **8b,** and **9a**, **9b** were synthesised using an acid-catalysed condensation, electrophilic substitution, and Knoevenagel condensation reactions. The dyes have moderately high singlet oxygen quantum yields. **7b** was found to have the highest singlet oxygen value of 0.55 among the styrylated BODIPY dyes. The main spectral bands of the dyes lie in the therapeutic window, and the dyes were found to be photostable upon exposure to UV-visible light.

When the cytotoxicities of BODIPY dyes **6** and **9** were compared, **6** was found to have more desirable photosensitizing properties because of its minimal dark toxicity and more desirable IC_{50} values upon illumination. Additionally, **6** had higher photo index values than **9**. This is an indication of better photocytotoxicity. Furthermore, when **9a** and **9b** anticancer activities were compared, **9b** was found to have more desirable antitumor properties.

Similarly, the anticancer properties of BODIPY series **7** and **8** were compared, and **7** were found to be the better PS dyes than **8** because of their lower IC_{50} values and minimal dark cytotoxicity. However, **8** had higher phototoxicity index values than **7** due to their low dark toxicity. Likewise, a comparison between **7a** and **7b** was carried out, and the mono-styryl **7b** dye was found to have better PDT activity properties than **7a**.

This was attributed to its enhanced ability to generate singlet oxygen. The same trend was observed when **8a** was compared to **8b**. However, when the dyes were used as a PS during PACT studies, they showed no activity. BODIPYs **2** and **5** were not used in bioassays because they had negligible singlet oxygen quantum yields.

On the other hand, the porphyrin target structures have cationic properties. Tetrapyridinyl porphyrin conjugated with triphenylphosphine (TPP) was synthesised, while the other series contained a substituent at the β-position. The porphyrins were metallated with Sn(IV) to enhance singlet oxygen generation and introduce axial ligands that can reduce aggregation. The porphyrin **10** series were found to have better cytotoxic properties and higher PI values due to their mitochondria targeting abilities. Since mitochondria are the powerhouse of the cell, destroying these organelles results in cell death. Additionally, the porphyrin **11** series also exhibited impressive PACT activity. **11c** exhibited the greatest antimicrobial activity due to the presence of axial ligands.

Furthermore, we conducted docking studies to evaluate their binding efficiency to human serum albumin (HSA), a transport protein in the body. Without the ability of the PS to bind to HSA, their bioavailability will be reduced, and consequently, its efficacy will also be reduced due to less photosensitiser reaching the active site. In this work, the mono-styrylated BODIPY dyes had better binding energies than the rest of the molecules. Thus, they will have better bioavailability during *in vivo studies*.

In conclusion, mitochondria-targeting photosensitisers had better cytotoxic properties than the BODIPY dyes that primarily localise in other organelles for two reasons. Firstly, the mitochondria will still contain high oxygen concentrations under hypoxic conditions. Secondly, this organelle is involved in regulating apoptotic death.

Nevertheless, there is still more work to be carried out in exploiting structure modifications on porphyrins and their analogues. To be specific, the following modifications are recommended:

I. To synthesise mono-substituted triphenylphosphine porphyrins to reduce the molecular weight of the compound that may inhibit its cellular uptake during *in vivo* studies.
II. To synthesise β-substituted mitochondria targeting porphyrins and study their photochemical studies.
III. To synthesise metallated BODIPY dyes and compare their cytotoxicity to brominated or iodinated dyes.
IV. To synthesise BODIPY dyes with chelated BF_2 centres in order to explore their photochemical and anticancer activities.
V. To synthesise mono-substituted BODPY dyes that absorb deep into the therapeutic window.

8. Appendix

Table 8.1 The calculated UV-visible absorption spectra of the B3LYP optimised geometries of the porphyrins

#[a]		λ_{cal}[b]	λ_{exp}[c]	f[d]	Wavefunction =[e]
					SnTPyP
1,2	Q	570	-	0.02	**61% s→-a/-s; 38% a→-a/-s;** …
3,4	B	373	-	1.23	**59% a→-a/-s; 35% s→-a/-s; …**
					10a
1	Q	608	657	0.0001	**49% s→-a; 47% a→-s**; …
2	Q	554	-	0.03	**54% a→-s; 43% s→-s**; …
20	B	400	427	1.10	**36% a→-s; 36% s→-s**; …
34	B	385	427	1.02	**41% 3→-s; 35% a→-a**; 14% H−19→-a; …
					10b
1	Q	581	640	0.02	**54% s→-a; 41% a→-s**; …
2	Q	576	640	0.02	**53% s→-s; 43% a→-a**; …
42	B	396	427	1.14	**42% a→-s; 33% s→-a**; …
47	B	395	427	0.94	**33% a→-a; 27% s→-s;** 25% H−19→-s; …
					10c
1	Q	578	634	0.01	40% H−24^{Opy}→-a; **34% a→-s; 18% s→-a;** …
2	Q	577	634	0.006	39% H−24^{Opy}→-s; **36% a→-a; 18% s→-s;** …
58	B	402	424	0.15	35% H−31^{Opy}→-a/-s; 31% H−30^{Opy}→-s; **17% a→-a/-s; 8% s→-a/-s;** …
60	B	401	424	0.16	42% H−31^{Opy}→-a/-s; 24% H−30^{Opy}→s; **19% a→-a/-s; 10% s→-a/-s;** …
69	-	371	-	0.72	30% H−31^{Opy}→-a/-s; 21% H−33^{Opy}→-s; **20% s→-a/-s; 8% a→-a/-s**; …
70	-	370	-	0.86	32% H−31^{Opy}→-a/-s; **23% s→-a/-s;** 13% H−32^{Opy}→s; **12% a→-a/-s;** …
					SnTPP
1,2	Q	575	-	0.04	**64% s→-a/-s; 35% a→-a/-s;** …
3,4	B	374	-	1.31	**62% a→-a/-s; 31% s→-a/-s;** …
					11a
1	Py	710	-	0.09	78% s→py; **10% a→-a; …**
2	Py	604	-	0.34	69% a→py; **17% s→-a; …**
3	Q	486	651	0.29	**50% s→-s; 22% a→-a;** 17% s→py; …
4	Q	468	651	0.99	**50% s→-a; 18% a→-s;** 16% a→py; …
7	B	352	425	1.06	**21% a→-s; 16% a→-a;** 14% H−3→py; **14% s→s; 13% s→a;** …
8	B	345	425	0.87	**34% a→-s; 17% s→-a; 16% a→-a;** 11% H−2→py; **11% s→-a;** …
					11b
1	Py	691	-	0.17	82% s→py; …
2	Py	609	-	0.18	55% a→py; **24% s→-a;** …
3	Q	484	640	1.02	**46% s→-a;** 18% a→py; **11% a→-s;** …
4	Q	469	640	0.40	**48% s→-s; 19% a→-a;** 17% a→py; …
8	B	367	427	0.91	**41% a→-a; 24% s→-s; 13% a→-s;** …
10	B	352	427	0.57	**41% a→-s; 15% s→-a**; …
					11c
1	Py	657	-	0.16	78% s→py; **12% a→-a; …**
2	Py	602	-	0.13	53% a→py; **31% s→-a; 11% a→-s;** …
5	Q	471	619	1.00	**35% s→-a;** 19% a→py; **11% a→-a;** …
6	Q	452	619	0.19	**34% s→-s; 17% a→-a;** 15% a→py; 11% a→py; 10% H−3→py; …

14	B	364	429	0.50	**28% a→-a; 23% s→-s;** 11% H−10→py; …
18	B	347	429	0.38	**35% a→-s; 13% s→-a;** 12% H−10→py; …

[a]The number of states assigned in terms of increasing energy within the TD-DFT calculation. [b]Calculated wavelengths in nm.[c]Experimental wavelengths in nm, recorded in **Table 3.1** [d]Calculated oscillator strengths. [e]Wavefunctions derived from the eigenvectors predicted by TD-DFT. Only one-electron contributions of more than 10% are included. **a**, **s, -a**, and **-s** refer to the MO nomenclature of Michl's perimeter model,[121] while **py** refers to a frontier MO associated with β-substitution. Opy as a superscript refers to MOs localised on pyridyloxy axial ligands. One-electron transitions between the **a**, **s, -a**, and **-s** MOs are highlighted in bold.

Table 8.2 The calculated UV-visible absorption spectra of the B3LYP optimised geometries of the BODIPY dyes.

#[a]	λ_{exp}[b]	λ_{cal}[c]	f[d]	Wavefunction =[e]
				H_2
1	-	411	0.54	**97% H→L**; …
				1
1	501	412	0.53	**97% H→L**; …
				2
5	541	452	0.39	**97% H→L**; …
				Br_2
1	-	429	0.60	**97% H→L**; …
				3
1	530	430	0.60	**97% H→L**; …
				5
5	555	458	0.46	**95% H→L**; …
				I_2
1	-	431	0.68	**97% H→L**; …
				4
1	542	430	0.68	**97% H→L**; …
				Br_2Sty
1	-	536	0.92	**97% H→L**; …
				6a
1	630	527	0.90	**97% H→L**; …
				I_2Sty
1	-	546	0.94	**97% H→L**; …
				7a
1	668	556	0.98	**96% H→L**; …
				7b
1	600	492	1.03	**95% H→L**; …
				8a
1	693	581	0.70	**95% H→L**; …
				8b
1	619	502	1.06	**93% H→L**; …
				9a

1	714	604	0.93	**100% H→L**; …
			9b	
1	616	524	1.22	**99% H→L**; …

[a]The number of the state assigned in terms of increasing energy within the TD-DFT calculation. [b]Calculated wavelengths in nm. [c]Experimental wavelengths in nm, recorded in **Table 3.1** [d]Calculated oscillator strengths. [e]Wavefunctions derived from the eigenvectors predicted by TD-DFT. Only one-electron contributions of more than 10% are included. H and L refer to the HOMO and LUMO. The H→L one-electron transition is highlighted in bold.

9. References

(1) Bray, F.; Laversanne, M.; Weiderpass, E.; Soerjomataram, I. The Ever-Increasing Importance of Cancer as a Leading Cause of Premature Death Worldwide. *Cancer* **2021**, *127* (16), 3029–3030.

(2) Cancer https://www.who.int/news-room/fact-sheets/detail/cancer (accessed May 14, 2022).

(3) Understanding What Cancer Is: Ancient Times to Present https://www.cancer.org/treatment/understanding-your-diagnosis/history-of-cancer/what-is-cancer.html (accessed May 14, 2022).

(4) Cancer History https://www.news-medical.net/health/Cancer-History.aspx (accessed May 14, 2022).

(5) Sung, H.; Ferlay, J.; Siegel, R. L.; Laversanne, M.; Soerjomataram, I.; Jemal, A.; Bray, F. Global Cancer Statistics 2020: GLOBOCAN Estimates of Incidence and Mortality Worldwide for 36 Cancers in 185 Countries. *CA: A Cancer Journal for Clinicians* **2021**, *71* (3), 209–249.

(6) https://www.cancer.org/about-us/our-global-health-work/global-cancer-burden.html (accessed May 14, 2022).

(7) https://www.cancer.gov/about-cancer/causes-prevention/risk/age (Accessed May14, 2022).

(8) Bukhtoyarov, O.; Samarin, D.; Bukhtoyarov, O. V; Samarin, D. M. An Overview on Pathogenesis of Cancer: Cancer Reparative Trap. *Journal of Cancer Therapy* **2015**, *6* (234), 399–412.

(9) Imran, A.; Qamar, H. Y.; Ali, Q.; Naeem, H.; Riaz, M.; Amin, S.; Kanwal, N.; Ali, F.; Sabar, M. F.; Nasir, I. A. Role of Molecular Biology in Cancer Treatment: A Review Article. *Iran. J. Public Health* **2017**, *46* (11), 1475−1485.

(10) Blackadar, C. B. Historical Review of the Causes of Cancer. *World J. Clin. Oncol.* **2016**, *7* (1), 54−86.

(11) Imran, M.; Paudel, K. R.; Jha, S. K.; Hansbro, P. M.; Dua, K.; Mohammed, Y. Dressing of Multifunctional Nanoparticles with Natural Cell-Derived Membranes for the Superior Chemotherapy. *Nanomedicine* **2022**, *3* (6), 1002–1023.

(12) Yang, Y.; Zheng, X.; Chen, L.; Gong, X.; Yang, H.; Duan, X.; Zhu, Y. Multifunctional Gold Nanoparticles in Cancer Diagnosis and Treatment. *Int. J. Nanomedicine* **2022**, *17*, 2041–2067.

(13) Yan, Y.; Kumar, A. B.; Finnes, H.; Markovic, S. N.; Park, S.; Dronca, R. S.; Dong, H. Combining Immune Checkpoint Inhibitors With Conventional Cancer Therapy. *Front. Immunol.* **2018**, *9* (1739), 1–13.

(14) Qiao, J.; Liu, Z.; Fu, Y. X. Adapting Conventional Cancer Treatment for Immunotherapy. *J. Mol. Med.* **2016**, *94* (5), 489–495.

(15) Klerk, D. J. de; Keijzer, M. J. de; Dias, L. M.; Heemskerk, J.; Haan, L. R. de; Kleijn, T. G.; Franchi, L. P.; Heger, M. Strategies for Improving Photodynamic Therapy Through Pharmacological Modulation of the Immediate Early Stress Response. *Methods Mol Biol.* **2022**, *6* (3), 405–480.

(16) Nakandi, K.; Stub, T.; Kristoffersen, A. E. Cancer-Related Correlates of Traditional and Complementary Medicine Use among Norwegian Cancer Survivors: A Cross-Sectional Study. *Research square* **2022**, *63* (4), 1–35.

(17) Mundy, E. A.; Blanchard, E. B.; Cirenza, E.; Gargiulo, J.; Maloy, B.; Blanchard, C. G. Posttraumatic Stress Disorder in Breast Cancer Patients Following Autologous Bone Marrow Transplantation or Conventional Cancer Treatments. *Behav. Res. Ther.* **2000**, *38* (10), 1015–1027.

(18) García-Fernández, C.; Saz, A.; Fornaguera, C.; Borrós, S. Cancer Immunotherapies Revisited: State of the Art of Conventional Treatments and next-Generation Nanomedicines. *Cancer Gene Ther. 2021 289* **2021**, *28* (9), 935–946.

(19) Gotwals, P.; Cameron, S.; Cipolletta, D.; Cremasco, V.; Crystal, A.; Hewes, B.; Mueller, B.; Quaratino, S.; Sabatos-Peyton, C.; Petruzzelli, L.; Engelman, J. A.; Dranoff, G. Prospects for Combining Targeted and Conventional Cancer Therapy with Immunotherapy. *Nat. Rev. Cancer* **2017**, *17* (5), 286–301.

(20) Robertson, C. A.; Evans, D. H.; Abrahamse, H. Photodynamic Therapy (PDT): A Short Review on Cellular Mechanisms and Cancer Research Applications for PDT. *J. Photochem. Photobiol. B Biol.* **2009**, *96* (1), 1–8.

(21) Allison, R. R.; Sibata, C. H. Oncologic Photodynamic Therapy Photosensitizers: A Clinical Review. *Photodiagnosis Photodyn. Ther.* **2010**, *7* (2), 61–75.

(22) Yanovsky, R. L.; Bartenstein, D. W.; Rogers, G. S.; Isakoff, S. J.; Chen, S. T. Photodynamic Therapy for Solid Tumors: A Review of the Literature. *Photodermatol. Photoimmunol. Photomed.* **2019**, *35* (5), 295–303.

(23) Ang, J. M.; Riaz, I. Bin; Kamal, M. U.; Paragh, G.; Zeitouni, N. C. Photodynamic Therapy and Pain: A Systematic Review. *Photodiagnosis Photodyn. Ther.* **2017**, *19*, 308–344.

(24) Cesar Trindade, A.; Antônio Poli De Figueiredo, J.; Steier, L.; Batista Blessmann Weber, J. Photodynamic Therapy in Endodontics: A Literature Review. *Photomed. Laser Surg.* **2015**, *33* (3), 10–25.

(25) Lim, C.M. and Gordon, L. Photodynamic therapy: A targeted literature review focussing on outcomes and optimisation in solid organ transplant recipients. *Australas J Dermatol.* **2019**, 60 (10), 273–277.

(26) Dos Santos, A. F.; De Almeida, D. R. Q.; Terra, L. F.; Baptista, M. S.; Labriola, L. Photodynamic Therapy in Cancer Treatment - an Update Review. *J. Cancer Metastasis Treat.* **2019**, *5* (25), 1-20.

(27) Dolmans, D. E. J. G. J.; Fukumura, D.; Jain, R. K. Photodynamic Therapy for Cancer. *Nat. Rev. Cancer* **2003**, *3* (5), 380–387.

(28) Donnelly, R. F.; McCarron, P. A.; Tunney, M. M. Antifungal Photodynamic Therapy. *Microbiol. Res.* **2008**, *163* (1), 1–12.

(29) Correia, J. H.; Rodrigues, J. A.; Pimenta, S.; Dong, T.; Yang, Z. Photodynamic Therapy Review: Principles, Photosensitizers, Applications, and Future Directions. *Pharmaceutics* **2021**, *13* (1332), 1–16.

(30) Honors, C. N.; Kruger, C. A.; Abrahamse, H. Photodynamic Therapy for Metastatic Melanoma Treatment: A Review. *Technol. Cancer Res. Treat.* **2018**, *17* (4), 1–15.

(31) Ma, J.; Jiang, L. Photogeneration of Singlet Oxygen ($^1O_2$) and Free Radicals ($Sen^{\cdot -}$, $O^{\cdot -2}$) by Tetra-Brominated Hypocrellin B Derivative. *Free Radical Research* **2009**, *35* (6), 767–777.

(32) Castano, A. P.; Demidova, T. N.; Hamblin, M. R. Mechanisms in Photodynamic

Therapy: Part One—Photosensitizers, Photochemistry and Cellular Localization. *Photodiagnosis Photodyn. Ther.* **2004**, *1* (4), 279–293.

(33) Plaetzer, K.; Krammer, B.; Berlanda, J.; Berr, F.; Kiesslich, T. Photophysics and Photochemistry of Photodynamic Therapy: Fundamental Aspects. *Lasers Med. Sci.* **2009**, *24* (2), 259–268.

(34) Karotki, A.; Kruk, M.; Drobizhev, M.; Rebane, A.; Nickel, E.; Spangler, C. W. Efficient Singlet Oxygen Generation upon Two-Photon Excitation of New Porphyrin with Enhanced Nonlinear Absorption. *IEEE J. Sel. Top. Quantum Electron.* **2001**, *7* (6), 971–975.

(35) Kenneth R. W.; Gomer, C. J.; Dougherty, T. J. Identification of Singlet Oxygen as the Cytotoxic Agent in Photo-Inactivation of a Murine Tumor. *Cancer Res.* **1976**, *36* (1), 2326–2329.

(36) Valenzeno, D. P. Photomodification of biological membranes with emphasis on singlet oxygen mechanisms. *Photochem. Photobiol.* **1987**, *46* (1), 147–160.

(37) Sharman, W. M.; Allen, C. M.; Van Lier, J. E. [35] Role of Activated Oxygen Species in Photodynamic Therapy. *Methods Enzymol.* **2000**, *319 (52)*, 376–400.

(38) Bergamini, C.; Gambetti, S.; Dondi, A.; Cervellati, C. Oxygen, Reactive Oxygen Species and Tissue Damage. *Curr. Pharm. Des.* **2004**, *10* (14), 1611–1626.

(39) Baptista, M. S.; Cadet, J.; Di Mascio, P.; Ghogare, A. A.; Greer, A.; Hamblin, M. R.; Lorente, C.; Nunez, S. C.; Ribeiro, M. S.; Thomas, A. H.; Vignoni, M.; Yoshimura, T. M. Type I and Type II Photosensitized Oxidation Reactions: Guidelines and Mechanistic Pathways. *Photochem. Photobiol.* **2017**, *93* (4), 912–919.

(40) Foote, C. S. Definition of Type I and Type II photosensitized oxidation. *Photochem. Photobiol.* **1991**, *54* (5), 659–659.

(41) Ochsner, M. Photophysical and Photobiological Processes in the Photodynamic Therapy of Tumours. *J. Photochem. Photobiol. B Biol.* **1997**, *39* (1), 1–18.

(42) Mroz, P.; Xia, Y.; Asanuma, D.; Konopko, A.; Zhiyentayev, T.; Huang, Y. Y.; Sharma, S. K.; Dai, T.; Khan, U. J.; Wharton, T.; Hamblin, M. R. Intraperitoneal Photodynamic Therapy Mediated by a Fullerene in a Mouse Model of Abdominal Dissemination of Colon Adenocarcinoma. *Nanomed.: Nanotechnol. Biol. Med.* **2011**, *7* (6), 965–974.

(43) Mroz, P.; Tegos, G. P.; Gali, H.; Wharton, T.; Sarna, T.; Hamblin, M. R. Photodynamic Therapy with Fullerenes. *Photochem. Photobiol. Sci. 2007 611* **2007**, *6* (11), 1139–1149.

(44) Dehaven, B. A.; Liberatore, H. K.; Greer, A.; Richardson, S. D.; Shimizu, L. S. Probing the Formation of Reactive Oxygen Species by a Porous Self-Assembled Benzophenone Bis-Urea Host. *ACS Omega* **2019**, *4* (5), 8290–8298.

(45) Davila, J.; Harriman, A. Photosensitized oxidation of biomaterials and related model compounds. *Photochem. Photobiol.* **1989**, *50* (1), 29–35.

(46) Zhuang, Z.; Dai, J.; Yu, M.; Li, J.; Shen, P.; Hu, R.; Lou, X.; Zhao, Z.; Tang, B. Z. Type I Photosensitizers Based on Phosphindole Oxide for Photodynamic Therapy: Apoptosis and Autophagy Induced by Endoplasmic Reticulum Stress. *Chem. Sci.* **2020**, *11* (13), 3405–3417.

(47) Lee, C.-N.; Hsu, R.; Chen, H.; Wong, T.-W.; Amparo, M.; Faustino, F.; Monteiro, C. J. P.; Ramos, C. I. V. Daylight Photodynamic Therapy: An Update. *Molecules*

2020, *25* (5195), 1–16.

(48) Bacellar, I. O. L.; Tsubone, T. M.; Pavani, C.; Baptista, M. S. Photodynamic Efficiency: From Molecular Photochemistry to Cell Death. *Int. J. Mol. Sci.* **2015**, *16* (9), 20523–20559.

(49) Foote, C. S. Mechanisms of Photosensitized Oxidation. *Science.* **1968**, *162* (3857), 963–970.

(50) Mroz, P.; Hashmi, J. T.; Huang, Y. Y.; Lange, N.; Hamblin, M. R. Stimulation of Anti-Tumor Immunity by Photodynamic Therapy. *Expert Rev. Clin. Immunol.* **2014**, *7* (1), 75–91.

(51) Castano, A. P.; Mroz, P.; Hamblin, M. R. Photodynamic Therapy and Anti-Tumour Immunity. *Nat. Rev. Cancer* **2006**, *67* (7), 535–545.

(52) http://photobiology.info/Uzdensky.html (accessed May 14, 2022).

(53) Casas, A.; Di Venosa, G.; Hasan, T.; Batlle, A. Mechanisms of Resistance to Photodynamic Therapy. *Curr. Med. Chem.* **2011**, *18* (16), 2486–2515.

(54) Allison, R. R.; Moghissi, K. Photodynamic Therapy (PDT): PDT Mechanisms. *Clin. Endosc.* **2013**, *46* (1), 24–29.

(55) Rocha G. L. B. Development of a Novel Photosensitizer for Photodynamic Therapy of Cancer, PhD, thesis, University of Coimbra, Lisbon, Portugal **2016**.

(56) Dewaele, M.; Maes, H.; Agostinis, P. ROS-Mediated Mechanisms of Autophagy Stimulation and Their Relevance in Cancer Therapy. *Autophagy* **2010**, *6* (7), 838–854.

(57) Reiners, J. J.; Agostinis, P.; Berg, K.; Oleinick, N. L.; Kessel, D. Assessing

Autophagy in the Context of Photodynamic Therapy. *Autophagy* **2010**, *6* (1), 7–18.

(58) Reiners, J. J.; Caruso, J. A.; Mathieu, P.; Chelladurai, B.; Yin, X. M.; Kessel, D. Release of Cytochrome c and Activation of Pro-Caspase-9 Following Lysosomal Photodamage Involves Bid Cleavage. *Cell Death Differ.* **2002**, *9* (9), 934–944.

(59) Xue, L. Y.; Chiu, S. M.; Oleinick, N. L. Photochemical Destruction of the Bcl-2 Oncoprotein during Photodynamic Therapy with the Phthalocyanine Photosensitizer Pc 4. *Oncogene* **2001**, *20* (26), 3420–3427.

(60) Usuda, J.; Chiu, S. M.; Murphy, E. S.; Lam, M.; Nieminen, A. L.; Oleinick, N. L. Domain-Dependent Photodamage to Bcl-2: a membrane anchorage region is needed to form the target of phthalocyanine photosensitization. *J. Biol. Chem.* **2003**, *278* (3), 2021–2029.

(61) Kessel, D.; Castelli, M. Evidence That Bcl-2 Is the Target of Three Photosensitizers That Induce a Rapid Apoptotic Response. *Photochem. Photobiol.* **2001**, *74* (2), 318–322.

(62) Agostinis, P.; Berg, K.; Cengel, K. A.; Foster, T. H.; Girotti, A. W.; Gollnick, S. O.; Hahn, S. M.; Hamblin, M. R.; Juzeniene, A.; Kessel, D.; Korbelik, M.; Moan, J.; Mroz, P.; Nowis, D.; Piette, J.; Wilson, B. C.; Golab, J. Photodynamic Therapy of Cancer: An Update. *CA. Cancer J. Clin.* **2011**, *61* (4), 250–281.

(63) Banfi, S.; Caruso, E.; Zaza, S.; Mancini, M.; Gariboldi, M. B.; Monti, E. Synthesis and Photodynamic Activity of a Panel of BODIPY Dyes. *J. Photochem. Photobiol. B Biol.* **2012**, *114*, 52–60.

(64) Hu, W.; Ma, H.; Hou, B.; Zhao, H.; Ji, Y.; Jiang, R.; Hu, X.; Lu, X.; Zhang, L.;

Tang, Y.; Fan, Q.; Huang, W. Engineering Lysosome-Targeting BODIPY Nanoparticles for Photoacoustic Imaging and Photodynamic Therapy under Near-Infrared Light. *ACS Appl. Mater. Interfaces* **2016**, *8* (19), 12039–12047.

(65) Liu, Y.; Li, Z.; Chen, L.; Xie, Z. Near Infrared BODIPY-Platinum Conjugates for Imaging, Photodynamic Therapy and Chemotherapy. *Dyes Pigm.* **2017**, *141*, 5–12.

(66) Li, M.; Tian, R.; Fan, J.; Du, J.; Long, S.; Peng, X. A Lysosome-Targeted BODIPY as Potential NIR Photosensitizer for Photodynamic Therapy. *Dye. Pigm.* **2017**, *147*, 99–105.

(67) Nguyen, V.-N.; Yim, Y.; Kim, S.; Ryu, B.; K Swamy, K. M.; Kim, G.; Kwon, N.; Kim, C.-Y.; Park, S.; Yoon, J.; Nguyen, V.; Yim, Y.; Kim, G.; Kwon, N.; Yoon, J.; Kim, S.; Park, S.; Ryu, B.; Kim, C. Y. Molecular Design of Highly Efficient Heavy-Atom-Free Triplet BODIPY Derivatives for Photodynamic Therapy and Bioimaging. *Angew. Chemie Int. Ed.* **2020**, *59* (23), 8957–8962.

(68) Üçüncü, M.; Karakuş, E.; Kurulgan Demirci, E.; Sayar, M.; Dartar, S.; Emrullahoglu, M. BODIPY-Au(I): A Photosensitizer for Singlet Oxygen Generation and Photodynamic Therapy. *Org. Lett.* **2017**, *19* (10), 2522–2525.

(69) Wang, H.; Zhao, W.; Liu, X.; Wang, S.; Wang, Y. BODIPY-Based Fluorescent Surfactant for Cell Membrane Imaging and Photodynamic Therapy. *ACS Appl. Bio Mater.* **2020**, *3* (1), 593–601.

(70) Mai, D. K.; Kang, B.; Vales, T. P.; Badon, I. W.; Cho, S.; Lee, J.; Kim, E.; Kim, H. J. Synthesis and Photophysical Properties of Tumor-Targeted Water-Soluble BODIPY Photosensitizers for Photodynamic Therapy. *Molecules* **2020**, *25* (15), 1–16.

(71) Badon, I. W.; Kim, C.; Lim, J. M.; Mai, D. K.; Vales, T. P.; Kang, D.; Cho, S.; Lee, J.; Kim, H. J.; Yang, J. Mitochondrion-Targeting PEGylated BODIPY Dyes for near-Infrared Cell Imaging and Photodynamic Therapy. *J. Mater. Chem. B* **2022**, *10* (8), 1196–1209.

(72) Kubheka, G.; Uddin, I.; Amuhaya, E.; Mack, J.; Nyokong, T. Synthesis and Photophysicochemical Properties of BODIPY Dye Functionalized Gold Nanorods for Use in Antimicrobial Photodynamic Therapy. *J. Porphyr. Phthalocyanines* **2016**, *20* (8), 1016–1024.

(73) Zou, J.; Yin, Z.; Ding, K.; Tang, Q.; Li, J.; Si, W.; Shao, J.; Zhang, Q.; Huang, W.; Dong, X. BODIPY Derivatives for Photodynamic Therapy: Influence of Configuration versus Heavy Atom Effect. *ACS Appl. Mater. Interfaces* **2017**, *9* (38), 32475–32481.

(74) Awuah, S. G.; You, Y. Boron Dipyrromethene (BODIPY)-Based Photosensitizers for Photodynamic Therapy. *RSC Adv.* **2012**, *2* (30), 11169–11183.

(75) Turksoy, A.; Yildiz, D.; Akkaya, E. U. Photosensitization and Controlled Photosensitization with BODIPY Dyes. *Coord. Chem. Rev.* **2019**, *379*, 47–64.

(76) Zhang, W.; Ahmed, A.; Cong, H.; Wang, S.; Shen, Y.; Yu, B. Application of Multifunctional BODIPY in Photodynamic Therapy. *Dye. Pigm.* **2021**, *185* (108937), 1–14.

(77) Lincoln, R.; Durantini, A. M.; Greene, L. E.; Martínez, S. R.; Knox, R.; Becerra, M. C.; Cosa, G. Meso-Acetoxymethyl BODIPY Dyes for Photodynamic Therapy: Improved Photostability of Singlet Oxygen Photosensitizers. *Photochem. Photobiol. Sci.* **2020**, *16* (2), 178–184.

(78) Bassan, E.; Gualandi, A.; Cozzi, P. G.; Ceroni, P. Design of BODIPY Dyes as Triplet Photosensitizers: Electronic Properties Tailored for Solar Energy Conversion, Photoredox Catalysis and Photodynamic Therapy. *Chem. Sci.* **2021**, *12* (19), 6607–6628.

(79) Watley, R. L.; Awuah, S. G.; Bio, M.; Cantu, R.; Gobeze, H. B.; Nesterov, V. N.; Das, S. K.; D'Souza, F.; You, Y. Dual Functioning Thieno-Pyrrole Fused BODIPY Dyes for NIR Optical Imaging and Photodynamic Therapy: Singlet Oxygen Generation without Heavy Halogen Atom Assistance. *Chem. Asian J.* **2015**, *10* (6), 1335–1343.

(80) Fan, G.; Yang, L.; Chen, Z. Water-Soluble BODIPY and Aza-BODIPY Dyes: Synthetic Progress and Applications. *Front. Chem. Sci. Eng.* **2014**, *8* (4), 405–417.

(81) Aksakal, N. E.; Eçik, E. T.; Kazan, H. H.; Yenilmez Çiftçi, G.; Yuksel, F. Novel Ruthenium(II) and Iridium(III) BODIPY Dyes: Insights into Their Application in Photodynamic Therapy in Vitro. *Photochem. Photobiol. Sci.* **2020**, *18* (8), 2012–2022.

(82) Burgess, K.; Burghart, A.; Chen, J.; Wan, C.-W. New Chemistry of BODIPY Dyes and BODIPY Dye Cassettes Featuring Through-Bond Energy Transfer. *Proc. SPIE 3926, Adv. Nucleic Acid Protein Anal. Manip. Seq.* **2000**, *3926* (6), 95–105.

(83) Kamkaew, A.; Burgess, K. Double-Targeting Using a Trkc Ligand Conjugated to Dipyrrometheneboron Difluoride (BODIPY) Based Photodynamic Therapy (PDT). *J. Med. Chem.* **2013**, *56* (19), 7608–7614.

(84) Lu, H.; Mack, J.; Yang, Y.; Shen, Z. Structural Modification Strategies for the

Rational Design of Red/NIR Region BODIPYs. *Chem. Soc. Rev.* **2014**, *43* (13), 4778–4823.

(85) Yang, Y.; Guo, Q.; Chen, H.; Zhou, Z.; Guo, Z.; Shen, Z. Thienopyrrole-Expanded BODIPY as a Potential NIR Photosensitizer for Photodynamic Therapy. *Chem. Commun.* **2013**, *49* (38), 3940–3942.

(86) Kamkaew, A.; Lim, S. H.; Lee, H. B.; Kiew, L. V.; Chung, L. Y.; Burgess, K. BODIPY Dyes in Photodynamic Therapy. *Chem. Soc. Rev.* **2012**, *42* (1), 77–88.

(87) Lu, P.; Chung, K. Y.; Stafford, A.; Kiker, M.; Kafle, K.; Page, Z. A. Boron Dipyrromethene (BODIPY) in Polymer Chemistry. *Polym. Chem.* **2021**, *12* (3), 327–348.

(88) Wu, L.; Burgess, K. A New Synthesis of Symmetric Boraindacene (BODIPY) Dyes. *Chem. Commun.* **2008**, 1*0* (40), 4933–4935.

(89) Thivierge, C.; Loudet, A.; Burgess, K. Brilliant BODIPY-Fluorene Copolymers with Dispersed Absorption and Emission Maxima. *Macromolecules* **2011**, *44* (10), 4012–4015.

(90) Kim, H.; Burghart, A.; Welch, M. B.; Reibenspies, J.; Burgess, K. Synthesis and Spectroscopic Properties of a New 4-Bora-3a,4a-Diaza- s -Indacene (BODIPY ®) Dye. *Chem. Commun.* **1999**, *3* (18), 1889–1890.

(91) Ngoy, B. P.; Molupe, N.; Harris, J.; Fomo, G.; Mack, J.; Nyokong, T. Photophysical Studies of 2,6-Dibrominated BODIPY Dyes Substituted with 4-Benzyloxystyryl Substituents. *J. Porphyr. Phthalocyanines* **2017**, *21* (4), 431–438.

(92) Li, L.; Nguyen, B.; Burgess, K. Functionalization of the 4,4-Difluoro-4-Bora-

3a,4a-Diaza-s-Indacene (BODIPY) Core. *Bioorg. Med. Chem. Lett.* **2008**, *18* (10), 3112–3116.

(93) Lim, S. H.; Thivierge, C.; Nowak-Sliwinska, P.; Han, J.; Van Den Bergh, H.; Wagnières, G.; Burgess, K.; Lee, H. B. In Vitro and in Vivo Photocytotoxicity of Boron Dipyrromethene Derivatives for Photodynamic Therapy. *J. Med. Chem.* **2010**, *53* (7), 2865–2874.

(94) Kubheka, G.; Babu, B.; Prinsloo, E.; Kobayashi, N.; Mack, J.; Nyokong, T. Photodynamic Activity of 2,6-Dibrominated Dimethylaminophenylbuta-1,3-DienylBODIPY Dyes. *J. Porphyr. Phthalocyanines* **2020**, *25* (1), 47–55.

(95) Mehraban, N.; Freeman, H. S. Developments in PDT Sensitizers for Increased Selectivity and Singlet Oxygen Production. *Materials* **2015**, *8* (7), 4421–4456.

(96) Epelde-Elezcano, N.; Martínez-Martínez, V.; Peña-Cabrera, E.; Gómez-Durán, C. F. A.; Arbeloa, I. L.; Lacombe, S. Modulation of Singlet Oxygen Generation in Halogenated BODIPY Dyes by Substitution at Their Meso Position: Towards a Solvent-Independent Standard in the Vis Region. *RSC Adv.* **2016**, *6* (48), 41991–41998.

(97) Jiang, X. D.; Xi, D.; Le Guennic, B.; Guan, J.; Jacquemin, D.; Guan, J.; Xiao, L. J. Synthesis of NIR Naphthyl-Containing Aza-BODIPYs and Measure of the Singlet Oxygen Generation. *Tetrahedron* **2015**, *71* (40), 7676–7680.

(98) Kue, C. S.; Ng, S. Y.; Voon, S. H.; Kamkaew, A.; Chung, L. Y.; Kiew, L. V.; Lee, H. B. Recent Strategies to Improve Boron Dipyrromethene (BODIPY) for Photodynamic Cancer Therapy: An Updated Review. *Photochem. Photobiol. Sci* **2020**, *17* (11), 1691–1708.

(99) Nie, X.; Wu, S.; Mensah, A.; Wang, Q.; Huang, F.; Wei, Q. FRET as a Novel Strategy to Enhance the Singlet Oxygen Generation of Porphyrinic MOF Decorated Self-Disinfecting Fabrics. *Chem. Eng. J.* **2020**, *395* (125012), 1–11.

(100) Adarsh, N.; Shanmugasundaram, M.; Avirah, R. R.; Ramaiah, D. Aza-BODIPY Derivatives: Enhanced Quantum Yields of Triplet Excited States and the Generation of Singlet Oxygen and Their Role as Facile Sustainable Photooxygenation Catalysts. *Chem. Eur. J.* **2012**, *18* (40), 12655–12662.

(101) Thomson, C. G.; Jones, C. M. S.; Rosair, G.; Ellis, D.; Marques-Hueso, J.; Lee, A. L.; Vilela, F. Continuous-Flow Synthesis and Application of Polymer-Supported BODIPY Photosensitisers for the Generation of Singlet Oxygen; Process Optimised by in-Line NMR Spectroscopy. *J. Flow Chem.* **2020**, *10* (1), 327–345.

(102) Adarsh, N.; Avirah, R. R.; Ramaiah, D. Tuning Photosensitized Singlet Oxygen Generation Efficiency of Novel Aza-BODIPY Dyes. *Org. Lett.* **2010**, *12* (24), 5720–5723.

(103) Donnelly, J. L.; Offenbartl-Stiegert, D.; Marín-Beloqui, J. M.; Rizzello, L.; Battaglia, G.; Clarke, T. M.; Howorka, S.; Wilden, J. D. Exploring the Relationship between BODIPY Structure and Spectroscopic Properties to Design Fluorophores for Bioimaging. *Chem. Eur. J.* **2020**, *26* (4), 863–872.

(104) Gai, L.; Lu, H.; Zou, B.; Lai, G.; Shen, Z.; Li, Z. Synthesis and Spectroscopic Properties of Bodipy Dimers with Effective Solid-State Emission. *RSC Adv.* **2012**, *2* (23), 8840–8846.

(105) Leen, V.; Miscoria, D.; Yin, S.; Filarowski, A.; Molisho Ngongo, J.; Van Der Auweraer, M.; Boens, N.; Dehaen, W. 1,7-Disubstituted Boron Dipyrromethene

(BODIPY) Dyes: Synthesis and Spectroscopic Properties. *J. Org. Chem.* **2011**, *76* (20), 8168–8176.

(106) Chen, P. Z.; Niu, L. Y.; Chen, Y. Z.; Yang, Q. Z. Difluoroboron β-Diketonate Dyes: Spectroscopic Properties and Applications. *Coord. Chem. Rev.* **2017**, *350*, 196–216.

(107) Descalzo, A. B.; Ashokkumar, P.; Shen, Z.; Rurack, K. On the Aggregation Behaviour and Spectroscopic Properties of Alkylated and Annelated Boron-Dipyrromethene (BODIPY) Dyes in Aqueous Solution. *ChemPhotoChem* **2020**, *4* (2), 120–131.

(108) Huang, J.; Fang, Y.; Dehaen, W. Macrocyclic Arenes Functionalized with BODIPY: Rising Stars among Chemosensors and Smart Materials. *Chemosensors* **2020**, *8* (3), 1–23.

(109) Rezende, L.; Rezende, L. C. D.; Emery, F. S. A Review of the Synthetic Strategies for the Development of BODIPY Dyes for Conjugation with Proteins. *Orbital Electron. J. Chem.* **2013**, *5* (1), 62–83.

(110) Wang, J.; Gong, Q.; Wang, L.; Hao, E.; Jiao, L. The Main Strategies for Tuning BODIPY Fluorophores into Photosensitizers. *J. Porphyr. Phthalocyanines* **2020**, *24* (5–7), 603–635.

(111) Loudet, A.; Burgess, K. BODIPY Dyes and Their Derivatives: Syntheses and Spectroscopic Properties. *Chem. Rev.* **2007**, *107* (11), 4891–4932.

(112) Shivran, N.; Tyagi, M.; Mula, S.; Gupta, P.; Saha, B.; Patro, B. S.; Chattopadhyay, S. Syntheses and Photodynamic Activity of Some Glucose-Conjugated BODIPY Dyes. *Eur. J. Med. Chem.* **2016**, *122*, 352–365.

(113) Wang, L.; Bai, J.; Qian, Y. Synthesis of a Triphenylamine BODIPY Photosensitizer with D–A Configuration and Its Application in Intracellular Simulated Photodynamic Therapy. *New J. Chem.* **2019**, *43* (43), 16829–16834.

(114) Ramu, V.; Gautam, S.; Garai, A.; Kondaiah, P.; Chakravarty, A. R. Glucose-Appended Platinum(II)-BODIPY Conjugates for Targeted Photodynamic Therapy in Red Light. *Inorg. Chem.* **2018**, *57* (4), 1717–1726.

(115) Dartar, S.; Ucuncu, M.; Karakus, E.; Hou, Y.; Zhao, J.; Emrullahoglu, M. BODIPY–Vinyl Dibromides as Triplet Sensitisers for Photodynamic Therapy and Triplet–Triplet Annihilation Upconversion. *Chem. Commun.* **2021**, *57* (49),

(116) Tahoun, M.; Gee, C. T.; McCoy, V. E.; Sander, P. M.; Müller, C. E. Chemistry of Porphyrins in Fossil Plants and Animals. *RSC Adv.* **2021**, *11* (13), 7552–7563.

(117) Senge, M. O.; Ryan, A. A.; Letchford, K. A.; MacGowan, S. A.; Mielke, T. Chlorophylls, Symmetry, Chirality, and Photosynthesis. *Symmetry* **2014**, *6* (3), 781–843.

(118) Taniguchi, M.; Bocian, D. F.; Holten, D.; Lindsey, J. S. Beyond Green with Synthetic Chlorophylls – Connecting Structural Features with Spectral Properties. *J. Photochem. Photobiol. C: Photochem. Rev.* **2022**, *5* (36), 1–153.

(119) Diers, J. R.; Kirmaier, C.; Taniguchi, M.; Lindsey, J. S.; Bocian, D. F.; Holten, D. A Perspective on the Redox Properties of Tetrapyrrole Macrocycles. *Phys. Chem. Chem. Phys.* **2021**, *23* (35), 19130–19140.

(120) Novak, I. Photoionization of tetrapyrrole macrocycles: Porphyrin isomers and corrole tautomers. *J. Photochem. Photobiol. A* **2022**, *427* (113849), 1–6.

(121) Mack, J. Expanded, Contracted, and Isomeric Porphyrins: Theoretical Aspects.

Chem. Rev. **2017**, *117* (4), 3444–3478.

(122) Spence, J. D.; Lash, T. D. Porphyrins with Exocyclic Rings. 14. Synthesis of Tetraacenaphthoporphyrins, a New Family of Highly Conjugated Porphyrins with Record-Breaking Long-Wavelength Electronic Absorptions. *J. Org. Chem.* **2000**, *65* (5), 1530–1539.

(123) Ste˛pień, M.; Latos-Graz.yński, L. Aromaticity and Tautomerism in Porphyrins and Porphyrinoids. In: Krygowski, T.M., Cyrański, M.K. (Eds) Aromaticity in Heterocyclic Compounds. Topics in Heterocyclic Chemistry. In *Springer, Berlin, Heidelberg*; Springer, Berlin, Heidelberg, **2009**; Vol. 19, pp 1–71.

(124) Schwartz, S.; Berg, M. H.; Bossenmaier, I.; Dinsmore, H. Determination of Porphyrins in Biological Materials. In *Methods of Biochemical Analysis, D. Glick (Ed.).*; John Wiley & Sons, Ltd, 2006; pp 221–293.

(125) Lash, T. D. Modification of the Porphyrin Chromophore by Ring Fusion: Identifying Trends Due to Annelation of the Porphyrin Nucleus. *J. Porphyr. Phthalocyanines* **2001**, *5* (3), 267–288.

(126) Brückner, C.; McCarthy, J. R.; Daniell, H. W.; Pendon, Z. D.; Ilagan, R. P.; Francis, T. M.; Ren, L.; Birge, R. R.; Frank, H. A. A Spectroscopic and Computational Study of the Singlet and Triplet Excited States of Synthetic β-Functionalized Chlorins. *Chem. Phys.* **2003**, *294* (3), 285–303.

(127) Gouterman, M. Spectra of Porphyrins. *J. Mol. Spectrosc.* **1961**, *6* (C), 138–163.

(128) Baker, E. W. Porphyrins. *Org. Geochem.* **1969**, 464–497.

(129) Gouterman, M.; Wagnière, G. H.; Snyder, L. C. Spectra of Porphyrins: Part II. Four Orbital Model. *J. Mol. Spectrosc.* **1963**, *11* (1–6), 108–127.

(130) Wang, X. F.; Tamiaki, H. Cyclic Tetrapyrrole Based Molecules for Dye-Sensitized Solar Cells. *Energy Environ. Sci.* **2010**, *3* (1), 94–106.

(131) Hiroto, S.; Miyake, Y.; Shinokubo, H. Synthesis and Functionalization of Porphyrins through Organometallic Methodologies. *Chem. Rev.* **2017**, *117* (4), 2910–3043.

(132) Brückner, C.; Mccarthy, J. R.; Daniell, H. W.; Pendon, Z. D.; Ilagan, R. P.; Francis, T. M.; Ren, L.; Birge, R. R.; Frank, H. A. A Spectroscopic and Computational Study of the Singlet and Triplet Excited States of Synthetic B-Functionalized Chlorins. *Chem. Phys.* **2003**, *294*, 285–303.

(133) Babu, B; Mack, J; Nyokong, T. A Sn(IV) Porphyrin with Mitochondria Targeting Properties for Enhanced Photodynamic Activity against MCF-7 Cells. *New J. Chem.* **2022**, *46* (11), 5288–5295.

(134) Babu, B.; Mack, J.; Nyokong, T. An Octabrominated Sn(Iv) Tetraisopropylporphyrin as a Photosensitizer Dye for Singlet Oxygen Biomedical Applications. *Dalton Trans.* **2020**, *49* (28), 9568–9573.

(135) Dingiswayo, S.; Babu, B.; Prinsloo, E.; Mack, J.; Nyokong, T. A Comparative Study of the Photophysicochemical and Photodynamic Activity Properties of Meso-4-Methylthiophenyl Functionalized Sn(IV) Tetraarylporphyrins and Triarylcorroles. *J. Porphyr. Phthalocyanines* **2020**, *24* (9), 1138–1145.

(136) Babu, B.; Mack, J.; Nyokong, T. Sn(Iv) N -Confused Porphyrins as Photosensitizer Dyes for Photodynamic Therapy in the near IR Region. *Dalton Trans.* **2020**, *49* (43), 15180–15183.

(137) Soy, R. C.; Babu, B.; Oluwole, D. O.; Nwaji, N.; Oyim, J.; Amuhaya, E.; Prinsloo,

E.; Mack, J.; Nyokong, T. Photophysicochemical Properties and Photodynamic Therapy Activity of Chloroindium(III) Tetraarylporphyrins and Their Gold Nanoparticle Conjugates. *J. Porphyr. Phthalocyanines* **2021**, *23* (3), 207–218.

(138) Babu, B.; Amuhaya, E.; Oluwole, D.; Prinsloo, E.; Mack, J.; Nyokong, T. Preparation of NIR Absorbing Axial Substituted Tin(Iv) Porphyrins and Their Photocytotoxic Properties. *Medchemcomm* **2019**, *10* (1), 41–48.

(139) Rothemund, P. A New Porphyrin Synthesis. The Synthesis of Porphin. *J. Am. Chem. Soc.* **1936**, *58* (4), 625–627.

(140) Gonsalves, A. M. D. A. R.; Pereira, M. M. A New Look into the Rothemund Meso-Tetraalkyl and Tetraarylporphyrin Synthesis. *J. Heterocycl. Chem.* **1985**, *22* (3), 931–933.

(141) Chmielewski, P. J.; Latos-Grażyński, L.; Rachlewicz, K. 5,10,15,20-Tetraphenylsapphyrin-Identification of a Pentapyrrolic Expanded Porphyrin in the Rothemund Synthesis. *Chem. Eur. J.* **1995**, *1* (1), 68–73.

(142) Badger, G. M.; Alan Jones, R.; Laslett, R. L. Porphyrins. VII. The Synthesis of Porphyrins by the Rothemund Reaction. *Aust. J. Chem.* **1964**, *17* (9), 1028–

(143) Lindsey, J. S.; Schreiman, I. C.; Hsu, H. C.; Kearney, P. C.; Marguerettaz, A. M. Rothemund and Adler-Longo Reactions Revisited: Synthesis of Tetraphenylporphyrins under Equilibrium Conditions. *J. Org. Chem.* **1987**, *52* (5), 827–836.

(144) Kitaoka, S.; Nobuoka, K.; Ihara, K.; Ishikawa, Y. A Simple Method for Efficient Synthesis of Tetrapyridyl-Porphyrin Using Adler Method in Acidic Ionic Liquids. *RSC Adv.* **2014**, *4* (51), 26777–26782.

(145) Silva E. M. P.; Giuntini F.; Faustino M. A., Tomé J. P. C.; Neves M. G. P. M. S.; Tomé A. C;, Silva A. M. S.; Santana-Marques M. G.; Ferrer-Correia A. J.; Cavaleiro J. A. S.; Caeiro M. F.; Duarte R. R.;Tavares S. A. P.; Pegado I. N.; d'Almeida B.; De Matos A. P. A.; Valdeira M. L. Synthesis of cationic beta-vinyl substituted meso-tetraphenylporphyrins and their in vitro activity against herpes simplex virus type 1. *Bioorg. Med. Chem. Lett*. 2005, 15 (14), 3333-3337.

(146) Campbell W. M.; Jolley K. W.; Wagner P.; Wagner K.; Wagner P. J.; Gordon K. C.; Schmidt-Mende L.; Schmidt-Mende M. K.; Wang Q.; Grätzel M.; Officer D. L. Highly Efficient Porphyrin Sensitizers for Dye-Sensitized Solar Cells. *J. Phys. Chem. A* **2007**, 111 (32), *11760-11762.*

(147) Onaka M.; Shinoda T.; Izumi Y.; Nolen Ernest. Porphyrin Synthesis in Clay Nanospaces. *Chem. Lett.* **1993**, *22* (1), 117–120.

(148) Henriques, C. A.; Pinto, S. M. A.; Aquino, G. L. B.; Pineiro, M.; Calvete, M. J. F.; Pereira, M. M. Ecofriendly Porphyrin Synthesis by Using Water under Microwave Irradiation. *ChemSusChem* **2014**, *7* (10), 2821–2824.

(149) Drain, C. M.; Gong, X. Synthesis of Meso Substituted Porphyrins in Air without Solvents or Catalysts. *Chem. Commun.* **1997**, *0* (21), 2117–2118.

(150) Lindsey, J. S. The Synthesis of Meso-Substituted Porphyrins. In *Montanari, F., Casella, L. (eds) Metalloporphyrins Catalyzed Oxidations. Catalysis by Metal Complexes*; Springer, Dordrecht, **1994**; pp 49–86.

(151) Wang, P.; Qin, F.; Zhang, Z.; Cao, W. Quantitative Monitoring of the Level of Singlet Oxygen Using Luminescence Spectra of Phosphorescent Photosensitizer. *Opt. Express* **2015**, *23* (18), 22991–23003.

(152) Żamojć, K.; Zdrowowicz, M.; Rudnicki-Velasquez, P. B.; Krzymiński, K.; Zaborowski, B.; Niedziałkowski, P.; Jacewicz, D.; Chmurzyński, L. The Development of 1,3-Diphenylisobenzofuran as a Highly Selective Probe for the Detection and Quantitative Determination of Hydrogen Peroxide. *Free Radic. Res.* **2017**, *51* (1), 38–46.

(153) Sanasam, B.; Raza, M. K.; Musib, D.; Roy, M. Photochemical and Photocytotoxic Evaluation of New Oxovanadium (IV) Complexes in Photodynamic Application. *J. Chem. Sci.* **2021**, *133* (2), 1–14.

(154) Chadwick, S. J.; Salah, D.; Livesey, P. M.; Brust, M.; Volk, M. Singlet Oxygen Generation by Laser Irradiation of Gold Nanoparticles. *J. Phys. Chem. C* **2016**, *120* (19), 10647–10657.

(155) Albiter, E.; Alfaro, S.; Valenzuela, M. A. Photosensitized Oxidation of 9,10-Dimethylanthracene with Singlet Oxygen by Using a Safranin O/Silica Composite under Visible Light. *Photochem. Photobiol. Sci.* **2015**, *14* (3), 597–602.

(156) Albiter, E.; Alfaro, S.; Valenzuela, M. A. Photosensitized Oxidation of 9,10-Dimethylanthracene on Dye-Doped Silica Composites. *Int. J. Photoenergy* **2011**, *2012* (23), 1–8.

(157) Clennan, E. L. Synthetic and Mechanistic Aspects of 1,3-Diene Photooxidation. *Tetrahedron* **1991**, *47* (8), 1343–1382.

(158) Chen, S., Chen, W., Shi, W. and Ma, H., Spectroscopic Response of Ferrocene Derivatives Bearing a BODIPY Moiety to Water: A New Dissociation Reaction *Eur. J. Chem.*, **2012**, 18 (3), 925-930.

(159) Zhang, X. F.; Li, X. The Photostability and Fluorescence Properties of Diphenylisobenzofuran. *J. Lumin.* **2011**, *131* (11), 2263–2266.

(160) Bobrowski, M.; Liwo, A.; Ołdziej, S.; Jeziorek, D.; Ossowski, T. CAS MCSCF/CAS MCQDPT2 Study of the Mechanism of Singlet: Oxygen Addition to 1,3-Butadiene and Benzene. *J. Am. Chem. Soc.* **2000**, *122* (34), 8112–8119.

(161) Castro-Olivares, R.; Günther, G.; Zanocco, A. L.; Lemp, E. Linear Free Energy Relationship Analysis of Solvent Effect on Singlet Oxygen Reactions with Mono and Disubstituted Anthracene Derivatives. *J. Photochem. Photobiol. A* **2009**, *207* (23), 160–166.

(162) Singh, A.; McIntyre, N. R.; Koroll, G. W. Photochemical Formation Of Metastable Species From 1,3-Diphenylisobenzofuran. *Photochem. Photobiol.* **1978**, *28* (45), 595–601.

(163) Fujii, M.; Usui, M.; Hayashi, S.; Gross, E.; Kovalev, D.; Künzner, N.; Diener, J.; Timoshenko, V. Y. Chemical Reaction Mediated by Excited States of Si Nanocrystals-Singlet Oxygen Formation in Solution. *J. Appl. Phys.* **2004**, *95* (7), 3689.

(164) Aubry, J. M.; Pierlot, C.; Rigaudy, J.; Schmidt, R. Reversible Binding of Oxygen to Aromatic Compounds. *Acc. Chem. Res.* **2003**, *36* (9), 668–675.

(165) Fudickar, W.; Linker, T. Imaging by Sensitized Oxygenations of Photochromic Anthracene Films: Examination of Effects That Improve Performance and Reversibility. *Chem. Eur. J.* **2006**, *12* (36), 9276–9283.

(166) Chadwick, S. J.; Salah, D.; Livesey, P. M.; Brust, M.; Volk, M. Singlet Oxygen Generation by Laser Irradiation of Gold Nanoparticles. *J. Phys. Chem.* **2016**,

120 (19), 10647–10657.

(167) Qin, F.; Wang, P.; Cao, W.; Zhang, Z. Quantitative Monitoring of the Level of Singlet Oxygen Using Luminescence Spectra of Phosphorescent Photosensitizer. *Opt. Express* **2015**, *23* (18), 22991–23003.

(168) Wang, P.; Qin, F.; Zhang, Z.; Cao, W. Quantitative Monitoring of the Level of Singlet Oxygen Using Luminescence Spectra of Phosphorescent Photosensitizer. *Opt. Express* **2015**, *23* (18), 22991–23003.

(169) Wanhua L., Jingfan X., Yuanjun H., Guoyu J., Hongyan Z., Pengfei W., Xuesong W., Baowen Z. Mitochondria-targeting properties and photodynamic activities of porphyrin derivatives bearing cationic pendant. *J. Photochem. Photobiol. B* **2010**, *98* (2), 167-17.

(170) Aveline, B.; Hasan, T.; Redmond, R. W. Photophysical And Photosensitizing Properties Of Benzoporphyrin Derivative Monoacid Ring A (Bpd-Ma). *Photochem. Photobiol.* **1994**, *59* (3), 328–335.

(171) Karolczak, J.; Kowalska, D.; Lukaszewicz, A.; Maciejewski, A.; Steer, R. P. Photophysical Studies of Porphyrins and Metalloporphyrins: Accurate Measurements of Fluorescence Spectra and Fluorescence Quantum Yields for Soret Band Excitation of Zinc Tetraphenylporphyrin. *J. Phys. Chem. A* **2004**, *108* (21), 4570–4575.

(172) Nyokong, T.; Antunes, E. Photochemical and Photophysical Properties of Metallophthalocyanines. In *Handbook of Porphyrin Science*, World Scientific, Singapore, **2010**; pp 247–357.

(173) https://micro.magnet.fsu.edu/primer/java/jablonski/jabintro/index.html

(accessed May 16, 2022).

(174) Fischer, M.; Georges, J. Fluorescence Quantum Yield of Rhodamine 6G in Ethanol as a Function of Concentration Using Thermal Lens Spectrometry. *Chem. Phys. Lett.* **1996**, *260* (1–2), 115–118.

(175) Soy, R. C.; Babu, B.; Oluwole, D. O.; Nwaji, N.; Oyim, J.; Amuhaya, E.; Prinsloo, E.; Mack, J.; Nyokong, T. Photophysicochemical Properties and Photodynamic Therapy Activity of Chloroindium(III) Tetraarylporphyrins and Their Gold Nanoparticle Conjugates. *Porphyrin Science by Women* **2021**, 207–218.

(176) Babu, B.; Sindelo, A.; Mack, J.; Nyokong, T. Thien-2-yl Substituted Chlorins as Photosensitizers for Photodynamic Therapy and Photodynamic Antimicrobial Chemotherapy. *Dye. Pigm.* **2021**, *185* (108886), 1–8.

(177) Babu, B.; Soy, R. C.; Mack, J.; Nyokong, T. Non-Aggregated Lipophilic Water-Soluble Tin Porphyrins as Photosensitizers for Photodynamic Therapy and Photodynamic Antimicrobial Chemotherapy. *New J. Chem.* **2020**, *44* (26),

(178) Magadla, A.; Babu, B.; Mack, J.; Nyokong, T. Positively Charged Styryl Pyridine Substituted Zn(II) Phthalocyanines for Photodynamic Therapy and Photoantimicrobial Chemotherapy: Effect of the Number of Charges. *Dalton Trans.* **2021**, *50* (26), 9129–9136.

(179) Openda, Y. I.; Babu, B.; Nyokong, T. Novel Cationic-Chalcone Phthalocyanines for Photodynamic Therapy Eradication of S. Aureus and E. Coli Bacterial Biofilms and MCF-7 Breast Cancer. *Photodiagnosis Photodyn. Ther.* **2022**, *38* (102863), 1–14.

(180) Bera, A.; Gautam, S.; Raza, M. K.; Pal, A. K.; Kondaiah, P.; Chakravarty, A. R.

BODIPY–Dipicolylamine Complexes of Platinum(Ii): X-Ray Structure, Cellular Imaging and Organelle-Specific near-IR Light Type-II PDT. *Dalton Trans.* **2022**, *51* (10), 3925–3936.

(181) Bhattacharyya, U.; Verma, B. K.; Saha, R.; Mukherjee, N.; Raza, M. K.; Sahoo, S.; Kondaiah, P.; Chakravarty, A. R. Structurally Characterized BODIPY-Appended Oxidovanadium(IV) β-Diketonates for Mitochondria-Targeted Photocytotoxicity. *ACS Omega* **2020**, *5* (8), 4282–4292.

(182) Pandey, V.; Raza, M. K.; Sonowal, M.; Gupta, I. BODIPY Based Red Emitters: Synthesis, Computational and Biological Studies. *Bioorg. Chem.* **2021**, *106* (104467), 1–9.

(183) Bera, A.; Gautam, S.; Raza, M. K.; Kondaiah, P.; Chakravarty, A. R. Oxoplatin-B, a Cisplatin-Based Platinum(IV) Complex with Photoactive BODIPY for Mitochondria Specific “Chemo-PDT” Activity. *J. Inorg. Biochem.* **2021**, *223* (111526), 1–9.

(184) Soy, R. C.; Babu, B.; Mack, J.; Nyokong, T. The Photodynamic Activities of the Gold Nanoparticle Conjugates of Phosphorus(V) and Gallium(III) A3 Meso-Triarylcorroles. *Dye. Pigm.* **2021**, *194* (109631), 1–13.

(185) Yang, F.; Zhang, Y.; Liang, H. Interactive Association of Drugs Binding to Human Serum Albumin. *Int. J. Mol. Sci.* **2014**, *15* (3), 3580–3595.

(186) Rohand, T.; Dolusic, E.; Ngo, T. H.; Maes, W.; Dehaen, W. Efficient Synthesis of Aryldipyrromethanes in Water and Their Application in the Synthesis of Corroles and Dipyrromethenes. *Arkivoc* **2007**, *56* (10), 307–324.

(187) Zhang, A.; Kwan, L.; Stillman, M. J. The Spectroscopic Impact of Interactions

with the Four Gouterman Orbitals from Peripheral Decoration of Porphyrins with Simple Electron Withdrawing and Donating Groups. *Org. Biomol. Chem.* **2017**, *15* (43), 9081–9094.

(188) Muranaka, A.; Yokoyama, M.; Matsumoto, Y.; Uchiyama, M.; Tsuda, A.; Osuka, A.; Kobayashi, N. Magnetic Circular Dichroism Study of Directly Fused Porphyrins. *ChemPhysChem* **2005**, *6* (1), 171–179.

(189) Ngoy, B. P.; Molupe, N.; Harris, J.; Fomo, G.; Mack, J.; Nyokong, T. Photophysical Studies of 2,6-Dibrominated BODIPY Dyes Substituted with 4-Benzyloxystyryl Substituents. *J. Porphyr. Phthalocyanines* **2017**, *21* (46), 431–438.

(190) Olmsted, J. Calorimetric Determinations of Absolute Fluorescence Quantum Yields. *J. Phys. Chem.* **1979**, *83* (20), 2581–2584.

(191) Zhang, X. F.; Xu, H. J. Influence of Halogenation and Aggregation on Photosensitizing Properties of Zinc Phthalocyanine (ZnPC). *J. Chem. Soc. Faraday Trans.* **1993**, *89* (18), 3347–3351.

(192) Lombardo, F.; Shalaeva, M. Y.; Tupper, K. A.; Gao, F.; Abraham, M. H. ElogP(Oct): A Tool for Lipophilicity Determination in Drug Discovery. *J. Med. Chem.* **2000**, *43* (15), 2922–2928.

(193) Ràfols, C.; Subirats, X.; Rubio, J.; Rosés, M.; Bosch, E. Lipophilicity of Amphoteric and Zwitterionic Compounds: A Comparative Study of Determination Methods. *Talanta* **2017**, *162* (3), 293–299.

(194) Mehanna, S.; Mansour, N.; Audi, H.; Bodman-Smith, K.; Mroueh, M. A.; Taleb, R. I.; Daher, C. F.; Khnayzer, R. S. Enhanced Cellular Uptake and

Photochemotherapeutic Potential of a Lipophilic Strained Ru(II) Polypyridyl Complex. *RSC Adv.* **2019**, *9* (30), 17254–17265.

(195) Ermondi, G.; Vallaro, M.; Saame, J.; Toom, L.; Leito, I.; Ruiz, R.; Caron, G. Rifampicin as an Example of Beyond-Rule-of-5 Compound: Ionization beyond Water and Lipophilicity beyond Octanol/Water. *Eur. J. Pharm. Sci.* **2021**, *161* (105802), 1–8.

(196) Pisani, M. J.; Fromm, P. D.; Mulyana, Y.; Clarke, R. J.; Körner, H.; Heimann, K.; Collins, J. G.; Keene, F. R. Mechanism of Cytotoxicity and Cellular Uptake of Lipophilic Inert Dinuclear Polypyridylruthenium(II) Complexes. *ChemMedChem* **2011**, *6* (5), 848–858.

(197) Andrić, F.; Bajusz, D.; Rácz, A.; Šegan, S.; Héberger, K. Multivariate Assessment of Lipophilicity Scales−Computational and Reversed Phase Thin-Layer Chromatographic Indices. *J. Pharm. Biomed. Anal.* **2016**, *127*, 81–93.

(198) Lameijer, L. N.; Brevé, T. G.; van Rixel, V. H. S.; Askes, S. H. C.; Siegler, M. A.; Bonnet, S. Effects of the Bidentate Ligand on the Photophysical Properties, Cellular Uptake, and (Photo)Cytotoxicity of Glycoconjugates Based on the [Ru(Tpy)(NN)(L)]2+ Scaffold. *Chem. Eur.J* **2018**, *24* (5), 2709–2717.

(199) Chakraborty, G.; Ray, A. K.; Singh, P. K.; Pal, H. Non-Covalent Interaction of BODIPY-Benzimidazole Conjugate with Bovine Serum Albumin–A Photophysical and Molecular Docking Study. *J. Photochem. Photobiol. A* **2019**, *377*, 220–227.

(200) Alnoman, R. B.; Hagar, M.; Parveen, S.; Ahmed, H. A.; Knight, J. G. Computational and Molecular Docking Approaches of a New Axially Chiral BODIPY Fluorescent Dye. *J. Photochem. Photobiol. A.* **2020**, *395* (112508), 1–

10.

(201) Paitandi, R. P.; Mukhopadhyay, S.; Singh, R. S.; Sharma, V.; Mobin, S. M.; Pandey, D. S. Anticancer Activity of Iridium(III) Complexes Based on a Pyrazole-Appended Quinoline-Based BODIPY. *Inorg. Chem.* **2017**, *56* (20), 12232–12247.

(202) Ksenofontov, A. A.; Bocharov, P. S.; Antina, E. V. Interaction of Tetramethyl-Substituted BODIPY Dye with Bovine Serum Albumin: Spectroscopic Study and Molecular Docking. *J. Photochem. Photobiol. A.* **2019**, *368*, 254–257.

(203) Jeena, M. T.; Kim, S.; Jin, S.; Ryu, J. H. Recent Progress in Mitochondria-Targeted Drug and Drug-Free Agents for Cancer Therapy. *Cancers (Basel).* **2020**, *12* (1), 1–8.

(204) Sobotta, L.; Skupin-Mrugalska, P.; Piskorz, J.; Mielcarek, J. Porphyrinoid Photosensitizers Mediated Photodynamic Inactivation against Bacteria. *Eur. J. Med. Chem.* **2019**, *175*, 72–106.

(205) G. W. T. M. J. Frisch, H. B. Schlegel, G. E. Scuseria, M. A. Robb, J. R., G. S. Cheeseman, V. Barone, G. A. Petersson, H. Nakatsuji, X. Li, M. Caricato, A. Marenich, J., B. G. J. Bloino, R. Gomperts, B. Mennucci, H. P. Hratchian, J. V. Ortiz, A. F. Izmaylov, J. L., D. W.-Y. Sonnenberg, F. Ding, F. Lipparini, F. Egidi, J. Goings, B. Peng, A. Petrone, T., D. R. Henderson, V. G. Zakrzewski, J. Gao, N. Rega, G. Zheng, W. Liang, M. Hada, M. Ehara, K., R. F. Toyota, J. Hasegawa, M. Ishida, T. Nakajima, Y. Honda, O. Kitao, H. Nakai, T. Vreven, K., J. A. M. Throssell, Jr., J. E. Peralta, F. Ogliaro, M. Bearpark, J. J. Heyd, E. Brothers, K. N. Kudin, T. K. V. N. Staroverov, R. Kobayashi, J. Normand, K. Raghavachari, A. Rendell, J. C. Burant, S. S., J. T. Iyengar, M. Cossi, J. M.

Millam, M. Klene, C. Adamo, R. Cammi, J. W. Ochterski, R. L. Martin, O. F. K. Morokuma, J. B. Foresman, and D. J. Fox, *Gaussian 09*, *Revision 01*, Gaussian, Inc*.,* Wallingford CT, 2013.